MASTER

Characterisation of a dielectric barrier discharge with a square mesh electrode

van der Schans, M.

Award date:
2015

Technische Universiteit
Eindhoven
University of Technology

Department of Applied Physics
Elementary Processes in Gas discharges (EPG)

Characterisation of a dielectric barrier discharge with a square mesh electrode

M. van der Schans

27th November 2014 EPG 14-18

Supervisors:

dr. A. Sobota
dr. P. Smits
dr.ir. E.M. van Veldhuizen
prof.dr.ir. G.M.W. Kroesen

Graduation committee:

prof.dr.ir. G.M.W. Kroesen
dr. A. Sobota
dr. L.J. van IJzendoorn
dr.ir. S. Nijdam
dr.ing. A.J.M. Pemen
dr.ir. L.P.J. Kamp

Abstract

Foot ulcers constitute a major health problem for a rapidly growing number of people suffering from diabetes. Currently these wounds are difficult to treat, often become infected and are usually the first step to amputation. Treatment with non-thermal plasma may offer a solution to this situation. As a first step towards a suitable plasma source, a dielectric barrier discharge (DBD) device, which is named *plasma plaster*, is designed and characterised. The plasma plaster consists of a powered electrode and a polyimide barrier that covers the powered electrode. In the final application the targeted wound functions as secondary electrode. However, for the characterisation in the current study a stainless steel secondary electrode is used. A discharge is ignited in a 0.5 mm air gap between the plaster and the secondary electrode by applying pulsed voltage to the plaster. Two plaster types are investigated: one has a solid plane electrode (the *plane plaster*) and the other has a square mesh electrode (the *meshed plaster*). It is hypothesised that through local electric field enhancement the meshed plaster may facilitate a more uniform discharge distribution when the secondary electrode is irregularly shaped.

For both plasters a diffuse discharge is obtained rather than a filamentary discharge, which is attributed to the short discharge gap. Tomographic techniques are used to study the discharge distribution. For the plane plaster the discharge distribution in the gap is determined by the shape of the secondary electrode, while for the meshed plaster it is determined by the structure of the mesh. The gas temperature and reduced electric field are measured by optical emission spectroscopy. Gas temperatures of 325 K are measured for both plasters while operating at 6.5 kV and are considered safe for the application. A reduced electric field of 520 Td is found for the plane plaster, while a value of 600 Td is found for the meshed plaster. This increase of approximately 20% for the meshed plaster compared to the plane plaster is consistent with the local electric field enhancement predicted by electrostatic simulations. While further investigation is required to corroborate this final result, it suggests that the discharge distribution and reduced electric field can be controlled by adjusting the mesh pattern without undesirable side effects like an increase in gas temperature. This may open the way to tailor discharge properties for specific treatments.

Contents

Chapter 1

Introduction

1.1 Plasmas for biomedical applications

Over the past few decades plasma technology has taken a central position in many industrial applications. Some notable examples include the (pre)processing of polymer materials, the manufacturing of semiconductor devices, and waste and pollution management [1,2]. Often called the fourth state of matter, plasmas are (partially) ionised gases. Generally, plasmas can be divided into two types: thermal plasmas and non-thermal plasmas. In thermal plasmas the electrons and heavy particles (ions and neutrals) have the same energy, whereas in non-thermal plasmas the electrons attain higher energies than the heavy particles. As a result, a selective chemistry may be achieved in non-thermal plasmas, while maintaining a low gas temperature [2]. This is exactly how many of the established applications benefit from non-thermal plasmas.

A relatively new and rapidly growing area of research is that of plasma medicine, where non-thermal plasmas are directly applied in the treatment of living tissue. Plasmas have been used before in medical applications, such as tissue cutting and blood coagulation, but their operation is based on thermal effects of high temperature plasmas [3,4]. Numerous new biomedical applications of non-thermal plasma are currently being researched, including tissue sterilisation, wound healing and tissue regeneration, and the treatment of skin diseases. While plasma medicine is mostly still in an empirical stage and detailed knowledge of the interaction between plasma and biological objects is yet to be obtained, experiments have already confirmed its enormous potential. It is believed that synergistic effects between plasma components such as reactive species, charged particles, electric fields and ultraviolet (UV) radiation are at the basis of an effective treatment. Several review papers [5–8] and books [4,9] summarising the current status and discussing potential applications have been published. Furthermore, medical applications of plasmas is also one of the key topics addressed in 'The 2012 Plasma Roadmap' [10].

1.1.1 Plasma treatment of chronic wounds in diabetes

The work presented in this thesis is part of a larger endeavour with the goal to develop a plasma treatment for foot ulcers in diabetes. Currently, about 382 million people world wide suffer from diabetes mellitus, the most common form of diabetes. According to the International Diabetes Federation, this number is projected to increase towards 592 million by 2035 [11]. Diabetic patients have a risk of up to 25% to develop a foot ulcer during their lifetime, resulting from immune deficiency, nerve damage and poor blood flow. These type of wounds constitute a major health problem because they are difficult to treat, frequently become infected and are usually the first step to amputation [12–14]. Plasma medicine may aid and offer a solution to this situation.

The vision is to develop a *plasma plaster*: a device that is applied to the wound much like a conventional plaster, and generates plasma in a region of air enclosed by the wound and the plaster. Plasma species are delivered to the wound by direct contact. To illustrate, a famous example of a plasma source that operates in air and places the object to be treated in direct contact with the plasma is shown in figure 1.1 [2,4,15]. Such a source is of the dielectric barrier discharge (DBD) type and consists of at least four components: (1) a powered electrode to which high voltage is supplied, (2) a dielectric barrier, (3) a layer of air in which a discharge can be ignited, and (4) a secondary electrode which is either at a floating potential or grounded. The exact function of each of these components will be further elaborated on in Chapter 2. However, it should be noticed that the object to be treated acts as the secondary electrode and is hence part of the discharge geometry.

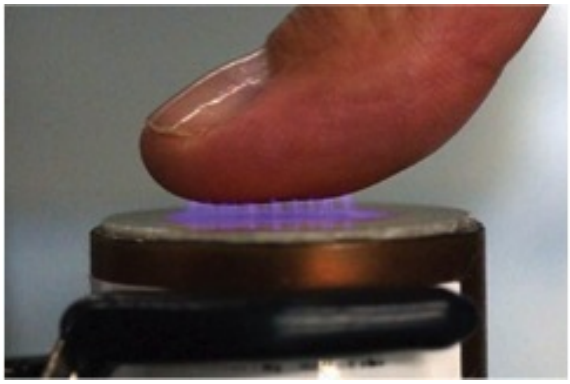

Figure 1.1: Illustration of a plasma source where the object to be treated (the finger) is in direct contact with the plasma. Plasma is generated in the air between the finger and the device at the bottom, which consists of a powered electrode covered by a dielectric material. Taken from the front cover of [2].

1.1.2 Plasma source requirements

An *in vivo* application of plasma imposes special requirements on the plasma source. In most cases a source will need to be designed specifically for the intended application. Generally, the requirements of a plasma source for medical applications arise from a combination of medical regulations, technical requisites and practical considerations.

To start, safety and controllability of any medical device must be guaranteed. Here this means that the used materials must be biocompatible under operation conditions in plasma. Biocompatibility means that there are no toxic or injurious effects on a biological object. It should be noted that biocompatibility is *not* an inherent property of a material, but rather a property of a material under specific operation conditions. When exposed to plasma, surface properties of a material may be altered or (components of) the material may be released by sputtering [1]. Additionally, since patients will be part of the discharge geometry, electrical safety has to be considered: in no case high conductive currents should be delivered to the target.

To achieve an effective and selective treatment, properties of the plasma such as gas temperature, densities of reactive species and electric fields must be controllable. Atmospheric pressure air plasmas are generally known to be difficult to control both in time and space [16]. Moreover, air discharges customarily have high reactive species yields, as for example evidenced by their application as ozone generators [17], resulting in a volatile and potentially dangerous environment.

Finally, from a practical point of view, the plasma plaster must be easily adaptable to fit irregularly shaped wounds and achieve a uniformly distributed discharge, even when the spacing between the plaster and the wound is slightly unequal across the surface of the wound. Furthermore, it would be favourable if the device is transparent in the final application, such that the plasma and wound can be observed during treatment. This requires the use of (partly) transparent materials.

Summarising, the major technological challenge is to design a plasma source that is biocompatible, flexible and transparent, and produces a plasma in atmospheric pressure air that has controllable and predictable properties. Finding a suitable dielectric material is one of the key objectives. Besides largely determining biocompatibility, flexibility and transparency, the dielectric's surface properties at the air interface also influence the discharge. To achieve sufficient flexibility the powered electrode must be flexible as well.

One approach to accomplish this is by using a mesh structured electrode, instead of a more conventional solid plane electrode. Additionally, it is hypothesised that the plasma properties and their distribution along the wound may also be controlled through local electric field enhancement in the air gap by choosing the mesh pattern accordingly.

The design methodology that is employed in the development process is iterative and the mentioned requirements will be implemented stepwise. This means that the work presented in this thesis involves one specific plaster design and only concentrates on the discharge properties.

1.2 Research goals of this project

As a first step towards a plasma plaster that is suitable for the treatment of chronic wounds, the effects of a structured electrode on several discharge properties are investigated. To this end, a comparative study between a plaster with a mesh structured electrode and a plaster with a solid plane electrode is performed. Since the focus is explicitly on the effects of a structured electrode, a stainless steel secondary electrode is used instead of a biological medium.

The goal of this project is to design a dielectric barrier discharge type source with a structured electrode, and to determine the effects of the structured electrode on

- the power dissipation,
- the discharge distribution,
- the gas temperature,
- and the (reduced) electric field.

Measuring each of these parameters in an atmospheric pressure air plasma is challenging. The highly transient nature and sub-millimeter features of the discharge require careful measurement and analysis, and preclude the use of any kind of probe that is in contact with the plasma. Electrical and optical diagnostics are used to achieve the mentioned goals.

1.3 Thesis outline

The main matter of this thesis consists of two parts. In the first part, *Background and Theory*, the relevant background theory is discussed:

Chapter 2 provides a theoretical background on electrical breakdown in gases and on the discharge mechanisms in dielectric barrier discharges.

Chapter 3 explains a selection of concepts from molecular spectroscopy, which serves as the basis for understanding and interpreting the optical spectroscopic measurement.

Some more chapter specific theory in included in later chapters.

In the second part of this thesis, *Experiments and Results*, the performed measurements and results are discussed:

Chapter 4 introduces the plasma plasters and explains the design decisions that were made from electrostatic field simulations.

Chapter 5 elaborates on the pulsed power system that is used to drive the discharge and discusses the electrical properties of the plasma source obtained from current and voltage characteristics.

Chapter 6 shows the discharge mode and distribution recorded by fast imaging and tomographic techniques.

Chapter 7 discusses the gas temperatures obtained by fitting the rotational structure in the emission spectrum of N_2 using a line-by-line radiation code.

Chapter 8 compares two different approaches to calculate the reduced electric field from intensity ratios of different vibronic transitions in N_2 and N_2^+ emission spectra.

Chapter 9 summarises the conclusions of this work.

Part I

Background and Theory

Chapter 2

Cold Atmospheric Pressure Plasmas

Cold atmospheric pressure plasmas are non-thermal plasmas characterised by a background gas temperature that is close to room temperature. The low operation temperature makes cold plasmas especially suitable for the treatment of sensitive surfaces. This chapter explains how these plasmas are generated and maintained at atmospheric pressure. First, an overview of two electrical breakdown mechanisms, Townsend breakdown and streamer breakdown, is given in section 2.1. Discharges at atmospheric pressure have the tendency to become non-uniform and constricted due to thermal instability. This process and ways to prevent it are discussed in section 2.2. One method to maintain a cold plasma at atmospheric pressure is by inserting one or multiple insulating layers into the discharge gap, resulting in a dielectric barrier discharge. In section 2.3 dielectric barrier discharges are further explained.

2.1 Electrical breakdown of gases

Electrical breakdown in gases at atmospheric pressure, such as air, has been the subject of many studies in the past and is still intensively being investigated [16]. Besides potential plasma-based applications, knowledge on electrical breakdown in air is also relevant in high voltage engineering, where it is often a major aspect to actually *prevent* breakdown between two conductors or between a conductor and ground.

The physical concepts of the early stages of breakdown at atmospheric pressure are similar to those at low pressure: an initial electron is accelerated in an externally applied electric field and subsequently produces more electrons by ionising background particles. The further development discharge at atmospheric pressure is often rather different from low pressure, and heavily depends on the discharge geometry and the way the voltage is supplied [16].

Before further discussing discharges at atmospheric pressure, first two important mechanisms of electrical breakdown are explained: *Townsend breakdown* and *streamer breakdown*.

2.1.1 Townsend breakdown

In the beginning of the twentieth century, Townsend developed a theory for electric breakdown in gases that is now known as Townsend breakdown [18]. Townsend breakdown describes the breakdown process of a discharge at pressure p between two parallel plates, which are separated by a distance d. A voltage V is applied across the plates, resulting in a uniform electric field $E_0 = V/d$.

If an initial electron[1] is released at the cathode, it will gain energy from the electric field and accelerate towards the anode. When the energy of the electron is high enough to ionise a background particle, it can generate another electron by electron impact ionisation:

$$\mathrm{e} + \mathrm{M} \rightarrow \mathrm{e} + \mathrm{e} + \mathrm{M}^{+}, \tag{2.1}$$

where M indicates a background particle. This process now repeats for both electrons and so on. The result is an avalanche of electrons that propagates in the direction towards the anode. The development of an electron avalanche is illustrated in figure 2.1.

The number of electrons n_e in an avalanche can be described as a function of the distance from the cathode x:

$$\mathrm{d}n_\mathrm{e} = \alpha n_\mathrm{e}\,\mathrm{d}x, \tag{2.2}$$

$$n_\mathrm{e}(x) = n_e(0)e^{\alpha x} = e^{\alpha x}, \tag{2.3}$$

where α is the ionisation coefficient, which is defined as the number of electron impact ionisation events per unit length and depends on the electric field [19].

Since electrons have a much higher mobility than ions, a trail of ions is left behind. The total amount of ions n_ion that is created in the avalanche is

$$n_\mathrm{ion} = n_e(d) - 1 = e^{\alpha d} - 1. \tag{2.4}$$

Ultimately, these ions will drift to the cathode, where they may cause secondary electron emission. The amount of secondary electrons n_se that are released from the cathode is given by

$$n_\mathrm{se} = \gamma n_\mathrm{ion} = \gamma(e^{\alpha d} - 1), \tag{2.5}$$

[1] The initial electron is often assumed to be generated by cosmic radiation or radioactive decay.

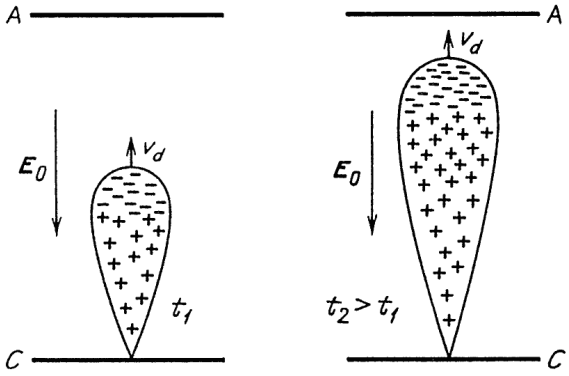

Figure 2.1: Shape and charge distribution of an electron avalanche at two consecutive moments in time t_1 and $t_2 > t_1$. The anode and cathode are indicated by 'A' and 'C', respectively. The direction of the externally applied electric field E_0 and the direction of motion of the avalanche head v_d are indicated by arrows. Taken from [19].

where γ is the secondary electron emission coefficient, which is defined as the amount electrons that are released from the cathode per incident ion [19]. The secondary electron emission coefficient is closely related to the work function of the cathode material, which determines how much energy is required to release an electron from it.

Each of the secondary electrons can now start a new avalanche. This situation becomes self-sustaining if at least one new secondary electron is produced by the ions at the cathode, resulting in the Townsend breakdown criterion:

$$\gamma(e^{\alpha d} - 1) = 1. \tag{2.6}$$

Up to now, other production and loss processes of ions and electrons, like photo-ionisation and electron attachment, have been neglected. In air plasmas, electron attachment to O_2 is an important electron loss process [16, 19, 20]:

$$\mathrm{e} + \mathrm{O_2} + \mathrm{M} \rightarrow \mathrm{O_2^-} + \mathrm{M}, \tag{2.7}$$

where M represents a third particle that is required for the conservation of energy and momentum. This can be taken into account in the Townsend theory by introducing the attachment coefficient η, which is defined as the amount of electron attachment events per unit [19]. Now α must be replaced by $\alpha - \eta$ in equation 2.2 and the Townsend criterion of equation 2.6 in this case becomes:

$$\frac{\gamma\alpha}{\alpha - \eta}(e^{(\alpha-\eta)d} - 1) = 1. \tag{2.8}$$

So, Townsend breakdown is characterised by the continuous development of electron avalanches in a uniform electric field. Using the Townsend theory, it is for example possible to derive Paschen's law, which gives the breakdown voltage V_{br} as function of the product pd [19]:

$$V_{\mathrm{br}}(pd) = \frac{Bpd}{\ln Apd - \ln[\ln(1 + 1/\gamma)]}, \tag{2.9}$$

where A and B are constants that depend on the gas composition. A Paschen curve for air is given in figure 2.2.

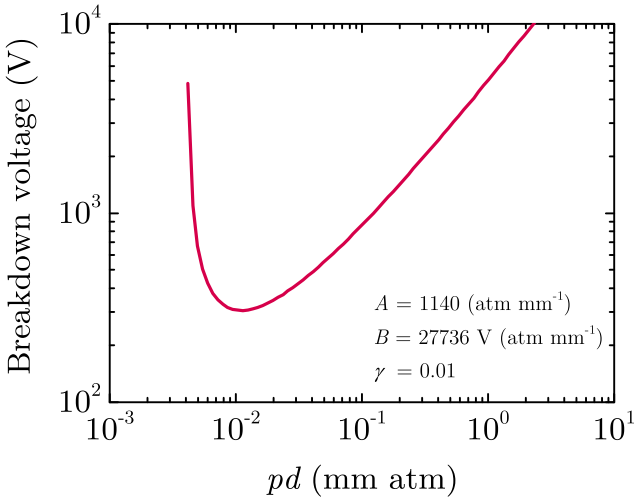

Figure 2.2: Paschen curve for air with a typical secondary electron emission coefficient of $\gamma = 0.01$. Data for A and B taken from [19].

2.1.2 Streamer breakdown

When fast breakdown processes for pd values exceeding about 1000 Torr cm $\approx$ 13 atm mm were observed that could not be explained by Townsend breakdown, Loeb [21, 22], Meek [23] and Raether [24] developed the concept of streamer breakdown. In the Townsend theory, it is assumed that the space charge of an avalanche does not influence the applied electric field E_0. Basically, streamer breakdown is an extension to the Townsend theory that does take space charge effects of a single avalanche into account.

Streamer breakdown also starts with an electron avalanche. As the number of electrons in the avalanche head grows larger during its development, space charge separation starts to locally enhance the electric field in front of the avalanche head, which results in high local ionisation rates [19]. This effect is illustrated in figure 2.3. The left part of figure 2.3 shows the externally applied field E_0 and the field E' resulting from the space charge separation separately, and the right part of the figure shows the net electric field $E = E_0 + E'$.

When the electric field due to space charge separation becomes of the same order as the external field, the avalanche will become a streamer. By comparing the electric field resulting from space charge separation in an avalanche to the applied electric field, Meek defined a criterion for the number of electrons in an avalanche that is required to initiate a streamer [19]:

$$\exp\left(\int [\alpha - \eta]\, \mathrm{d}x\right) \approx 10^8, \tag{2.10}$$

where the left hand side is a more general form of equation 2.3 and the ionisation coefficient is now depends on the local electric field. While this criterion is not really a strict criterion and the exact requirements and processes of streamer formation are more complex [20], it does show that for streamer formation the electric field must be high enough (through α) and that the gap must long enough (through x).

A streamer is a thin ionised channel that develops under the influence of the externally applied electric field enhanced by its own electric field [19]. Two types of streamers can be distinguished: positive streamers and negative streamers. Both streamer types are illustrated in figure 2.4. A positive streamer is directed towards the cathode and the streamer head contains positive charge, as shown in figure 2.4a. A negative streamer, on

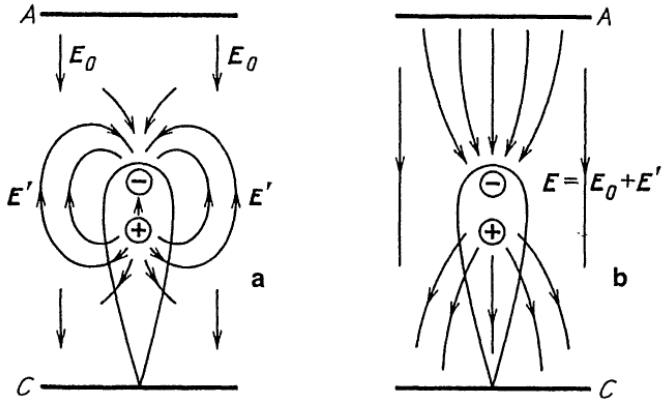

Figure 2.3: Electric fields in a gap containing an electron avalanche. In the left figure the externally applied field E_0 and the field from the space charge separation in the avalanche E' are shown separately. In the right figure the resulting total electric field $E = E_0 + E'$ is shown. Taken from [19].

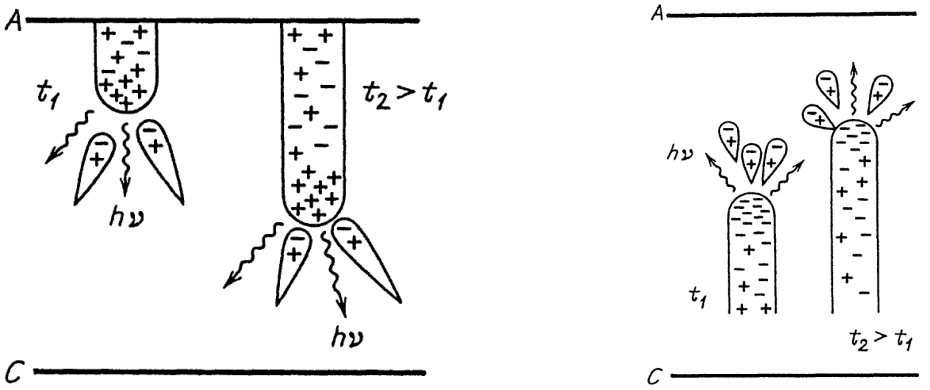

(a) Positive streamer.

(b) Negative streamer.

Figure 2.4: Shape and charge distribution of a positive streamer (a) and a negative streamer (b) at two consecutive moments in time t_1 and $t_2 > t_1$. The wavy arrows represent photons with energy $h\nu$ emitted from the streamer head. The anode and cathode are indicated by 'A' and 'C', respectively. Taken from [19].

the other hand, travels towards the anode and its head contains negative charges, which are mostly electrons [20]. A negative streamer is shown in figure 2.4b

Both streamer types develop by ionising the gas in front of the streamer head [19]. Thus the formation process requires the presence of free electrons in front of the streamer. Negative streamers can supply these electrons themselves from the streamer head. However, in positive streamers the electrons drift into the streamer body can therefore not be used for this purpose. Usually, the production of electrons in front of positive streamers is attributed to photo-ionisation by highly energetic photons that are emitted by excited molecules in the streamer head [19]. This process is also illustrated in figure 2.4. Additionally, background ionisation can also serve as a source of free electrons for the propagation of positive streamers [20]. Secondary avalanches resulting from these electrons are subsequently pulled into streamer head.

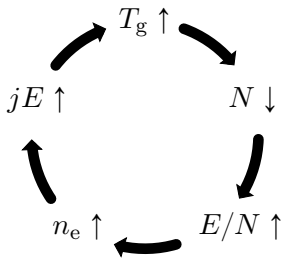

Figure 2.5: Illustration of the thermal instability. Adapted from [19].

2.2 Non-thermal atmospheric pressure plasmas

When a plasma is produced by applying an electric field across two parallel electrodes, energy is first delivered to the electrons. The energy is then transferred to the heavy particles by ionisation, excitation, dissociation of molecules and elastic collisions. In the case of molecular gases, vibrational excitation often also plays an important role [25]. Generally, the energy transfer from the electric field to the electrons is much more efficient than the energy transfer between electrons and heavy particles through collisions, which results in a non-thermal plasma where the gas temperature remains much smaller than the electron temperature [1–4, 25].

However, due to high collision rates and hence low diffusion rates, discharges at atmospheric pressure are prone to thermal instabilities [19, 25]. When the discharge is allowed to develop, (local) heating of the gas tends to result in non-uniformities and discharge contraction. This process is illustrated in figure 2.5 and can be understood as follows [19, 20]: An increase in gas temperature T_g results in a decrease in the gas density N. When a constant electric field E is applied, this results in an increase of the reduced electric field E/N. The reduced electric field can be regarded as a measure for the amount of energy an electron obtains from the field E along its mean free path $\lambda_{mfp} \propto 1/N$ between successive collisions. An increase in E/N consequently results in a higher ionisation rate and thereby in a higher electron density n_e. Now the conductivity and conduction current density j rise, leading to an increase in power dissipation by Joule heating jE, which further increases the gas temperature.

Several steps can be taken to prevent the development of a thermal instability in an atmospheric pressure plasma. Heating of heavy particles occurs on a time scale from approximately 100 ns to 1 µs [25]. So by using nanosecond voltage pulses, heating of the gas can be prevented. Another common approach is to insert a dielectric barrier between the electrodes. In this case the barrier limits the current density and thereby the heating of the gas. The resulting discharge is called a dielectric barrier discharge (DBD) and is explained in more detail in the next section.

2.3 Dielectric barrier discharges

Dielectric barrier discharges have been studied for over a century. The first experimental investigations were reported by Siemens in 1857, whose worked focused on ozone generation [17]. Today, DBDs in air or oxygen are still used in industrial ozone production. Additionally, DBDs are also used in pollution control, plasma enhanced chemical vapour deposition (PECVD), CO_2 lasers, excimer lamps and plasma displays [17, 20, 26–28].

Some typical parallel plane DBD configurations are illustrated in figure 2.6. In each case at least one dielectric barrier is present between the electrodes. The barrier can be

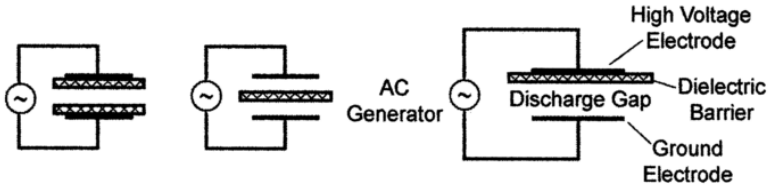

Figure 2.6: Several possible planar DBD geometries. In each case at least one dielectric is present between the electrodes. Taken from [17].

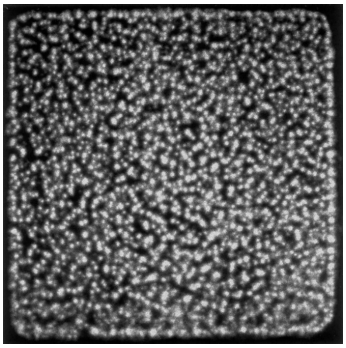

Figure 2.7: Top view through a transparent electrode of a filamentary DBD in air. The light spots indicate the locations of the filaments. Taken from [17].

positioned at either or both of the electrodes or between the electrodes. Besides the planar arrangements, coaxial configurations and surface discharge geometries exist as well [17, 26, 28]. The presence of the dielectric barrier precludes direct current (DC) operation. Instead, alternating current (AC) or pulsed excitation has to be used.

When breakdown occurs, charges are accumulated at the dielectric barrier(s) and generate a local electric field opposite to the applied field, which consequently inhibits the discharge. As long as the applied voltage is high enough, subsequent discharges strike at other locations where the electric field is still high. These local and self-limiting discharges are often called microdischarges [17, 26, 28]. The deposited charges facilitate a new microdischarge at the same location when the polarity of the applied is reversed. This is known as the memory effect and results in the visible filaments that most DBDs exhibit. The photograph in figure 2.7 shows a top view of the distribution of filaments in a filamentary DBD in air through a transparent electrode. So, DBDs operating in this *filamentary mode* are not uniform and consist of numerous filaments that are distributed in the discharge gap.

Besides the just described filamentary mode, DBDs can also operate in a *diffuse mode* that is free of filaments. While the filamentary mode is often associated with streamer breakdown and the diffuse mode with Townsend breakdown [29], the exact conditions to obtain a diffuse DBD at atmospheric pressure are currently not yet fully understood. Diffuse DBDs are most often achieved in air with an admixture of helium [16], and by using alumina (Al_2O_3) electrodes [30]. Additionally, it is proposed that pre-ionisation [31, 32], a low surface resistance of the dielectric barrier [33], and electronic stabilisation [34] may facilitate a diffuse DBD. Several of these concepts are further explored in the discussion of Chapter 6.

Examples of a filamentary DBD and a diffuse DBD and their corresponding typical voltage and current characteristics are shown in figure 2.8. In figure 2.8a the current pulses

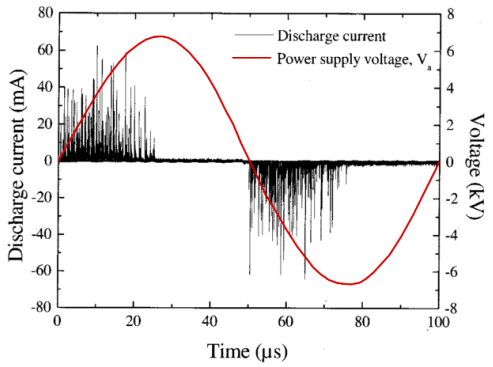

(a) Voltage and current for a filamentary DBD.

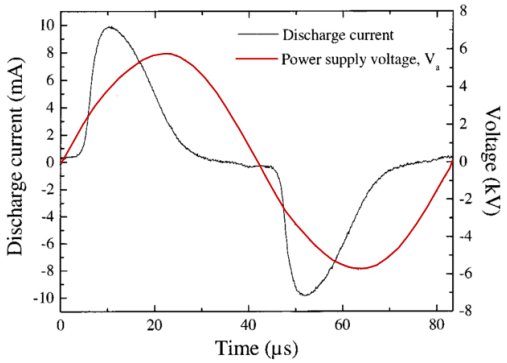

(b) Voltage and current for a diffuse DBD.

(c) Photograph of a filamentary DBD.

(d) Photograph of a diffuse DBD.

Figure 2.8: Examples of typical voltage and current characteristics for a filamentary DBD (a) and a diffuse DBD (b) and photographs of the discharge gap for a filamentary DBD (c) and a diffuse DBD (d) with an exposure time of 10 ns. Both discharges are operated in pure nitrogen at atmospheric pressure. Taken from [31].

of individual microdischarges associated with a filamentary DBD can clearly be observed in the current signal. In the case of a diffuse DVD there is a single broad discharge current peak, as shown in figure 2.8b. Figures 2.8c and 2.8d show photographs of a filamentary and a diffuse DBD respectively. The pictures are taken with an intensified charge coupled device (ICCD) camera with an exposure time of 10 ns. For the filamentary discharge the plasma channels of several microdischarge are visible, while for the diffuse discharge the plasma is distributed more homogeneously and no filaments are present.

It should be noted that in literature a variety of names is used by different authors to indicate a diffuse DBD. Okazaki *et al*, who started the study on diffuse DBDs in 1987, used the term atmospheric pressure glow discharge (APGD) [35]. Roth *et al*, who investigated many possible applications of diffuse DBDs, use the term one atmosphere uniform glow discharge plasma (OAUGDP) [36]. Finally, Massines proposes a distinction between a glow DBD (GDBD), which mostly occurs in larger gaps and has the spatial structure of a low pressure glow discharge, and a Townsend DBD (TDBD), which resembles a low pressure Townsend discharge [29]. In this thesis the term diffuse DBD or simply 'diffuse discharge' is used.

Chapter 3

Structure and Spectra of Diatomic Molecules

Spectroscopic diagnostics are a powerful tool in the characterisation of atmospheric pressure air plasmas. Numerous properties of the plasma can be determined by measuring the spectral intensity of the light that is emitted. In Chapter 7 the emission spectrum of N_2 is used to obtain the gas temperature and in Chapter 8 the emission spectra of N_2 and N_2^+ are used to infer the reduced electric field. To understand and analyse the measured spectra, some fundamental knowledge of the energy level structure and transitions in diatomic molecules is required. This chapter provides a background on these two subjects and serves as the basis for a line-by-line radiation code that will be presented in Chapter 7. Section 3.1 explains the energy structure of diatomic molecules and section 3.2 discusses the emission spectra that result from radiative transitions between different energy states in a diatomic molecule. Evidently, a full exploration of molecular spectroscopy is outside the scope of this thesis and more details can be found in found in [37–40].

3.1 Structure of diatomic molecules

Diatomic molecules consist of two nuclei surrounded by orbiting electrons. As in the case of atoms, the Coulomb force mediates the interaction between the electrons and the nuclei. Since there are two nuclei, relative motion with respect to each other along the internuclear axis and about the centre of mass is possible, resulting in vibrational and rotational motion respectively. Just like the electronic states of atoms, different discrete electronic, vibrational and rotational states exist for molecules, with corresponding quantised energy levels E_e, E_{vib} and E_{rot} respectively.

Typically, the energy separating the electronic levels is much larger than that between the vibrational levels, which, on its turn, is still much larger than the energy separation between rotational levels:

$$\Delta E_e \gg \Delta E_{\text{vib}} \gg \Delta E_{\text{rot}}. \tag{3.1}$$

This suggests a molecular energy structure where a given electronic level contains many vibrational levels, and a vibrational level contains numerous rotational levels, as illustrated in figure 3.1. To understand the exact structure of energy levels in diatomic molecules the energies associated with the different types of motions are now analysed in more detail.

The attainable energy levels in a molecule follow from the time independent Schrödinger equation, which in case of a diatomic molecule with N electrons is given by

$$\frac{\hbar}{2m_e}\sum_{i=1}^{N}\nabla_i^2\Psi + \frac{\hbar}{2}\sum_{k=1}^{2}\frac{1}{M_k}\nabla_k^2\Psi + (E-V)\Psi = 0, \tag{3.2}$$

where Ψ is the wave function and E is the energy of the state, m_e is the electron mass, in the case of a homonuclear diatomic molecule $M_1 = M_2 = M$ is the mass of each of the nuclei, and V is the potential, which contains all interactions. The subscript on the Laplacian indicates that it operates with respect to the coordinates of the i^{th} electron or the k^{th} nucleus. The difficulty of finding a solution to this equation is due to V and, just like the case of multi-electron atomic systems, no exact solutions are known.

To obtain an approximate solution, the Born-Oppenheimer approximation can be used. This approximation assumes that the electrons move very fast compared to the nuclei and that they are therefore able to adjust themselves to the motion of the nuclei instantaneously. In the Born-Oppenheimer approximation the electronic and nuclear parts of the wave function and their contribution to the total energy of a state are separated. Subsequently, the nuclear part is further separated into a vibrational and rotational part,

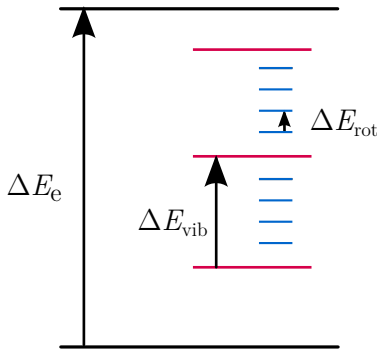

Figure 3.1: Schematic energy diagram for a molecule showing electronic levels (black lines), vibrational levels (red lines) and rotational levels (blue lines).

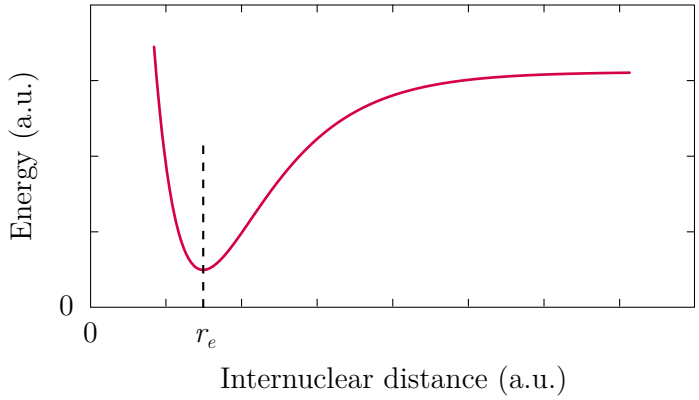

Figure 3.2: Typical shape of the molecular potential energy as function of the internuclear distance. The equilibrium separation at the minimum of the curve is indicated by r_e.

resulting in

$$\Psi = \Psi_{\mathrm{e}} \cdot \Psi_{\mathrm{vib}} \cdot \Psi_{\mathrm{rot}}, \tag{3.3}$$

$$E = E_{\mathrm{e}} + E_{\mathrm{vib}} + E_{\mathrm{rot}}. \tag{3.4}$$

The electronic part is used to calculate a molecular potential energy curve, which is then used to solve the vibrational and rotational parts of the Schrödinger equation. A typical example of the molecular potential as function of the internuclear distance is shown in figure 3.2.

In spectroscopy, energies are traditionally expressed in wave numbers (units cm^{-1}) and equation 3.4 is written as

$$T = \frac{E}{hc} = T_e + G(v) + F(J), \tag{3.5}$$

where T_e represents the electronic *term energy* and $G(v)$ and $F(J)$ are the vibrational and rotational term energies respectively. Expressions for these term energies and their dependence on the vibrational quantum number v and rotational quantum number J are now discussed.

3.1.1 Vibrational energy

When a molecule vibrates, the internuclear separation oscillates periodically about its equilibrium distance, which corresponds to the minimum of the molecular potential curve. If the variation in separation is small with respect to the equilibrium, the potential can be approximated by a parabola. This results in the well-known quantum harmonic oscillator, with discrete energies given by

$$E_{\mathrm{vib}}(v) = \hbar\sqrt{\frac{2k}{M}}(v + \frac{1}{2}), \tag{3.6}$$

where k is a constant depending on the shape of the potential. In terms of wave numbers the expression for the vibrational energy levels becomes

$$G(v) = \frac{E_{\mathrm{vib}}(v)}{hc} = \omega_e(v + \frac{1}{2}), \tag{3.7}$$

where ω_e is the vibrational frequency in wave numbers and is dependent on the electronic state (through k). For larger deviations from the equilibrium distance, the molecular potential can no longer be approximated by a parabola and higher order terms are required. This results in the anharmonic oscillator model, with corresponding energies:

$$G(v) = \omega_e(v + \frac{1}{2}) - \omega_e x_e(v + \frac{1}{2})^2 + \omega_e y_e(v + \frac{1}{2})^3 - \ldots, \tag{3.8}$$

where $\omega_e x_e$ and $\omega_e y_e$ represent higher order corrections to the harmonic oscillator energies.

Contrary to the harmonic oscillator, the anharmonic model also accounts for dissociation. If the distance between the nuclei becomes large enough, their covalent bond breaks and as a result further separation of the nuclei does not require additional energy. The energy at which this happens is the dissociation energy.

3.1.2 Rotational energy

To obtain an expression for the rotational energy levels, the molecule is first modeled as a rigid rotor by keeping the internuclear separation fixed at the equilibrium distance. The rotational part of equation 3.2 can in this case be solved by inserting $V = 0$ and leads to rotational energy levels given by

$$E_{\text{rot}}(J) = \frac{\hbar^2 J(J+1)}{2I}, \tag{3.9}$$

where $I = \frac{1}{2}Mr^2$ is the moment of inertia of the two nuclei about their centre of mass in the direction perpendicular to the internuclear axis. In terms of wave numbers the expression for the rotational energy levels becomes

$$F(J) = \frac{E_{\text{rot}}}{hc} = B_e J(J+1), \tag{3.10}$$

where B_e is the rotational constant for a given electronic state of the molecule.

However, if there is vibrational motion, the molecule cannot be approximated by a rigid rotor. When the distance between the nuclei changes, the moment of inertia also changes. Again higher order correction terms of $J(J+1)$ are included in the rotational energy term to account for this:

$$F(J) = B_e J(J+1) - D_e[J(J+1)]^2 + H_e[J(J+1)]^3 - \ldots, \tag{3.11}$$

where D_e and H_e are higher order rotational constants. D_e is often referred to as the centrifugal distortion constant.

One result of the anharmonic oscillator model for vibrations is that the equilibrium distance shifts to larger values for higher vibrational levels. This leads to another correction that is implemented by making the rotational constants dependent on the vibrational level

$$F(v, J) = B_v J(J+1) - D_v[J(J+1)]^2 + H_v[J(J+1)]^3 - \ldots, \tag{3.12}$$

with

$$B_v = B_e - \alpha_e(v + \frac{1}{2}) + \gamma_e(v + \frac{1}{2})^2 + \ldots, \tag{3.13}$$

$$D_v = D_e - \beta_e(v + \frac{1}{2}) + \epsilon_e(v + \frac{1}{2})^2 + \ldots. \tag{3.14}$$

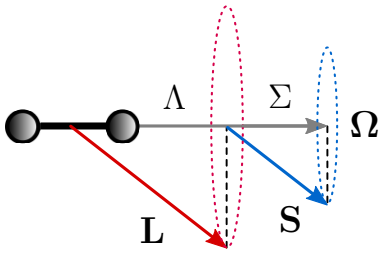

Figure 3.3: Precession of the electronic orbital angular momentum **L** and the electronic spin angular momentum **S** about the internuclear axis. The projections along the internuclear axis, Λ and Σ, together constitute the total electronic angular momentum about the internuclear axis $\Omega = \Lambda + \Sigma$ and the corresponding vector $\mathbf{\Omega}$.

Often the vibrational and rotational term energies are stated together in a more general way by the Dunham expansion:

$$T(v, J) = G(v) + F(v, J) = \sum_m \sum_n Y_{mn} (v + \frac{1}{2})^m \left[J(J+1)\right]^n , \tag{3.15}$$

where the constants Y_{mn} are called Dunham coefficients.

3.1.3 Coupling of electronic and rotational motion

Thus far, the interaction between vibrational and electronic motion has been taken into account by fitting the vibrational levels to the molecular potential curve, and the interaction between vibrational and rotational motion has been included through equation 3.12. Finally, the influence of the electronic motion on the rotational energy needs to be considered. To do this, first some properties of electronic states without rotation are briefly discussed.

Electronic states

In a diatomic molecule the electrons move in a field that has axial symmetry about the internuclear axis. As a result, the electronic orbital angular momentum **L** precesses about the internuclear axis, as shown in figure 3.3. Its component of along the internuclear axis, M_L, is a constant of motion can take the values

$$M_L = -L, -L+1, \ldots, L-1, L. \tag{3.16}$$

In the absence of a magnetic field, the energy of the state is invariant under a change of sign in M_L. Electronic states of diatomic molecules are therefore classified by the quantum number Λ, which is defined as

$$\Lambda = |M_L|. \tag{3.17}$$

States with $\Lambda \neq 0$ are thus doubly degenerate. For $\Lambda = 0, 1, 2, 3 \ldots$ the corresponding electronic state is designated Σ, Π, Δ, $\Phi \ldots$ respectively.

Just like atoms, the combined spin of individual electrons results in the electronic spin angular momentum **S**, which is also indicated in figure 3.3. The corresponding quantum number S is either an integer or half-integer, depending whether the total number of electrons is even or odd. The electron spin angular momentum also has a component along the internuclear axis, M_S, which can take the values

$$M_S = -S, -S+1, \ldots, S-1, S. \tag{3.18}$$

Conventionally, M_S is denoted by the quantum number Σ,

$$\Sigma = M_S, \tag{3.19}$$

which should not confused with the symbol Σ that is used to indicate $\Lambda = 0$ states. So, for each value of S, there are $2S+1$ possible values for Σ, which is called the *spin multiplicity* of an electronic state.

Together the electronic orbital and spin angular momenta constitute the total electronic angular momentum $\mathbf{\Omega}$. The total electronic angular momentum has a component Ω along the internuclear axis that is given by

$$\Omega = \Lambda + \Sigma. \tag{3.20}$$

The three quantum numbers Λ, S and Ω form the basis of the *molecular term symbol* notation describing the electronic state:

$$^{2S+1}\Lambda_{\Omega}. \tag{3.21}$$

Besides the angular momenta, symmetry properties of the electronic wavefunction are important as well. In a diatomic molecule, any plane through the internuclear axis is a symmetry plane. The electronic wavefunction Ψ_e of a non-degenerate state ($\Lambda = 0$) can either remain unchanged or changes sign when reflected through a symmetry plane. In the first case, the state has a '+' symmetry and in the second case it has a '−' symmetry. This symmetry property is indicated by a superscripted plus or minus sign.

Additionally, in homonuclear diatomic molecules the nuclei also have a point symmetry at the midpoint of the internuclear axis. When the electronic wavefunction Ψ_e is reflected through this point, it also either remains unchanged or it changes sign. In the first case, the state is an *even* state and in the second case the sate is an *odd*. The even or odd symmetry is indicated by a subscripted 'g' or 'u' respectively (from the German words *gerade* and *ungerade*).

Including symmetry properties, the full notation used to label electronic states becomes

$$^{2S+1}\Lambda^{(\pm)}_{\Omega\,(\mathrm{g,u})}. \tag{3.22}$$

Often this label is paired with an empirical single letter label to explicitly indicate whether an electronic state is the ground state (X), or an excited state (in order of ascending energy A, B, C...). For example, the ground state of N_2 in this notation is given by $X\,^1\Sigma^+_g$.

Hund's coupling cases

Now the interaction between electronic motion and the nuclear rotation is considered. The electronic angular momenta ($\mathbf{L}$ and $\mathbf{S}$) and the angular momentum of nuclear rotation $\mathbf{N}$ together form the total angular momentum of the molecule, which is indicated by $\mathbf{J}$. Depending on which interactions are dominant, several types of coupling, called Hund's cases, can be distinguished. Of the five cases, named (a) through (e), only Hund's case (a) and (b) are relevant for the analysis in Chapter 7 and Chapter 8, and therefore only these two cases will be discussed.

Hund's case (a) In this case both $\mathbf{L}$ and $\mathbf{S}$ are strongly coupled to the internuclear axis, and the interaction between electronic motion and nuclear motion is very weak. This means $\mathbf{\Omega}$ is well defined. The total angular momentum $\mathbf{J}$ is formed by addition of $\mathbf{\Omega}$ and the angular momentum of nuclear rotation $\mathbf{N}$. A vector diagram illustrating

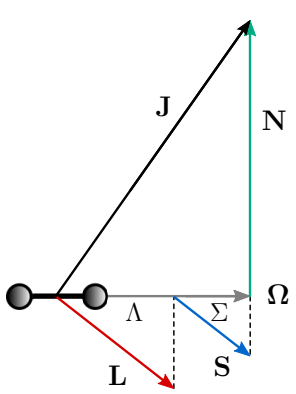

(a) Vector diagram for Hund's case (a).

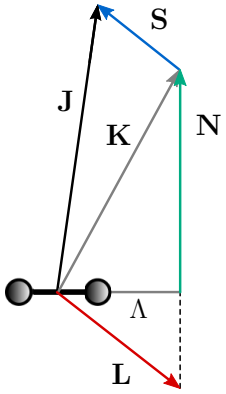

(b) Vector diagram for Hund's case (b).

Figure 3.4: Vector diagrams illustrating coupling for Hund's cases (a) and (b).

this coupling is shown in figure 3.4a. The energy in this type of coupling can be described by a so-called *symmetric top* model. Neglecting the higher order correction terms for a moment, the rotational term energy for Hund's case (a) is

$$F(v, J) = B_v[J(J+1) - \Omega^2] + A\Omega^2, \tag{3.23}$$

where the term $A\Omega^2$ is constant for a given electronic state and is therefore often included in T_e. Here J can take the values

$$J = \Omega,\ \Omega+1,\ \Omega+2, \ldots \tag{3.24}$$

Hund's case (b) This case is characterised by very weak coupling of **S** to the internuclear axis. As a result, **Ω** is not defined. Now the electronic orbital angular momentum **Λ** and the angular momentum of nuclear rotation **N** form the *total angular momentum apart from spin* **K**. The corresponding quantum number K can have values

$$K = \Lambda,\ \Lambda+1,\ \Lambda+2, \ldots \tag{3.25}$$

Next, **K** and **S** together form the total angular momentum **J**. A vector diagram illustrating this coupling is shown in figure 3.4b. In this case J can take the values

$$J = |K-S|,\ |K-S|+1,\ \ldots,\ (K+S-1),\ (K+S). \tag{3.26}$$

So, for a given K, each rotational level J consists of $2S+1$ components, which is equal to the spin multiplicity of the state. To illustrate, consider a $^2\Sigma$ state ($\Lambda = 0$, $S = 1/2$). Now the rotational term energy has two components:

$$F_1(v, K) = B_v K(K+1) + \frac{1}{2}\gamma K \tag{3.27}$$

$$F_2(v, K) = B_v K(K+1) - \frac{1}{2}\gamma(K+1), \tag{3.28}$$

where F_1 corresponds to the components with $J = K + 1/2$ and F_2 corresponds to the components with $J = K - 1/2$. The splitting constant γ is generally very small compared to B_v

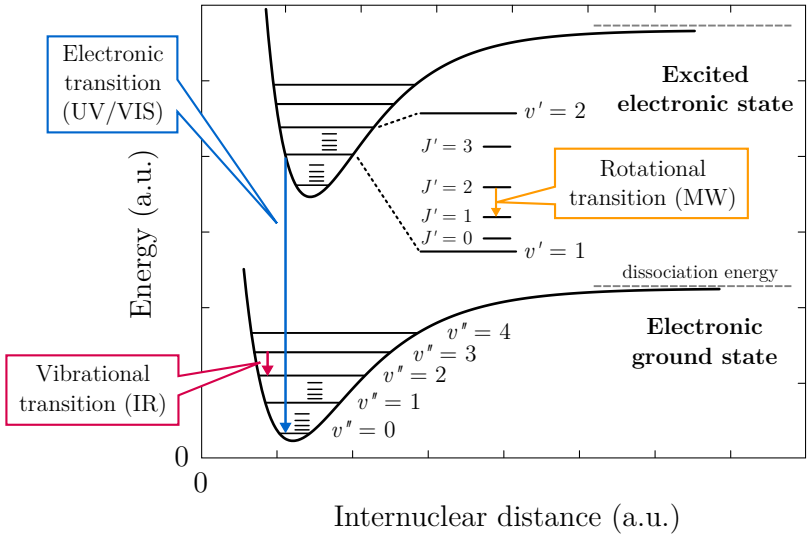

Figure 3.5: Schematic energy level diagram of a molecule. Examples of electronic, vibrational and rotational transitions are indicated by the blue, red and orange coloured arrows respectively.

A few things should be noticed when comparing these two cases. Firstly, for singlet states ($S = 0$) there is no distinction between case (a) and (b), because now $\Lambda = \Omega$ and $K = J$.

Σ states ($\Lambda = 0$) with a spin multiplicity higher than 1 ($S \neq 0$) cannot belong to Hund's case (a), because in this case the spin is not coupled to the internuclear axis at all and hence Ω is not defined.

Finally, it must be realised that Hund's cases represent idealised cases and that in reality often *intermediate* coupling cases apply. Furthermore, molecules can move from one coupling case to another as their rotation increases. Nevertheless, Hund's cases often represent the molecular structure to a good approximation.

With the knowledge of this section, a more precise energy level diagram of a typical diatomic molecule can now be made. Figure 3.5 shows two molecular potential curves, one for the electronic ground state and the other for an excited electronic state. The potential curves for different electronic states do generally not have the same shape. Both curves contain vibrational levels, whose energy separation decreases for increasing quantum numbers v, as a result of the anharmonicity of the potential. The energy separation of the rotational levels on the other hand increases approximately linearly with J for not too high quantum numbers J.

3.2 Spectra of diatomic molecules

Now transitions between different molecular states can be considered. When a molecule is in a state Ψ_i with corresponding energy E_i, it can decay to a state Ψ_k of energy $E_k < E_i$ by emitting a photon which carries off the excess energy:

$$E_{\text{photon}} = h\nu = E_i - E_k. \tag{3.29}$$

Depending on what type of transition takes place, this photon can be emitted in different regions of the electromagnetic spectrum. Pure rotational transitions emit in the

microwave (MW) region. Vibrational transitions and vibrational transitions accompanied by a rotational transition (a *rovibrational* transition) emit in the infrared (IR) region. And finally, electronic transitions, electronic transitions accompanied by a vibrational transition (a *vibronic* transition) and electronic transitions accompanied by a vibrational and rotational transition (a *rovibronic* transition) emit in the ultraviolet (UV) and visible (VIS) region. Transitions between different electronic, vibrational and rotational states are also indicated figure 3.5. Since each molecule has its own set of energy levels, the spectrum resulting from all different transitions is a fingerprint of the molecule.

A specific transition can be specified by the electronic, vibrational and rotational quantum numbers n, v and J of the upper state and the lower state. Conventionally, the quantum numbers of the upper state are primed ($'$) and the those of the lower state are doubly primed ($''$): $\Psi_i = \Psi_{n'v'J'}$ and $\Psi_k = \Psi_{n''v''J''}$. Whether a specific transition is possible and what its probability is can be calculated from the wavefunctions of the involved states.

3.2.1 Transition moment and selection rules

The probability of a transition between two states is proportional to the square of electric dipole transition moment $|\mathbf{R}^{n'\,v'\,J'}_{n''v''J''}|^2$, where

$$\mathbf{R}^{n'\,v'\,J'}_{n''v''J''} = \int \Psi^*_{n'v'J'} \mathbf{M} \Psi_{n''v''J''}\, \mathrm{d}\tau. \tag{3.30}$$

In this equation $\mathbf{M}$ is the electric dipole moment of the molecule and the integration over τ includes all electronic and nuclear coordinates. Using equation 3.3, $\mathbf{R}^{n'\,v'\,J'}_{n''v''J''}$ can be separated into three contributions depending only on the electronic, vibrational and rotational part. Consequently, $|\mathbf{R}^{n'\,v'\,J'}_{n''v''J''}|^2$ can be separated as well:

$$|\mathbf{R}^{n'\,v'\,J'}_{n''v''J''}|^2 = |R^{n'}_{n''}|^2\, q^{v'}_{v''}\, S^{J'}_{J''}, \tag{3.31}$$

where $R^{n'}_{n''}$ is the electronic transition moment, $q^{v'}_{v''}$ is known as the Franck-Condon factor and $S^{J'}_{J''}$ is called the Hönl-London factor, but is also frequently referred to as the *line strength*.

If any of the factors in equation 3.31 is zero, that particular transition is said to be forbidden. This fact can be used to establish a set of selection rules for allowed transitions. Because only transitions involving an electronic transition are used in the measurements presented in this thesis, only the selection rules relevant for transitions including an electronic transitions are mentioned.

The selection rules that are generally valid for rovibronic transitions are

- $\Delta J = \pm 1$,
- $\Delta J = 0$ only if $\Lambda \neq 0$ in either the upper or lower state,
- g $\leftrightarrow$ u is allowed, but g $\leftrightarrow$ g and u $\leftrightarrow$ u are forbidden

From the first two selection rules follows that the rotational structure of a $(n', v') \rightarrow (n'', v'')$ transition consists of three branches, which are named the P-, Q- and R-branch:

- P-branch: $\Delta J = J'' - J' = -1$
- Q-branch: $\Delta J = J'' - J' = 0$
- R-branch: $\Delta J = J'' - J' = +1$

Apart from these general selection rules, there are additional selection rules that are related to the different coupling cases. Some of these selection rules apply to both Hund's case (a) and Hund's case (b) and some only hold when the upper and lower state both belong to same case. These additional selection rules can be found in [37].

3.2.2 Line intensity

The allowed transitions result in a number of *spectral lines* which constitute the emission spectrum. When the intensities in a spectrum are considered, it not only important know that the transition moment is non-zero, but also what the actual transition probability is. From wave mechanics it follows that the Einstein transition probability for spontaneous emission $A^{n'\,v'\,J'}_{n''v''J''}$ is given by

$$A^{n'\,v'\,J'}_{n''v''J''} = \frac{64\pi^4}{3h}\nu^3 \frac{\sum |R^{n'\,v'\,J'}_{n''v''J''}|^2}{g_{J'}}, \tag{3.32}$$

where ν is the frequency of the emitted photon, $g_{n'v'J'}$ is the degeneracy of the upper state and the sum $\sum |R^{n'\,v'\,J'}_{n''v''J''}|$ is taken over the degenerate states of the upper and lower levels of the transition.

If there are $n_{n'v'J'}$ molecules in the upper state then the intensity of the spectral line is given by

$$I^{\,n'\,v'\,J'}_{n''v''J''} = n_{n'v'J'} \cdot h\nu \cdot A^{n'\,v'\,J'}_{n''v''J''}. \tag{3.33}$$

Part II

Experiments and Results

Chapter 4

Plasma Plasters and Electrostatic Field Simulations

In this chapter the plasma plasters are introduced and the design decisions are explained. To study the effects of a structured electrode, two plaster types were made: one with a square mesh structured electrode and another with a solid plane electrode. Their features are described in section 4.1. Together with a stainless steel secondary electrode, the plasters form a dielectric barrier discharge cell. The secondary electrode and the complete discharge cell are presented in section 4.2. In the design process, electrostatic simulations were performed to predict and compare the combined effects of a structure electrode and barrier thickness on the electric field distribution. In section 4.3 the results for both plaster types are presented and discussed.

4.1 Plasma plasters

The devices that are investigated are named *plasma plasters*. This name was chosen because they are intended to be applied to the skin or to a wound in the same way as a conventional plaster. At the same time, they serve as the powered electrode and barrier of a dielectric barrier discharge geometry. This means that the plasters at least contain

- a conductive part that can be connected to a power supply;
- a dielectric part that functions as barrier.

The two plasters that are used in the experiments are shown in figure 4.1. A 18 µm thick nickel-gold (NiAu) plated copper layer is printed on a polyimide base layer. The NiAu layer is conductive and serves as powered electrode. Additionally, a 50 µm thick cover layer, which consist of a 25 µm thick polyimide film and a 25 µm thick silicone adhesive, is applied to the centre part of the device and functions as a dielectric barrier. A power supply can be connected at the bottom rectangular extension, where the conductive layer is partly exposed.

The main difference between the two plasters is the structure in the centre part of the conductive layer. One has a square mesh structured electrode (figure 4.1a) and will be referred to as the **meshed plaster**, and the other has a solid plane electrode (figure 4.1b) and will be referred to as the **plane plaster**. Generally, a discharge will concentrate where the separation is smallest when a plane electrode is used in combination with an irregularly shaped surface such as a wound, leading to an uneven treatment. As will be shown in section 4.3, using a mesh structured electrode results in local electric field enhancement, which may potentially be used to distribute the discharge more evenly. The effects of a mesh structured electrode on the discharge properties are investigated experimentally and compared to the plane plaster.

The structured part of the meshed plaster consists of conductive channels with a thickness of 0.12 mm and the separation between parallel channels is 0.9 mm. The mesh structure and dimensions of the plaster are illustrated in figure 4.2. The exterior dimensions of the plane plaster are the same as for the meshed plaster.

Polyimide based plasters with a printed electrode were chosen because this provides freedom in designing the structure of the mesh. Virtually any pattern can be printed and used as an electrode. Furthermore, polyimide materials have a dielectric strength of about 268 to 339 kV/mm [41], which should be sufficiently high to prevent dielectric breakdown in the present case.

4.2 Discharge cell

Besides the plaster, a secondary electrode is required to complete the discharge cell. To focus on the effects of a mesh structured electrode, a stainless steel secondary electrode with a diameter of 6 mm is used instead of a biological medium. Stainless steel is chosen to prevent the formation of oxide layers on the electrode surface.

The secondary electrode is positioned above the centre part of the plaster. To ascertain that the plaster and the secondary electrode are parallel they are both placed in a holder. Additionally, the secondary electrode is attached to a screw gauge micrometer to have accurate control of the gap width. A photograph of the assembled holder is shown is figure 4.3. The holder can be mounted to one or multiple linear or rotating stages to ease the alignment for optical diagnostics.

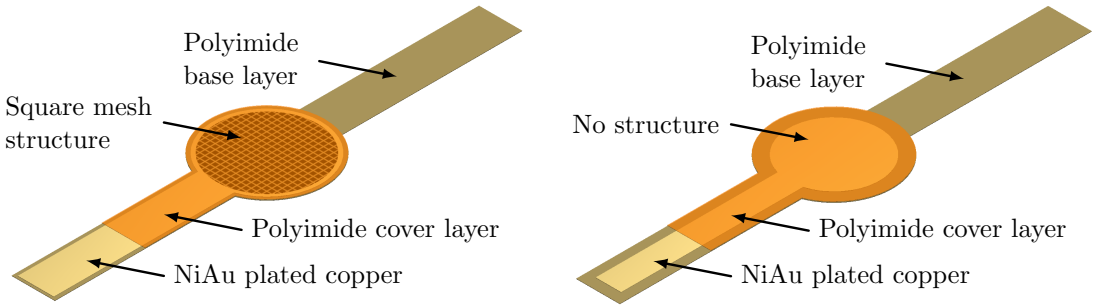

(a) Meshed plaster **(b)** Plane plaster

Figure 4.1: Schematic drawing of the meshed plaster (a), and the plane plaster (b).

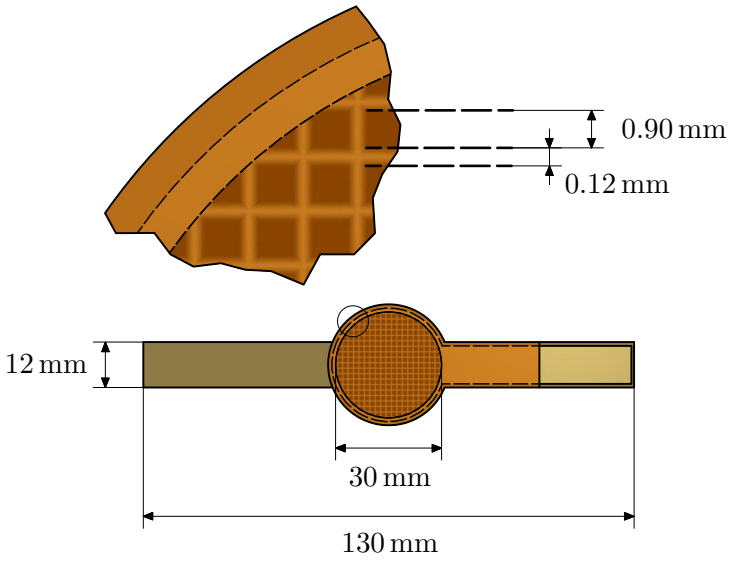

Figure 4.2: Schematic sketch of the meshed plaster. The top part is a zoomed view of the encircled part.

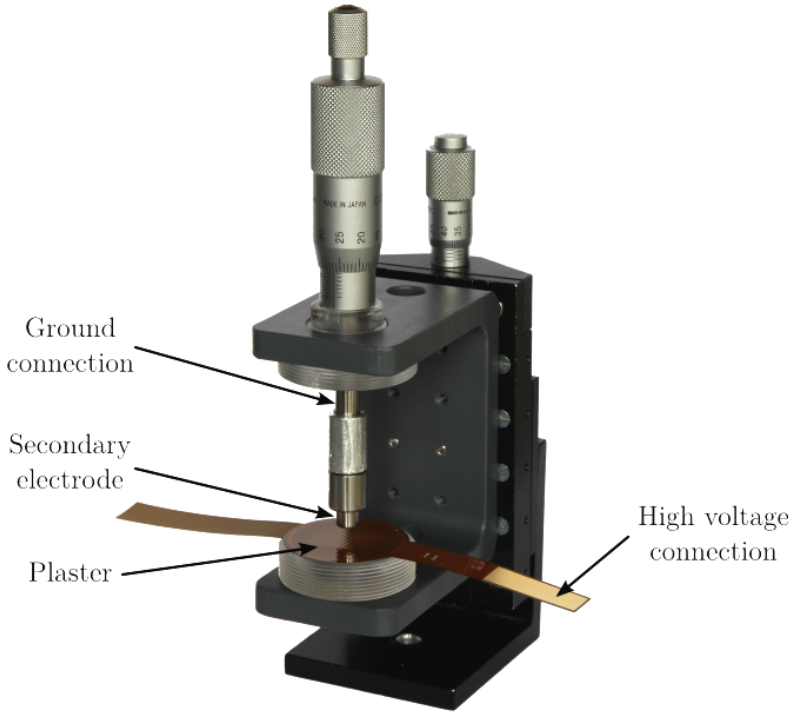

Figure 4.3: Photograph of the assembled holder. The backside of the 'U'-shaped PVC part (dark grey) has multiple threaded holes to attach it to a linear slide or stage in different orientations.

4.3 Electrostatic simulation of the electric field

To predict and compare the electric field distribution resulting from a certain mesh pattern and barrier thickness, an electrostatic model was built using Comsol Multiphysics. In this model the circular centre part of the plasters is simulated. The properties of the model will be explained first and then the results for the meshed plaster and the plane plaster are shown and discussed.

4.3.1 Model

To start, an appropriate model geometry has to be constructed. Because the plane plaster has cylindrical symmetry, a 2D axisymmetric geometry is used. The centre part of the meshed plaster has no axial symmetry, so in this case a 3D geometry is required. However, the centre part of the meshed plaster does have a periodic structure which is mapped onto itself under rotation by a multiple of 90° about the axis through its centre. Therefore, it suffices to model a single quarter of the meshed plaster and apply periodic boundary conditions to the cut planes[1].

In each case the air gap between the plaster and the secondary electrode is set to 0.5 mm. The relative permittivity of the barrier is set to $\varepsilon_r = 4$ to approximately represent the polyimide film and silicone adhesive. The model domain must be sufficiently large to include fringing fields. Furthermore, the computational grid needs to be sufficiently dense in the dielectric barrier and in the gap between the plaster and secondary electrode to successfully capture local electric field enhancement. These conditions are met once there

[1] In fact, the geometry could be further reduced by realising that a single quarter of the centre part exhibits a reflection symmetry along its bisector. This is however not implemented in the presented model.

are no further changes in the electric field when either the model domain or the grid density is further increased. A voltage of 5 kV is applied to the plaster and the secondary electrode is grounded.

The local potential V and electric field $\mathbf{E}$ are calculated by solving Gauss's law on the grid:

$$-\nabla \cdot \varepsilon \nabla V = 0, \tag{4.1}$$

with

$$-\nabla V = \mathbf{E}. \tag{4.2}$$

Furthermore, a homogeneous Neumann condition is applied to the open boundaries of the model domain:

$$\hat{\mathbf{n}} \cdot \nabla V = \frac{\mathrm{d}V}{\mathrm{d}\hat{\mathbf{n}}} = 0, \tag{4.3}$$

where $\hat{\mathbf{n}}$ is the unit vector normal to the boundary surface.

4.3.2 Results and discussion

In figures 4.4 through 4.9, a side-by-side comparison of the electric field strengths for the plane plaster and the meshed plaster is given. In figures 4.4 to 4.6 both plasters have a barrier thickness of 50 µm (like the actual plasters) and in figures 4.7 to 4.9 the barrier thickness is 500 µm.

From the side view in figure 4.4 and the top view just above the dielectric layer in figure 4.5, a clear local field enhancement can be observed for the meshed plaster with a 50 µm barrier. This is a result of the mesh structure with sharp edges and the thin barrier. The field is highest at points between intersections of the mesh structure. At these places the field is enhanced by approximately 20% compared to field resulting from the plane plaster. At places where there is a 'void' in the mesh structure, the field about 20% lower than in the case of the plane plaster.

When the barrier thickness is increased, the effects of the meshed structure become less pronounced in the air gap. Starting from a barrier thickness of approximately 500 µm, the plane plaster and meshed plaster produce similar fields in the gap, as shown in figures 4.7 and 4.8. Thus, the barrier thickness of the meshed plaster controls the amount of field enhancement in the air gap and can therefore be used as a design rule for the meshed plaster. The 50 µm layer was chosen specifically to study the effects of field enhancement and, as will be shown in the following chapters, it has a dramatic effect on how the discharge is distributed in the volume between the plaster and secondary electrode.

Finally, just below the secondary electrode another local enhancement of electric field strength is observed in figures 4.6 and 4.9. This is caused by the round edges of the secondary electrode and may potentially result in the discharge concentrating here. In principle, these enhancements can be prevented by using appropriate edge shapes known as Rogowski profiles [42]. Rogowski profiles are commonly used to produce homogeneous electric fields between two plates and several methods to calculate them exist [43, 44].

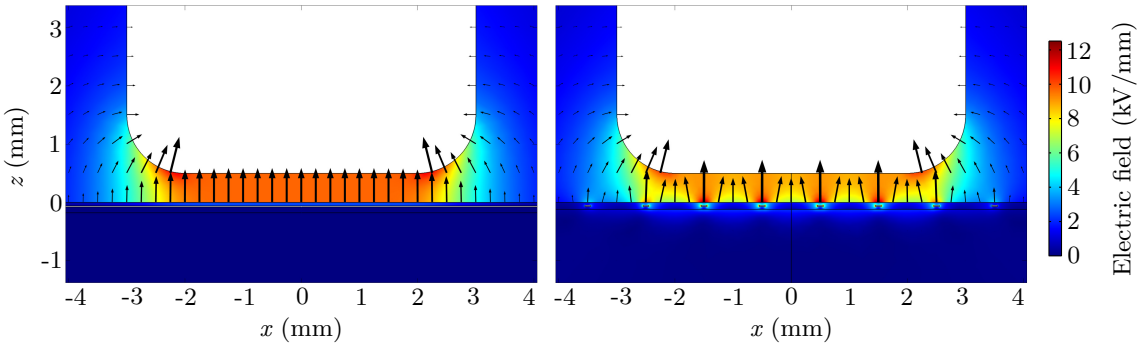

Figure 4.4: Side view ($y = 0$ plane) of the electric field strength for the plane plaster (left) and the meshed plaster (right), both with a barrier thickness of 50 µm. The arrows show the direction of the field at their tail and their lengths are proportional to the field strength.

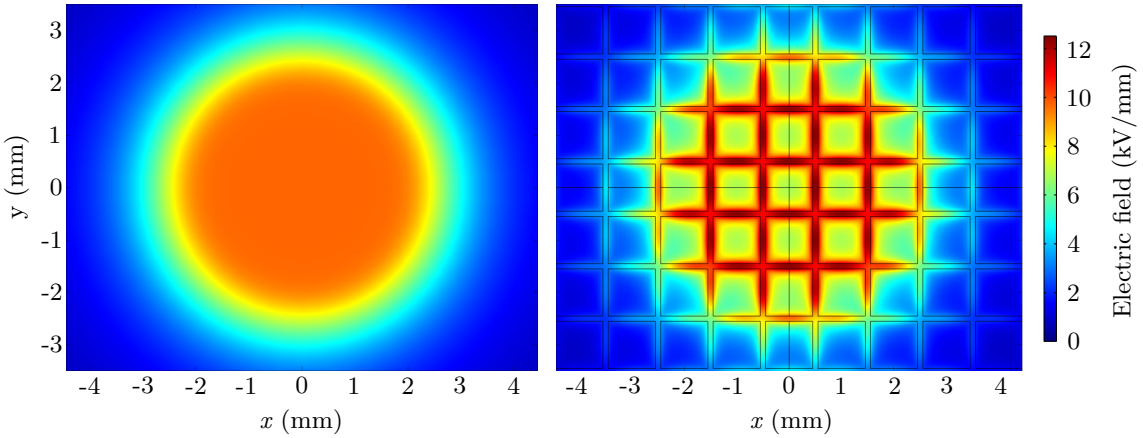

Figure 4.5: Top view ($z = 1\,\mu m$ plane) of the electric field strength just above the polyimide layer for the plane plaster (left) and the meshed plaster (right), both with a barrier thickness of 50 µm.

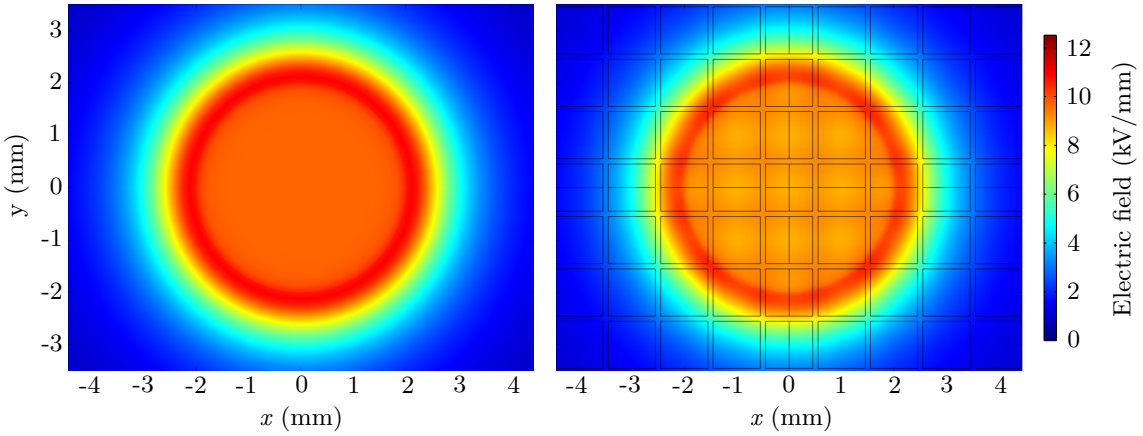

Figure 4.6: Top view ($z = 499\,\mu m$ plane) of the electric field strength just below the secondary electrode for the plane plaster (left) and the meshed plaster (right), both with a barrier thickness of 50 µm.

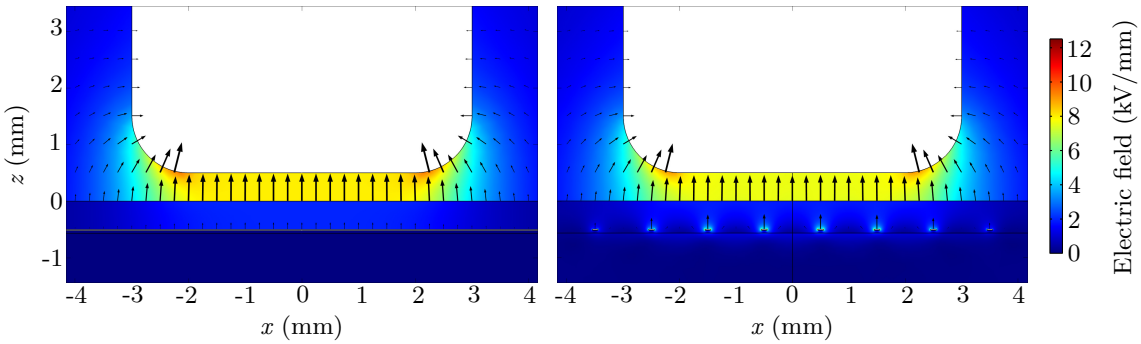

Figure 4.7: Side view ($y = 0$ plane) of the electric field strength for the plane plaster (left) and the meshed plaster (right), both with a barrier thickness of 500 µm. The arrows show the direction of the field at their tail and their lengths are proportional to the field strength.

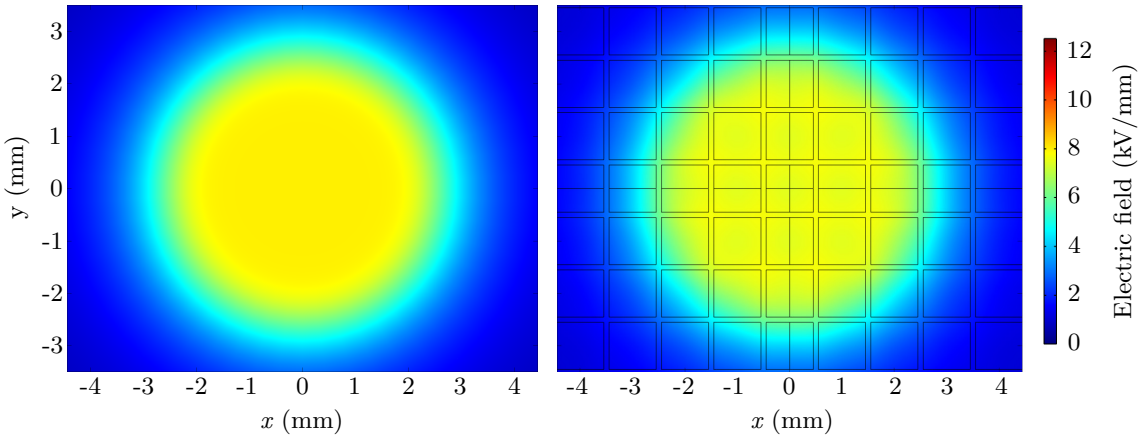

Figure 4.8: Top view ($z = 1\,\mu m$ plane) of the electric field strength just above the polyimide layer for the plane plaster (left) and the meshed plaster (right), both with a barrier thickness of 500 µm.

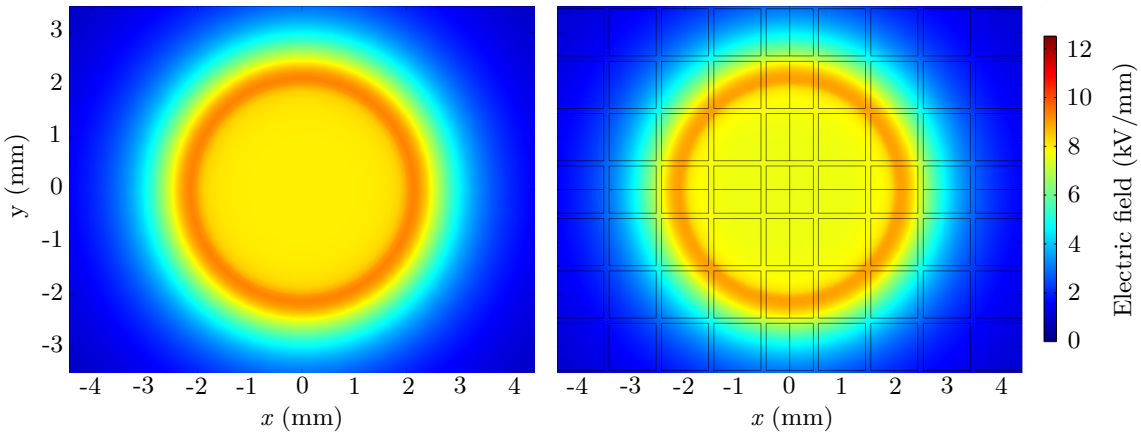

Figure 4.9: Top view ($z = 499\,\mu m$ plane) of the electric field strength just below the secondary electrode for the plane plaster (left) and the meshed plaster (right), both with a barrier thickness of 500 µm.

Chapter 5

Electronics and Electrical Characterisation

The plasma plasters are driven by a pulsed power system. Pulsed excitation is used to limit the delivered discharge current to short pulses. In section 5.1 the components of the system are discussed and the basic operation parameters are established. To compare the electrical properties of the plasters, voltage and current characteristics are used to determine the cell capacitance, barrier capacitance and energy dissipation in section 5.2. Finally, section 5.3 discusses the results and offers some general remarks on the operation of the plasters.

5.1 Electrical set-up and operation parameters

Positive unipolar high voltage (HV) pulses with a pulse width of 1 µs and a repetition frequency of 1 kHz are applied to the plaster to drive the discharge. A schematic overview of the electronics that are used to generate and deliver these pulses is shown in figure 5.1.

The pulsed power supply consists of three components: a HV direct current (DC) supply (Spellman UHR10P60), a function generator (Agilent 33220A) and a HV pulse generator (DEI PVX-4110). The HV pulse generator uses the signal from the function generator to gate the high voltage produced by the HV DC supply, resulting in a high voltage pulse.

The output of the pulsed power supply is connected to the plaster through a 1 kΩ series resistor. Mainly, this resistor is included as a precaution to prevent damage to the HV pulse generator from high conductive currents in case the dielectric barrier breaks.

A high voltage probe (Tektronix P6015) is placed between the series resistor and the plaster to measure the voltage across the discharge cell. Two Rogowski current probes are used to measure the current. One of the current probes (Pearson 6585) measures the current going into the plaster at the high voltage side and is labeled *HV side current*. The other current probe (Pearson 2877) measures the current leaving the secondary electrode at the grounded side and is referred to as *GND side current*.

All three probe signals are recorded by an oscilloscope (Agilent InfiniiVision DSO7034A, not included in figure 5.1). Transmission delays and the response times of the probes are taken into account by applying an appropriate offset to the different oscilloscope channels (see Appendix A.2.2).

Positive unipolar pulses with pulse heights of up to 10 kV can be generated with this set-up. The achieved rise times (10% to 90% of the pulse height) are several tens of nanoseconds and depend on the pulse height, as shown in figure 5.2.

To be able to apply an *overvoltage*, a voltage higher than the minimum required voltage to ignite the discharge, the gap width is set to 0.5 mm. For a gap width of 0.5 mm the breakdown voltage is found around 4.3 kV for both plasters. In addition, at 0.5 mm the gap remains large enough to visually observe the discharge. Figure 5.3 shows the discharge for both plasters as it appears to the eye with a pulse height of 5 kV.

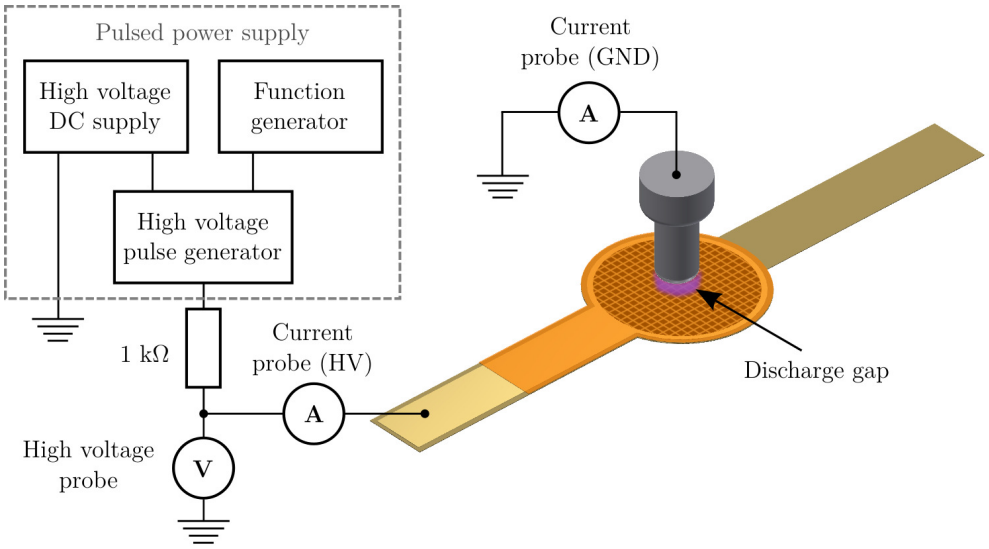

Figure 5.1: Schematic representation of the electrical set-up. The discharge gap, where discharges occur and plasma is generated, is indicated in purple.

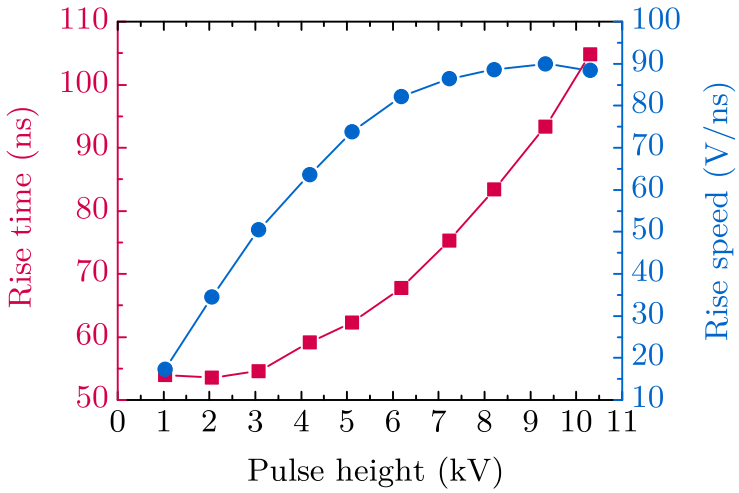

Figure 5.2: Rise time (red squares) and rise speed (blue circles) of the pulse as function of pulse height. The rise speed is calculated by dividing the pulse height by the rise time.

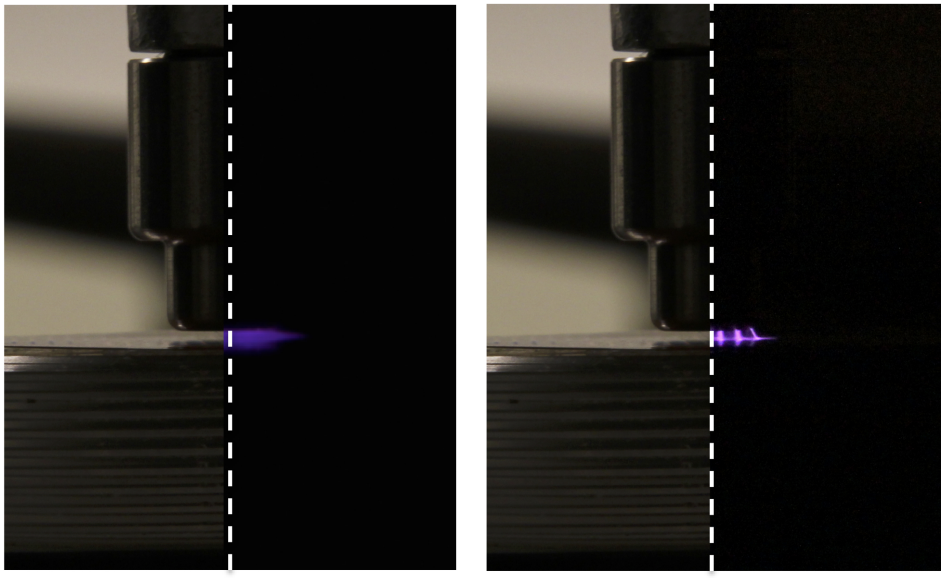

(a) Plane plaster **(b)** Meshed plaster

Figure 5.3: Visual appearance of the discharge for the plane plaster (a) and the meshed plaster (b). The left part of the images is taken with the light on to illustrate the viewing angle. The photographs of the discharges in the right parts of the images are taken using an exposure time of 1/6 s and 1 s for the plane plaster and meshed plaster respectively.

5.2 Voltage and current characteristics

The general shapes of the voltage and current signals for the two plaster share similar characteristics. The typical shape of the signals at pulse heights below the breakdown voltage ($< 4.3\,\mathrm{kV}$) are shown in figure 5.4. Both current signals in the bottom part of figure 5.4 show the displacement current caused by the change in voltage across the discharge cell. As will be explained in section 5.2.2, the difference in the two current signals is a result of stray capacitances.

Typical shapes of the voltage and current signals in the presence of a discharge are shown in figure 5.5. Besides the displacement current, there are now two additional discharge current peaks. The first one corresponds to the *discharge on the rise of the pulse*, which is driven by the electric field produced by the externally applied voltage. During the discharge on the rise of the pulse, negative charge is deposited on the dielectric barrier until the net electric field in the gap is zero. When the external voltage is turned off, only the electric field of the deposited charges remains and causes the *discharge on the fall of the pulse*. While the deposited charges are released from the dielectric surface the electric field driving the discharge on the fall of the pulse decreases. This results in a lower but broader discharge peak at the fall of the pulse. The current integrated over a whole cycle is zero and hence there is no net charge build-up on the dielectric barrier.

Although effort was taken to minimise ringing and interference in the voltage and current signals, significant oscillations are still observed on the discharge current on the rise of the pulse in the GND side current signal (bottom graph in figure 5.5). The oscillation is of the same order of magnitude as the discharge current peak and results in an overshoot, which explains the increased peak height compared to the HV side current signal.

Furthermore, the discharge current peak on the rise of the pulse exhibits a jitter of about 20 ns from pulse to pulse, while the jitter on the discharge current peak on the fall of the pulse is only about 5 ns. On the fall of the pulse there are electrons present on the dielectric barrier that were deposited during the discharge on the rise of the pulse. These electrons are used to initiate breakdown on the fall of the pulse. At the rise of the pulse, there are no electrons left from the previous discharge and a new first electron is required. The exact time and location of the production of this electron are subject to chance, which explains the larger jitter on the discharge current peak on the rise of the pulse.

To compare the electrical properties of the plasters, the capacitance of the discharge cell C_{cell}, the capacitance of the barrier C_{barrier} and the energy dissipation per cycle E_{cycle} are determined. These quantities can all be calculated from the voltage and current signals. To understand how they relate to measured signals, the electrical system is first analysed using an equivalent circuit.

5.2.1 Equivalent circuit

An equivalent circuit to the electrical set-up is given in figure 5.6. The part that represents the discharge cell is indicated by the dashed grey rectangle. The capacitors C_{barrier} and C_{gap} represent the dielectric barrier and the air gap respectively.

A variable resistor R is placed parallel to C_{gap} to model the resistance of the plasma during the discharge [19]. When the voltage across the air gap is insufficient to ignite a discharge, the resistance is taken infinitely large and the discharge current I_R is in this case zero. In literature sometimes an additional switch in series with the variable resistor is used to model this behaviour [17]. Alternatives to the variable resistor include two facing Zener diodes [16], or a voltage controlled current source [45]. However, in the analysis of the equivalent circuit this choice is irrelevant here, as they all lead to the same results.

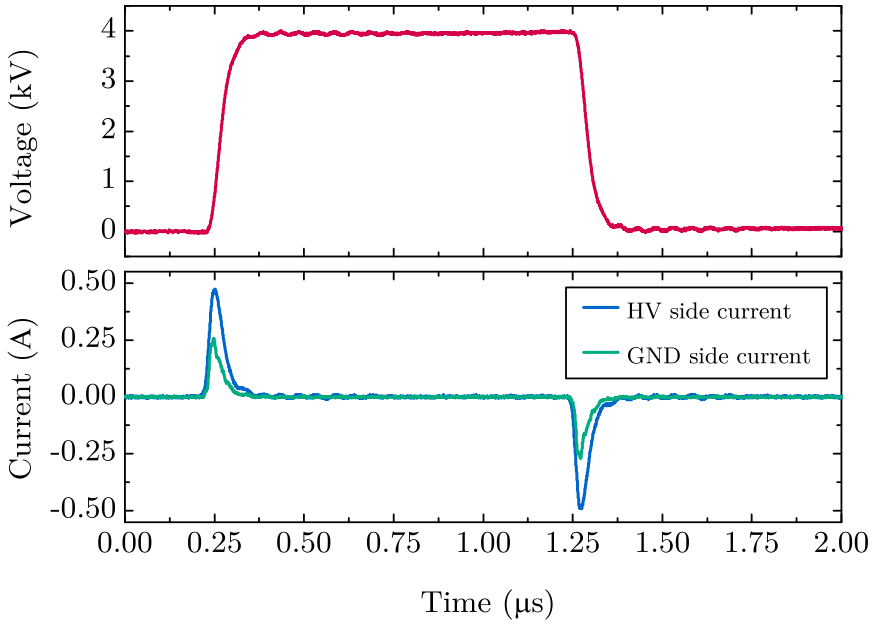

Figure 5.4: Typical signals without a discharge. Only displacement current is present in the current graph.

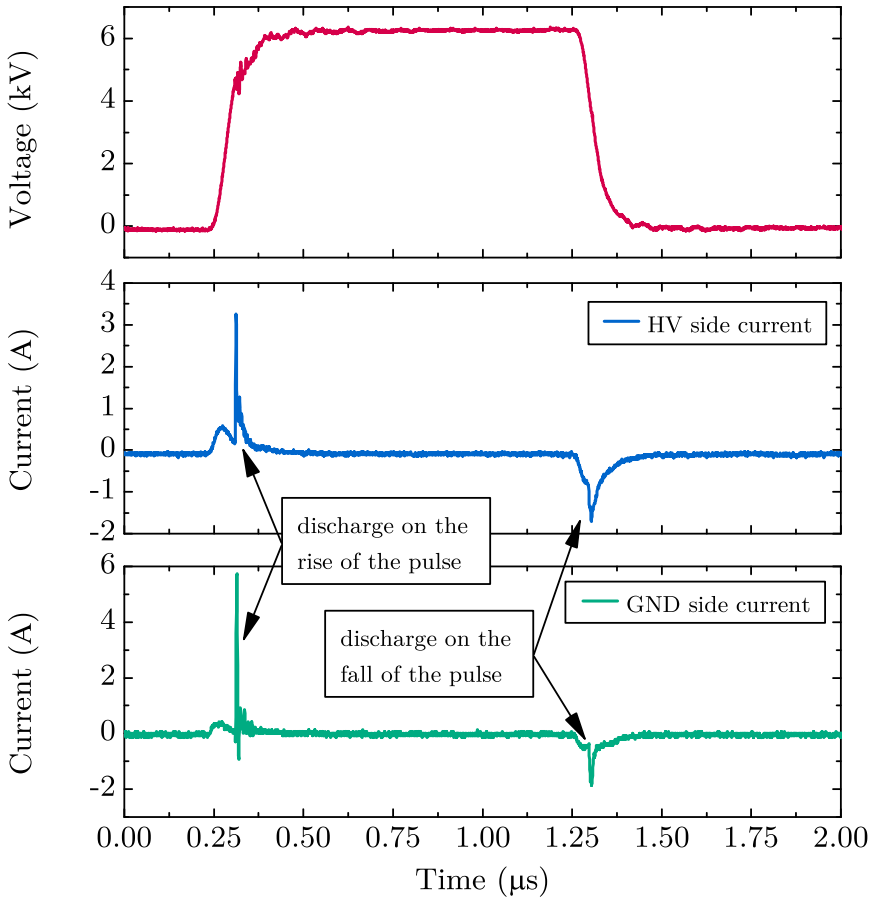

Figure 5.5: Typical signals with a discharge. In addition to the displacement current two discharge current peaks are now visible. One occurs on the rise of the pulse and the other on the fall of the pulse.

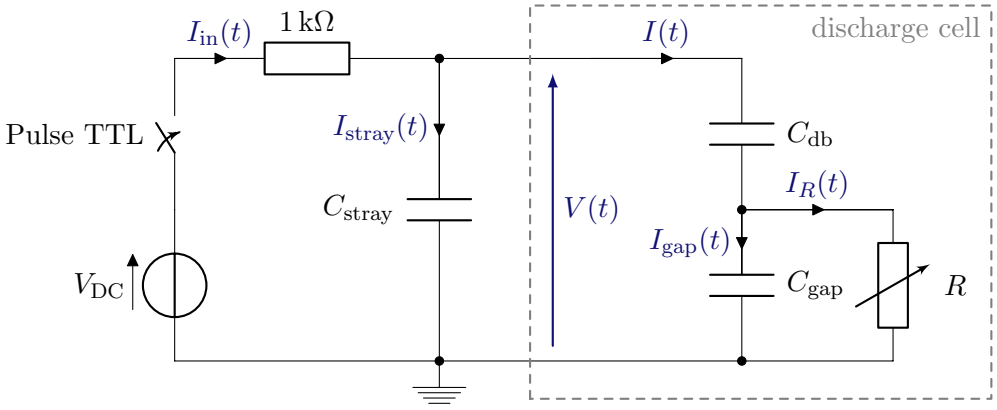

Figure 5.6: Equivalent circuit to the electrical set-up of figure 5.1.

In general, any electrical component is capacitively coupled to some extent to other components in its proximity. This results in unintended stray capacitances. Stray capacitances are distributed along the system and cannot be represented by a single localised capacitor. Nevertheless, a capacitor C_{stray} is placed parallel to the discharge cell to indicate the presence of stray capacitances.

As shown in figure 5.1, the voltage and current are measured after the 1 kΩ series resistor. It is therefore not necessary to include the pulsed power supply and the series resistor in the equivalent circuit. However, for completeness the pulsed power supply is modeled by a DC voltage source and a switch, whose state is determined by a pulsed transistor-transistor logic (TTL) signal.

Without a discharge in the air gap, the circuit is completely capacitive and there is only displacement current. In this case the voltage over the discharge cell $V(t)$ and the current flowing into the discharge cell $I(t)$ are related by

$$I(t) = C_{\text{cell}} \frac{\mathrm{d}V}{\mathrm{d}t} \tag{5.1}$$

with

$$C_{\text{cell}} = \frac{C_{\text{barrier}} C_{\text{gap}}}{C_{\text{barrier}} + C_{\text{gap}}}. \tag{5.2}$$

So, in the absence of a discharge, the capacitance of the discharge cell can be calculated from the signal measured by either of the current probes and the derivative of the signal measured by the voltage probe.

The instantaneous power $P(t)$ that is dissipated in the gap is

$$P(t) = V_{\text{gap}}(t) I_R(t). \tag{5.3}$$

While the voltage across the gap $V_{\text{gap}}(t)$ and the discharge current $I_R(t)$ cannot be measured directly, it can be shown that the amount of energy that is dissipated in the gap during one cycle is given by

$$E_{\text{cycle}} = \int_0^T P(t)\,\mathrm{d}t = \int_0^T V_{\text{gap}}(t) I_R(t)\,\mathrm{d}t \tag{5.4}$$

$$= \int_0^T V(t) I(t)\,\mathrm{d}t, \tag{5.5}$$

where T is the duration of one cycle. This provides a method to calculate the energy dissipation per cycle from the voltage and current measured by the probes. A detailed derivation of equation 5.5 can be found in [46] and is also provided in Appendix A.1.

Table 5.1: The capacitance of the discharge cell determined by different methods.

Method	Capacitance (pF)	
	Meshed plaster	Plane plaster
Eq. 5.1 (HV side)	6.1 ± 0.6	6.2 ± 0.6
Eq. 5.1 (GND side)	2.8 ± 0.8	2.8 ± 0.7
Lissajous method	3.2 ± 0.3	3.4 ± 0.3
Comsol[1]	0.9	1.1

[1] In the Comsol model only the circular centre part of the plasters is taken into account.

5.2.2 Cell capacitance

To calculate C_{cell} from equation 5.1, the voltage signal is first numerically differentiated. Since numerical differentiation is sensitive to noise, the signals from 1024 cycles are averaged on the oscilloscope to improve the signal-to-noise ratio. Voltage and current signals measured at a pulse height of 4 kV are used to calculate C_{cell}.

Table 5.1 shows the found values for both plasters using the HV side current in the first row and using the GND side current in the second row. For both plasters the same values are found within the error margin. There is however a factor of approximately 2 difference between the measurements using the HV side current and the GND side current. This is a result of stray capacitance: A larger amount of stray capacitance is included in the measurement at the HV side than in the measurement at the GND side. The third row in table 5.1 shows the values found using the *Lissajous method* and will be discussed in section 5.2.3.

Finally, the Comsol model that was used for the electrostatic field simulations in Chapter 4 can also be used to calculate the cell capacitance without the influence of any stray capacitance. The results are shown in the bottom row of table 5.1. The model predicts that the meshed plaster results in an approximately 0.2 pF lower cell capacitance than the plane plaster.

Comparing the found values from the different methods, it is observed that stray capacitances constitute the largest part of the total capacitance of the system. The 0.2 pF difference between the meshed plaster and the plane plaster is negligible compared to the stray capacitance and therefore the voltage and current behaviour of both plasters is similar when there is no discharge.

5.2.3 Barrier capacitance

Another commonly used approach to the electrical analysis of DBDs is the so-called *Lissajous method*, which was first proposed by Manley in 1943 [47]. In this method the cell capacitance C_{cell} as well as the barrier capacitance C_{barrier} can be determined from a parametric plot of the charge $Q(t)$ on dielectric barrier against the applied voltage $V(t)$, provided that the maximum voltage is sufficiently high to cause breakdown. Such a parametric plot is called a Lissajous figure.

For sinusoidal excitation, the Lissajous figure is a parallelogram. As illustrated in figure 5.7, one slope of the parallelogram is equal to C_{cell} and the other slope is equal to C_{barrier} [16, 17, 47]. However, this does assume that the voltage across the gap remains constant and equal to the breakdown voltage during the discharge. In fast pulsed discharges this

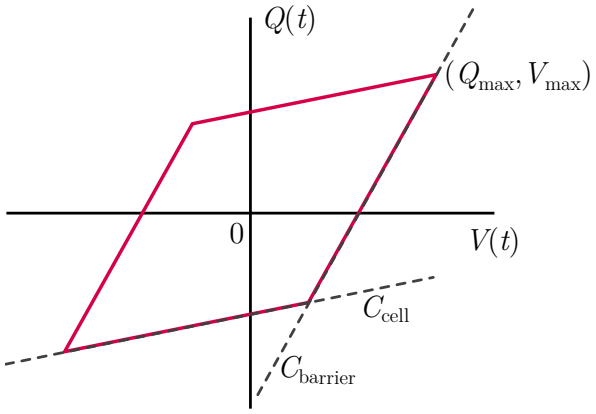

Figure 5.7: Typical Lissajous figure for sinusoidal excitation.

is often not the case, as evidenced by the rise times and rise speeds shown in figure 5.2. As a result, the Lissajous figures do not appear as well-defined parallelograms for pulsed excitation.

Nevertheless, recent literature has shown that Lissajous figures can still be useful for electrical characterisation under pulsed excitation [48]. In the case of pulsed excitation, the maximum amount of charge $Q_{\max}$ that is accumulated on the barrier after the discharge on the rise of the pulse is still related to the maximum applied voltage $V_{\max}$ (the pulse height) by:

$$Q_{\max} \propto C_{\text{barrier}} V_{\max}. \tag{5.6}$$

So C_{barrier} can now be determined from the $(Q_{\max}, V_{\max})$ points of multiple Lissajous figures measured at different pulse heights.

The charge $Q(t)$ is determined by measuring the voltage $V_m(t)$ across an additional capacitor of known capacitance C_{m}, which is placed between the discharge cell and the ground:

$$Q(t) = C_m V_m(t). \tag{5.7}$$

By choosing $C_m = 500\,\text{pF} \gg C_{\text{cell}}$, the influence of the additional capacitor on the system is minimised and $V_m(t)$ is of the order of several 10 V.

The measured Lissajous figures using the meshed plaster are shown in figure 5.8. Due to heavy oscillations in the $Q(t)$ signal, adjacent averaging with a window of 101 points, which is equivalent to 50 ns, was applied to obtain the shown Lissajous figures. Since the system resides in the $(Q_{\max}, V_{\max})$ state for about 1 µs between the discharges on the rise of the pulse and on the fall of the pulse, no essential information is lost by the smoothing process.

A linear fit through the $(Q_{\max}, V_{\max})$ points results in a barrier capacitance of 19 ± 3 pF. Repeating the measurements using the plane plaster results in the same value. To compare, the formula for an ideal parallel plate capacitor $C = \varepsilon_0 \varepsilon_r A/d$ with an effective electrode area of $A = \pi r^2 = \pi(3.0\,\text{mm})^2 = 2.8 \times 10^{-5}\,\text{m}^2$, a separation of $d = 50\,\mu\text{m}$ (the barrier thickness) and $\varepsilon_r = 4$ gives 20 pF.

Additionally, the bottom slope of the Lissajous figures is still equal to C_{cell} as indicated in figure 5.8. The cell capacitance obtained from this method was already included in table 5.1. Since $Q(t)$ is essentially equal to the integrated GND side current, the resulting value of C_{cell} is similar to that found from equation 5.1 using the GND side current.

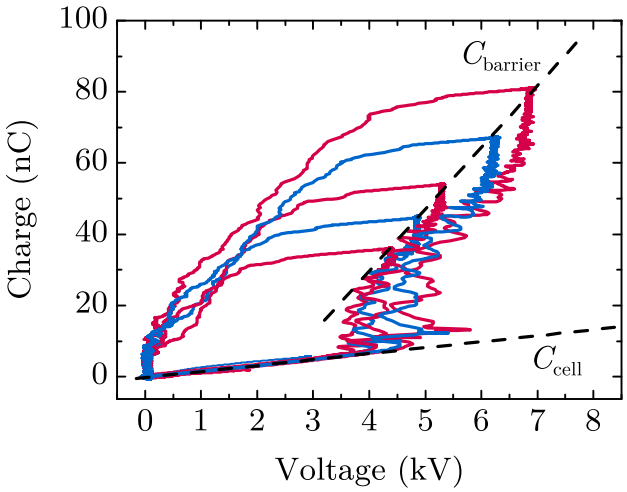

Figure 5.8: Lissajous figures for different pulse heights measured using the meshed plaster. C_{barrier} is determined by fitting a line through the $(Q_{\max}, V_{\max})$ points and C_{cell} is calculated from the bottom slope of the figures.

5.2.4 Energy dissipation

For both plasters the averaged energy dissipation per cycle $\bar{E}_{\text{cycle}}$ is determined as function of pulse height. The averaged energy per cycle is calculated using $N = 10$ single cycle measurement:

$$\bar{E}_{\text{cycle}} = \frac{1}{N} \sum_{i=1}^{N} E_{\text{cycle}(i)}. \tag{5.8}$$

As demonstrated by equation 5.5, $E_{\text{cycle}(i)}$ can be obtained by numerically integrating the product of the voltage signal and the current signal. The results using the HV side current are shown in figure 5.9. A detailed analysis of the errors is given in Appendix A.2. Using the GND side current leads to the same values within the error margin.

Three different regions can be distinguished in figure 5.9:

Region I. For pulse height below approximately 4.3 kV the voltage is too low to ignite a discharge and as a result and there is virtually no energy dissipation;

Region II. For pulse heights between about 4.3 kV and 7 kV the averaged energy dissipation per cycle increases approximately linearly with pulse height.

Region III. For pulse heights exceeding 7 kV the averaged energy dissipation per cycle keeps increasing approximately linearly for the plane plaster. However, for the meshed plaster a significant increase in energy dissipation is observed.

Inspecting the meshed plaster at pulse heights greater than 7 kV reveals that the discharge now extends beyond the area that is directly underneath the secondary electrode. The photographs in figure 5.10 show that the discharge branches outwards along the surface of the dielectric and follows the structure of the mesh. Figure 5.11 shows the current signal for a pulse height of 8.5 kV using the meshed plaster. Comparing figure 5.11 to the middle graph of figure 5.5, additional discharge current is observed after the primary discharge current peak. This suggests that the outwards branching of the discharge occurs after the primary discharge in the gap.

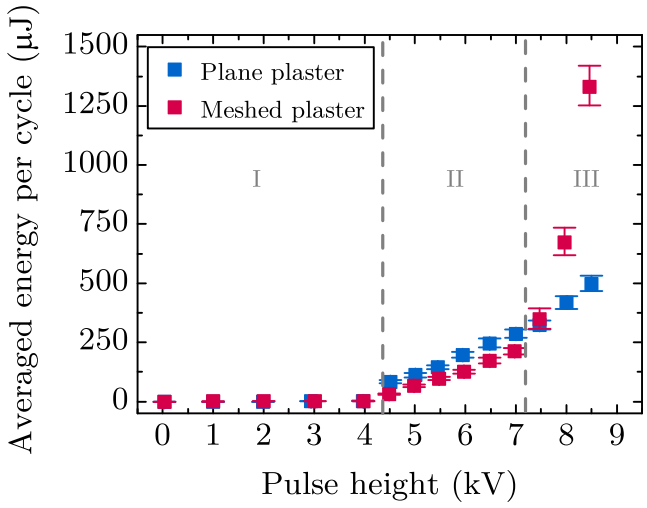

Figure 5.9: Average energy per cycle as function of pulse height at constant pulse width of 1 µs and a repetition frequency of 1 kHz. Three different regions are indicated by roman numerals.

5.3 Discussion

The effect of the electrode structure on the discharge is immediately visible in 5.3. The discharge with the plane plaster in figure 5.3a looks diffuse, whereas a clear structure is visible for the meshed plaster in figure. Nevertheless, since these photographs are taken using exposure times covering hundreds of discharges, they cannot be used to determine whether the discharge is diffuse and covers the whole gap region during a single pulse.

For both plasters the discharge current peaks appear as a single peak. This is often an indication of a diffuse discharge. However, if microdischarges temporally overlap, the current probe might not be able to resolve individual current peaks. In addition, in literature examples have been reported where patterned DBDs, consisting of regularly organised filaments, have current characteristics similar to those of a diffuse DBD [**?**]. So further investigation is still required to verify the discharge modes of both plasters.

In the range of pulse heights of approximately 4.3 kV to 7 kV the energy dissipation per cycle gradually increases for both plasters. This is expected because at higher voltages higher electric fields are produced and more charge is transported before the discharge is choked. The averaged energy dissipation per cycle for the plane plaster is about 30% higher than for the meshed plaster. However, since the discharge distribution resulting from the two plasters is not the same, this does not necessarily mean that the energy density in the discharge is higher for the plane plaster.

For the meshed plaster increased energy dissipation is found for voltage larger than 7 kV, which is related to the discharge extending beyond the discharge gap. As mentioned, the current signal suggests that the outwards branching occurs after the primary discharge in the gap. It is believed that this is a result of charge repulsion and strong electric fields along the dielectric surface just outside the gap, both caused by the negative charge that is deposited on the dielectric during the primary discharge. Time resolved imaging of the discharge using an intensified charge coupled device (ICCD) camera may be used to confirm that the outwards branching occurs after the primary discharge. However, since the plasters only last for less than a minute in this mode and the amount of plasters is limited, this behaviour is not further investigated.

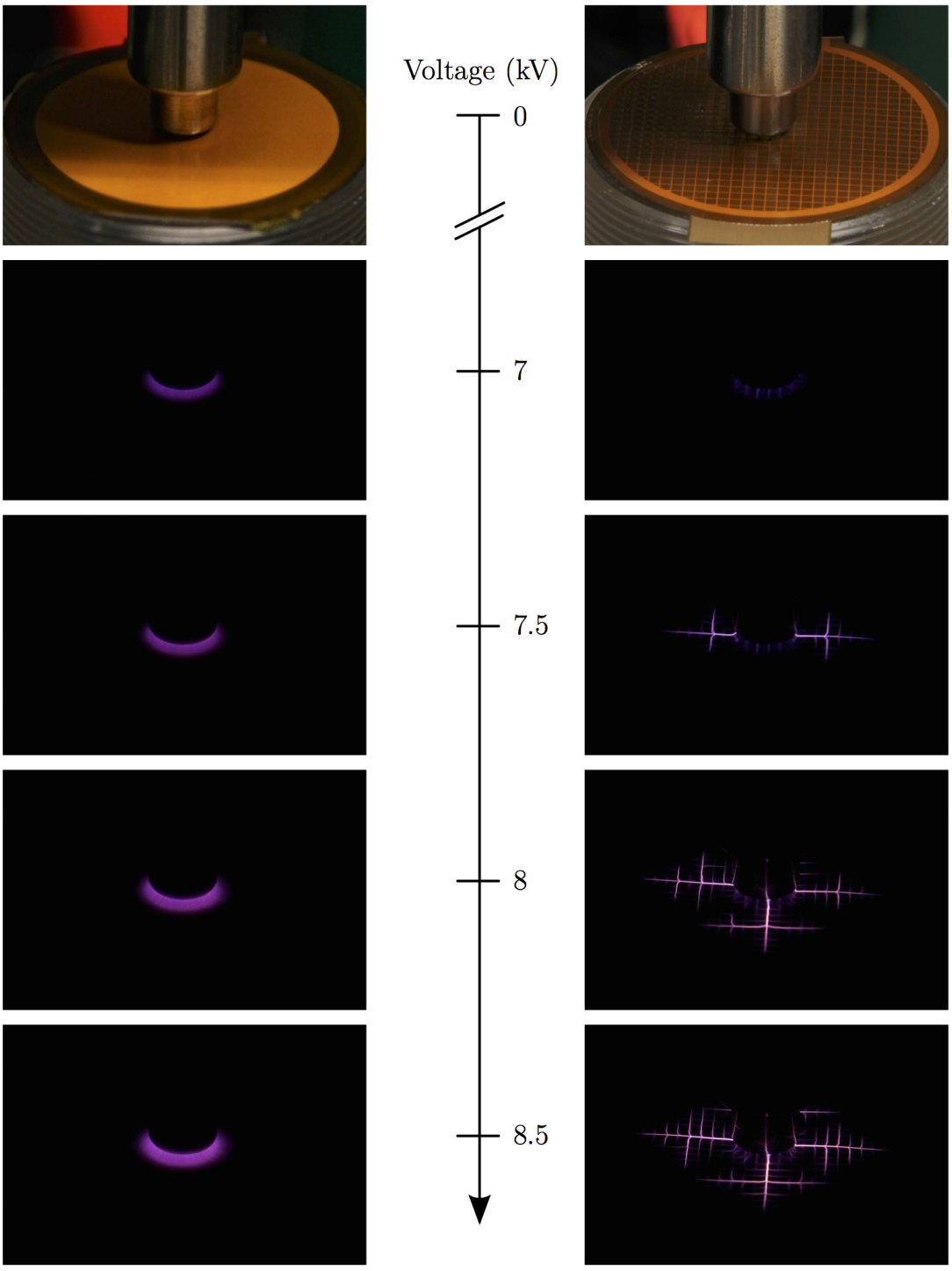

Figure 5.10: Photographs of the discharge using pulse heights of $\leqslant 7\,\mathrm{kV}$. The photographs on the top are taken with the lights on and illustrate the viewing angle. The camera was used in burst mode while the voltage was increased manually, so the voltage values are merely indicative.

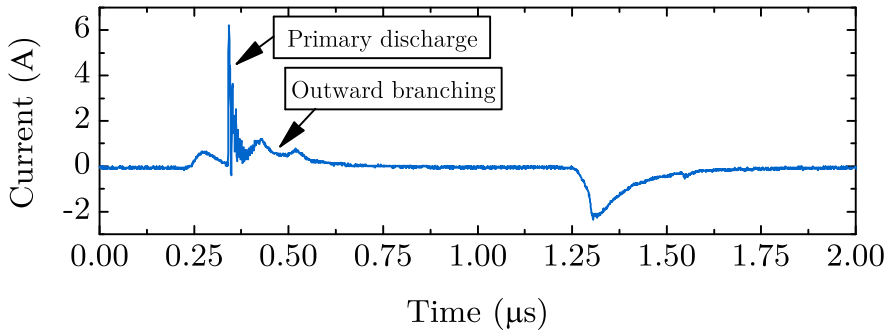

Figure 5.11: Current measured at the HV side for the meshed plaster operated at 8.5 kV. Additional discharge current corresponding to the branching is visible after the primary discharge on the rise of the pulse.

While using pulse heights between 4.3 to 7 kV (region II of figure 5.9), the plasters can operate up to an hour before breakdown of the barrier finally occurs. As mentioned in Chapter 4, the dielectric strength of polyimide is sufficiently high to prevent dielectric breakdown due the applied electric fields. However, exposure to plasma causes degradation. The degradation of the polyimide barrier is visible by eye: the part of the barrier that is exposed to plasma becomes less reflective. In literature it has been reported that exposure of polyimide to an air plasma indeed results in an increased surface roughness and oxidation [49].

Some of the plasters stop operating before breakdown of the barrier occurs. In this case, the discharge current peak on the rise of the pulse first starts to drift towards the end of the pulse and the jitter significantly increases, up to hundreds of nanoseconds. This unstable behaviour can commence at any time during operation and ultimately extinguishes the discharge. By increasing the voltage, a discharge can still be ignited for a short time before it extinguishes again. This may indicate the build-up of negative charge on the barrier surface. Additionally, it might be related to a build-up of space charge in the polyimide material, as reported in [50]

Despite their limited and unpredictable operation time, the plasters do produce reproducible results while operating in the stable mode with low amounts of jitter as described in section 5.2. All results presented in this thesis are obtained while the plaster is operating in the stable mode.

Chapter 6

Discharge Mode and Distribution

In this chapter the discharge mode and the discharge distribution of both plasters are investigated. Fast imaging with an intensified charge coupled device (ICCD) camera is used to record emission from a single discharge. Images with exposure times of $5\,\mathrm{ns}$ are used to study the discharge mode and images with exposure times of $100\,\mathrm{ns}$, which capture an entire single discharge, are used to reconstruct the emission pattern within the gap. First, section 6.1 provides background on the two tomographic techniques that are used to obtain the discharge distribution in the gap: Abel inversion and the inverse Radon transform. Section 6.2 explains the experimental set-up that is used to record and analyse the images. Finally, the results are presented and discussed in section 6.3 and section 6.4 respectively.

6.1 Plasma tomography

To gain insight in the discharge distribution, the local emission of light within the gap is studied. The local emission at position $\mathbf{r}$ in the plasma is characterised by the *emission coefficient* $\epsilon(\mathbf{r})$. However, when a detector is used to measure the light emitted by a plasma in a specific direction, photons emitted in that direction from different places in the plasma contribute to the recorded intensity: what is measured is a line integral of $\epsilon(\mathbf{r})$. The measured intensity can be written as

$$I = \int_L \epsilon(\mathbf{r})\,\mathrm{d}l, \tag{6.1}$$

where l is the length parameter along of the *line-of-sight* L. This concept is illustrated in figure 6.1, where an observer looks to a plasma, which is indicated in purple and has a certain local emission coefficient $\epsilon(\mathbf{r})$. The observed intensity is the result of photons that are emitted in the shaded area in the direction of the observer.

Local information can be reconstructed from multiple line-of-sights measurements. If the plasma has cylindrical symmetry, a technique called *Abel inversion* can be applied to a lateral set of line-of-sight integrated intensity measurements to obtain the radial distribution of emission. If there is no symmetry, a more general approach has to be used. The local emission coefficient is in this case obtained by applying the *inverse Radon transform* to intensity measurements taken from numerous different angles.

Both techniques are now further explained. More details can be found in the book on computerised tomography by Kak and Slaney [51].

6.1.1 Abel inversion

In case of a plasma with an outer radius R and cylindrical symmetry, the emission coefficient only depends on the radial coordinate, $\epsilon = \epsilon(r)$. A Cartesian coordinate system is chosen such that the detector is parallel to the y-axis, as illustrated in figure 6.2.

The intensity $I = I(y)$ measured by the detector in a lateral scan is obtained by integrating $\epsilon(r)$ along chords parallel to the x-axis:

$$I(y) = \int_{-\infty}^{+\infty} \epsilon(r)\,\mathrm{d}x = \int_{-\sqrt{R^2-y^2}}^{\sqrt{R^2-y^2}} \epsilon(r)\,\mathrm{d}x = 2\int_0^{\sqrt{R^2-y^2}} \epsilon(r)\,\mathrm{d}x, \tag{6.2}$$

where $x = \pm\sqrt{r^2-y^2}$ was used. Switching the integration variable from x to r leads to

$$I(y) = 2\int_y^R \frac{\epsilon(r) r\,\mathrm{d}r}{\sqrt{r^2-y^2}}. \tag{6.3}$$

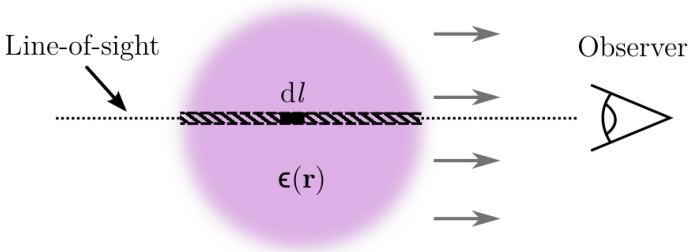

Figure 6.1: Illustration of the line-of-sight. All photons emitted in the direction of the observer within the shaded area contribute to the observed intensity.

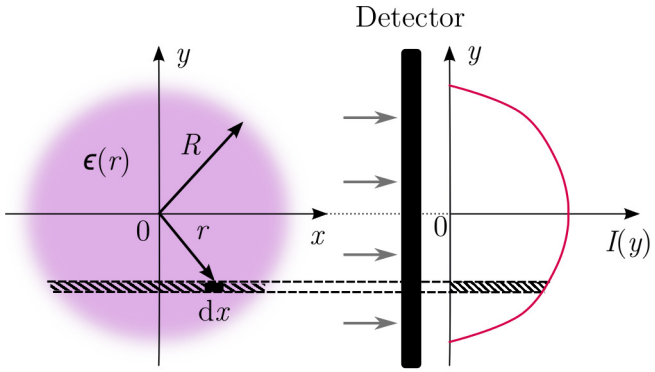

Figure 6.2: Coordinate system for Abel inversion. The detector is parallel to the y-axis and and makes a lateral scan along chords parallel to the x-axis. The resulting intensity profile $I(y)$ is shown by the red curve.

This equation can be inverted analytically to

$$\epsilon(r) = -\frac{1}{\pi}\int_r^R \frac{\mathrm{d}I(y)}{\mathrm{d}y}\frac{\mathrm{d}y}{\sqrt{y^2-r^2}}, \tag{6.4}$$

which is known as Abel inversion.

Since the derivative of $I(y)$ is present in equation 6.3, the results are highly sensitive to noise. Therefore, the quality of the inversion is highly dependent on the signal-to-noise ratio of the measurement and a significant amount of smoothing may be required. Algorithms that do not use differentiation exist as well. One example is the Fourier-based method proposed by Pretzler [52], which will be used here.

The Fourier-based method first expands the unknown distribution $\epsilon(r)$ into a series of cosine functions up to order N

$$\epsilon(r) = \sum_{n=0}^{N} A_n f_n(r), \tag{6.5}$$

where A_n are the expansion coefficients and

$$f_n(r) = \begin{cases} 1 & \text{if } n = 0 \\ 1-(-1)^n \cos\left(n\pi\frac{r}{R}\right) & \text{if } n \geqslant 1 \end{cases}. \tag{6.6}$$

Next, the line-of-sight intensity profile resulting from the expansion is calculated using equation 6.2. The expansion coefficients are then fitted to match the measured intensity profile using the linear least squares method. Finally, the fitted expansion coefficients are reinserted in equation 6.4, producing $\epsilon(r)$. Besides the advantage of not having to calculate any derivative, this method also implicitly functions as a low-pass filter by limiting the frequencies that appear in the expansion through N.

6.1.2 Radon transform and inverse Radon transform

When there is no symmetry at all, a more general approach to obtain the local emission coefficient has to be used: the inverse Radon transform. In this method the intensity measurements from different angles are used to reconstruct $\epsilon(\mathbf{r})$. To understand how this works, first the intensity profile resulting from a single lateral scan is analysed.

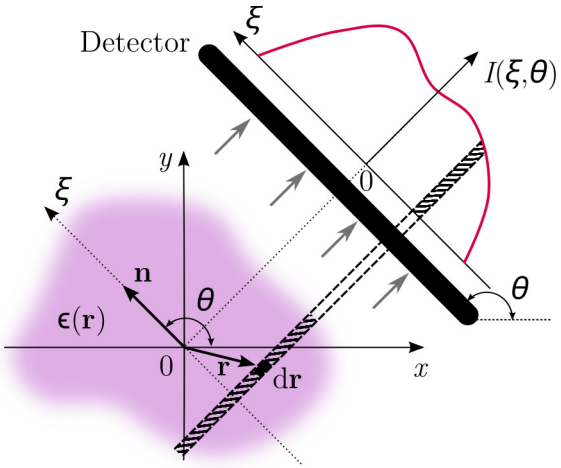

Figure 6.3: Coordinate system for the two-dimensional Radon transform. The position of the detector is defined by the angle θ with the x-axis. The axis along the detector is the ξ-axis. The resulting intensity profile $I(\xi, \theta)$ from a lateral scan is shown by the red curve.

Figure 6.3 shows an arbitrarily shaped plasma, which is again indicated in purple and has an emission coefficient $\epsilon(\mathbf{r})$. The detector makes an angle θ with the x-axis and the axis along the detector is named the ξ-axis. The unit vector along the ξ-axis is $\hat{\mathbf{n}} = (\cos\theta, \sin\theta)$.

In a lateral scan the emission coefficient is now integrated along straight lines that satisfy

$$\hat{\mathbf{n}} \cdot \mathbf{r} = x\cos\theta + y\sin\theta = \xi. \tag{6.7}$$

The intensity $I(\xi, \theta)$ for a fixed angle θ is then given by

$$I(\xi, \theta) = \iint \epsilon(x, y)\delta(x\cos\theta + y\sin\theta - \xi)\,\mathrm{d}x\,\mathrm{d}y \tag{6.8}$$

$$= \mathcal{R}_2[\epsilon(x, y)], \tag{6.9}$$

where δ is the Dirac delta function. The mathematical relation between $I(\xi, \theta)$ and $\epsilon(x, y)$ in equation 6.9 is the two-dimensional Radon transform $\mathcal{R}_2$.

Now the objective is to retrieve $\epsilon(x, y)$ by applying an inverse Radon transform $\mathcal{R}_2^{-1}$ to $I(\xi, \theta)$:

$$\epsilon(x, y) = \mathcal{R}_2^{-1}[I(\xi, \theta)]. \tag{6.10}$$

There are several techniques to obtain the inverse Radon transform. The most widely used method is the *filtered back projection* [51]. This method is based on the *Fourier slice theorem*, which establishes a relation between the one-dimensional (1D) Fourier transform of a lateral scan $I(\xi, \theta) = \mathcal{R}_2[\epsilon(x, y)]$, and the two-dimensional (2D) Fourier transform of the emission coefficient $\epsilon(x, y)$.

First, the intensity $I(\xi, \theta)$ at fixed angle θ is 1D Fourier transformed with respect to ξ:

$$\hat{I}(k_\xi, \theta) = \mathcal{F}_1[I(\xi, \theta)] = \int I(\xi, \theta)e^{-ik_\xi \xi}\,\mathrm{d}\xi. \tag{6.11}$$

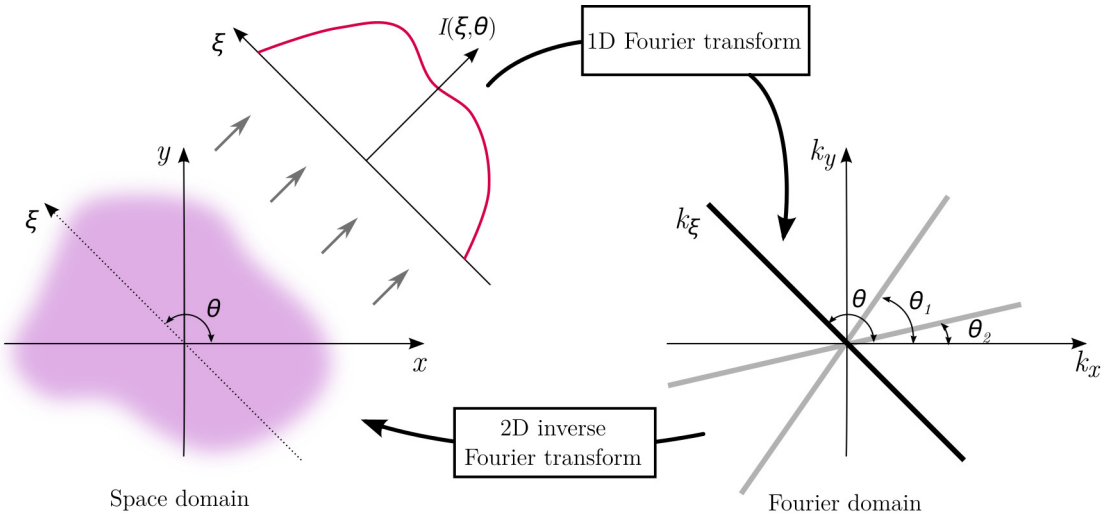

Figure 6.4: Illustration of the inverse Radon transform. The 1D Fourier transform of a lateral scan at angle θ in the space domain is equal to a slice of the 2D Fourier spectrum at the same angle θ in the Fourier domain. Acquiring lateral scans at different angles θ_1 and θ_2, results in slices at angles θ_1 and θ_2.

Substituting $I(\xi, \theta)$ from equation 6.8 into equation 6.11 gives

$$\hat{I}(k_\xi, \theta) = \iiint \epsilon(x, y)\delta(x\cos\theta + y\sin\theta - \xi)e^{-ik_\xi \xi}\,\mathrm{d}x\,\mathrm{d}y\,\mathrm{d}\xi \tag{6.12}$$

$$= \iint \epsilon(x, y)e^{-ik_\xi(x\cos\theta + y\sin\theta)}\,\mathrm{d}x\,\mathrm{d}y, \tag{6.13}$$

where the sifting property of the Dirac delta function was invoked in equation 6.13.

Next, the 2D Fourier transform of $\epsilon(x, y)$ is defined as

$$\hat{\epsilon}(k_x, k_y) = \mathcal{F}_2[\epsilon(x, y)] = \iint \epsilon(x, y)e^{-i(k_x x + k_y y)}\,\mathrm{d}x\,\mathrm{d}y. \tag{6.14}$$

Comparing equation 6.13 and equation 6.14 shows that $\hat{I}(k_\xi, \theta)$ is equal to $\hat{\epsilon}(k_x, k_y)$ evaluated at $k_x = k_\xi \cos\theta$ and $k_y = k_\xi \sin\theta$:

$$\hat{I}(k_\xi, \theta) = \hat{\epsilon}(k_\xi \cos\theta, k_\xi \sin\theta). \tag{6.15}$$

This result is known as the Fourier slice theorem. It means that the 1D Fourier transform of a lateral scan of $\epsilon(x, y)$ at an angle θ with the x-axis, is equal to a 'slice' of the 2D Fourier spectrum of $\epsilon(x, y)$ at an angle θ with the k_x-axis.

So, by measuring $I(\xi, \theta)$ at different angles θ and subsequently applying a 1D Fourier transform, the 2D Fourier spectrum of $\epsilon(x, y)$ can be constructed. The emission coefficient is then obtained by using the inverse 2D Fourier transform:

$$\epsilon(x, y) = \mathcal{F}_2^{-1}[\hat{\epsilon}(k_x, k_y)] = \frac{1}{4\pi^2}\iint \hat{\epsilon}(k_x, k_y)e^{i(k_x x + k_y y)}\,\mathrm{d}k_x\,\mathrm{d}k_y. \tag{6.16}$$

This concept is illustrated in figure 6.4, where both the space domain and the Fourier domain are shown.

However, the filtered back projection method does not directly use the inverse 2D Fourier transform. In order to use the Fourier slice theorem from equation 6.15 in equation

6.16, a change of coordinates $(k_x, k_y) \rightarrow (k_\xi \cos\theta, k_\xi \sin\theta)$ has to be made in the right hand side of equation 6.16:

$$\epsilon(x,y) = \frac{1}{4\pi^2} \iint \hat{\epsilon}(k_\xi \cos\theta, k_\xi \sin\theta) e^{ik_\xi(x\cos\theta + y\sin\theta)} |k_\xi| \, \mathrm{d}k_\xi \, \mathrm{d}\theta \tag{6.17}$$

$$= \frac{1}{4\pi^2} \iint \hat{I}(k_\xi, \theta) e^{ik_\xi(x\cos\theta + y\sin\theta)} |k_\xi| \, \mathrm{d}k_\xi \, \mathrm{d}\theta. \tag{6.18}$$

Finally, equation 6.18 can be written as

$$\epsilon(x,y) = \int Q(x\cos\theta + y\sin\theta, \theta) \, \mathrm{d}\theta, \tag{6.19}$$

where the *filtered projection* $Q(\xi, \theta)$ is defined as

$$Q(\xi,\theta) = \frac{1}{4\pi^2} \int \hat{I}(k_\xi, \theta) e^{ik_\xi t} |k_\xi| \, \mathrm{d}k_\xi. \tag{6.20}$$

Apart from a factor $(2\pi)^{-1}$, the filtered projection can be interpreted as the 1D inverse Fourier transform of the function $\hat{I}(k_\xi, \theta)|k_\xi|$, which explains its name: first $I(\xi, \theta)$ is Fourier transformed, then the filter $|k_\xi|$ is applied, and finally the result is inverse Fourier transformed.

Since this linear filter amplifies the highest frequencies most, it can cause problems for measurements with a significant amounts of noise. Often, an additional filter that cuts the highest frequencies is applied. The filter can also be disregarded, resulting in *unfiltered back projection*. This however blurs the finer structures and details in the result.

In short, the filtered back projection algorithm works as follows:

- $I(\xi, \theta)$ is measured for a fixed angle θ,
- $I(\xi, \theta)$ is 1D Fourier transformed with respect to ξ (eq. 6.11): $\hat{I}(k_\xi, \theta) = \mathcal{F}_1[I(\xi, \theta)]$,
- $\hat{I}(k_\xi, \theta)$ is multiplied by a linear filter: $\hat{I}(k_\xi, \theta)|k_\xi|$,
- $\hat{I}(k_\xi, \theta)|k_\xi|$ is inverse 1D Fourier transformed (eq. 6.20): $Q(\xi, \theta) = \frac{1}{2\pi}\mathcal{F}_1^{-1}[\hat{I}(k_\xi, \theta)]$,
- $Q(\xi, \theta)$ is 'back projected' in the same direction $I(\xi, \theta)$ is recorded (eq. 6.19): $\epsilon(x, y) = Q(x\cos\theta + y\sin\theta, \theta)$.

This process is repeated for all angles θ and the resulting $\epsilon(x, y)$ are superimposed to reconstruct the original distribution. Notice that in the last step each point along the same line-of-sight receives the same contribution. So the back projection step can be seen as 'reverse binning'.

6.2 Experimental set-up

As shown in figure 6.5, a UV camera lens (Nikon UV-Nikkor 105 mm f/4.5) and an additional quartz lens are used to image the light emitted by the discharge onto the detector of the ICCD camera (Stanford Computer Optics 4Picos). The ICCD camera is triggered by the same function generator that triggers the pulsed power supply. The camera's delay and exposures times are set through the software. The gate signal of the ICCD is also recorded on the oscilloscope together with the voltage and current characteristics.

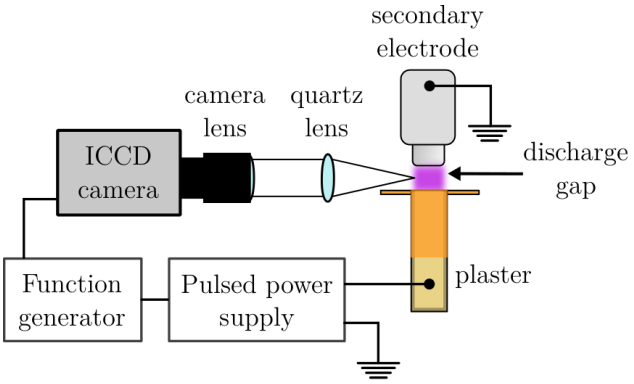

Figure 6.5: Schematic drawing of the setup used for imaging of the light emitted by the discharge. The purple region indicates the discharge gap where discharges occur and plasma is generated.

For both plasters an exposure time of 5 ns is used to record different stages of the discharge on the rise of the pulse. Since there is a 10 to 20 ns jitter on the discharge current peak, the recorded ICCD gate signal and current signal are used to determine the relative position in time between an exposure and the beginning of the discharge current peak.

To determine the discharge distribution on the rise of the pulse for the plane plaster, the Fourier-based Abel inversion method is applied to the intensity measurement from a single discharge using an exposure time of 100 ns. Before processing the recorded intensity is integrated vertically over the gap width. A MATLAB implementation of the Fourier-based Abel inversion method that is available at [53] is used to calculate the radial emission coefficient profile.

In order to use the inverse Radon transform to obtain the discharge distribution of the meshed plaster, the holder assembly is mounted to a rotating stage. The intensity from the discharge on the rise of the pulses is recorded at 12 different angles successively with intervals of 15° and an exposure time of 100 ns. For each angle the measured intensity is vertically integrated across the gap. The inverse Radon transform is performed using the `iradon` function from MATLAB's IMAGE PROCESSING TOOLBOX. This MATLAB function uses the back projection algorithm and has customisable filters.

6.3 Results

ICCD images showing the first 20 ns of the discharge with 5 ns exposure times are shown in figure 6.6 and figure 6.7 for the plane plaster and meshed plaster respectively, the time in upper left corners of the images indicates the start of the exposure relative to the start of the discharge current peak. After 20 ns from the start of the discharge no emission is visible on the images from the ICCD camera anymore.

The local emission coefficient for the plane plaster is shown in figure 6.8. Cosine functions up to order $N = 10$ could be used in the calculation using the Fourier-based Abel inversion method. Using higher orders resulted in multiple local minima and maxima in the radial profile, which are not expected in the current geometry.

Figure 6.9 shows the emission coefficient calculated for the meshed plaster by the inverse Radon transform. Because a significant amount of noise was present in the measurements, unfiltered back projection was used.

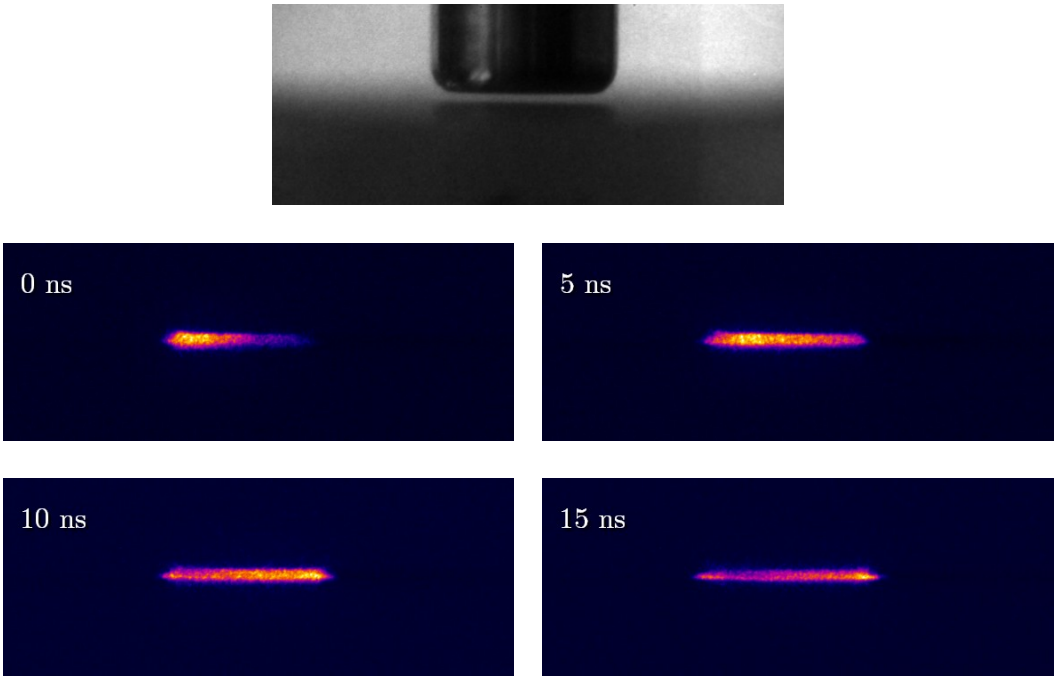

Figure 6.6: ICCD photographs of the emission from the first 20 ns of the discharge on the rise of the pulse for the **plane plaster**. The top photograph shows what is included in the frame. All other photographs are single exposures with an exposure time of 5 ns. The time indicates the delay relative to the inception of the discharge.

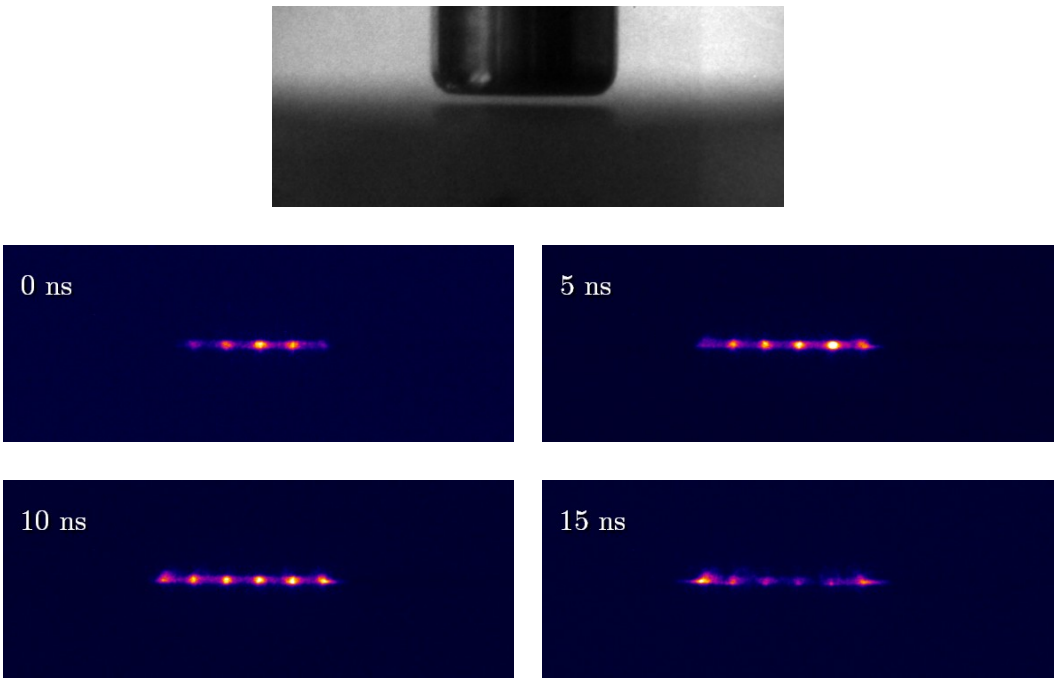

Figure 6.7: ICCD photographs of the emission from the first 20 ns of the discharge on the rise of the pulse for the **meshed plaster**. The top photograph shows what is included in the frame. All other photographs are single exposures with an exposure time of 5 ns. The time indicates the delay relative to the inception of the discharge.

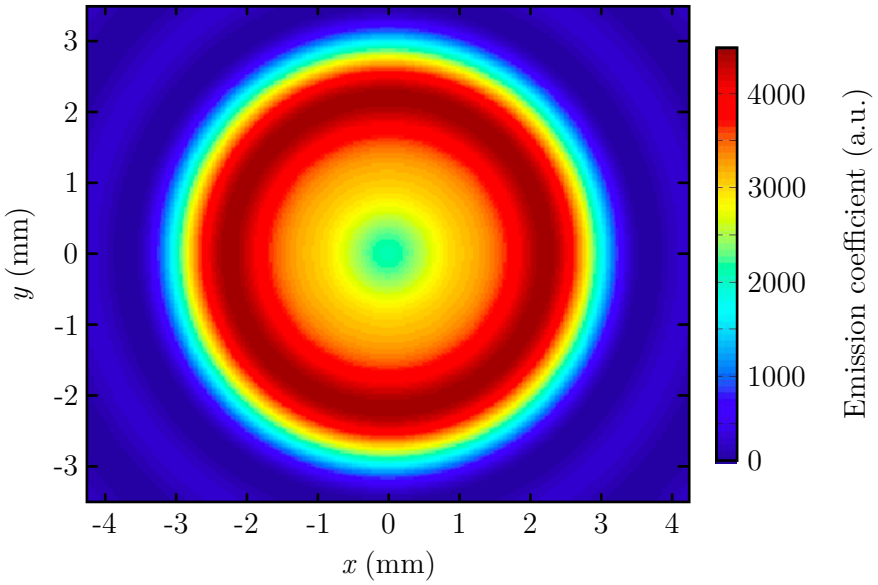

Figure 6.8: Local emission of the **plane plaster** obtained by the Fourier-based Abel inversion method using cosine functions up to order $N = 10$.

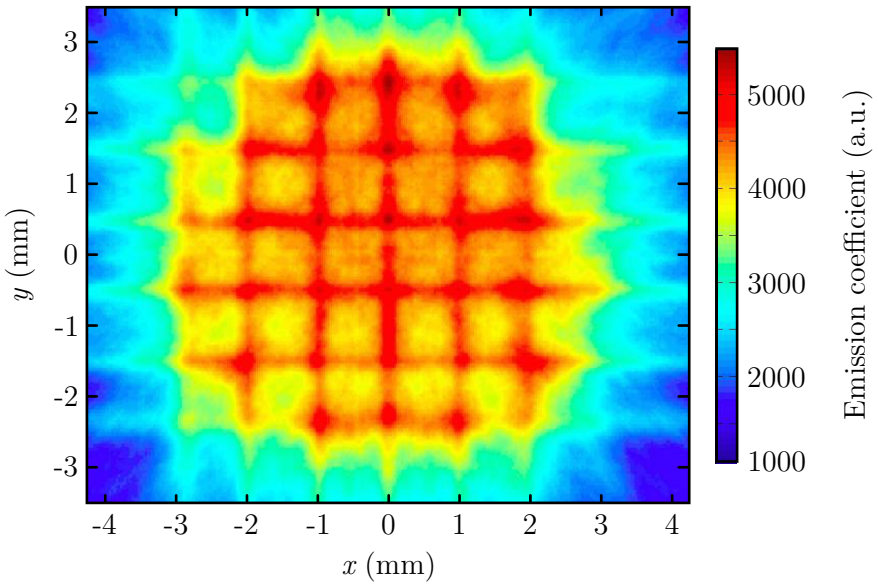

Figure 6.9: Local emission of the **meshed plaster** obtained by unfiltered back projection of 12 intensity profiles measured at different angles with an interval of 15°.

6.4 Discussion

6.4.1 Discharge mode

To analyse the ICCD photographs in figures 6.7 and 6.6, it must be considered what is visible on the time scale of 5 ns. Typical streamer velocities in ambient air are of the order 10^5 m/s [54, 55], which means that they would cross the gap in approximately 5 ns. So, the current temporal resolution would not suffice to observe the development of individual streamers. However, if the discharge was driven by streamer breakdown, bright channels of typically 10 to 100 µm wide, corresponding to streamers and the resulting filaments [17,19], should still have been visible. No such structures were observed in any case. So, together with the single discharge current peaks presented in Chapter 5, it is concluded that the discharge is diffuse for both plasters. Measurements of the gas temperature and reduced electric field, which will be presented in the following two chapters, provide further support to this conclusion.

The short gap width of 0.5 mm is believed to suppress the occurrence of streamers: if the electron density in an avalanche cannot grow large enough to satisfy Meek's criterion (equation 2.10) before it crosses the gap, the formation of streamers is prevented and a diffuse discharge is achieved. As mentioned in Chapter 2, other factors that can facilitate a diffuse discharge have been reported in literature. They are now reviewed and their relevance to the present case is discussed.

Using the example of a pure nitrogen DBD, it was proposed in [31, 32] that it is necessary to have a uniform pre-ionisation to obtain a diffuse discharge and that nitrogen metastables play an important role. Collisions between nitrogen metastables remaining from the previous discharge could provide a uniform electron density through Penning ionisation before the discharge, which will result in many overlapping avalanches and hence a diffuse discharge [32]. Alternatively, a flux of remaining nitrogen metastables may result in the uniform emission of secondary electrons at the cathode [29].

However, as shown in [56], the presence of oxygen leads to rapid quenching of excited nitrogen states. With a repetition rate of 1 kHz, the time between subsequent voltage pulses is 1 ms. On this timescale no significant amounts of nitrogen metastables survive in the presence of oxygen at atmospheric pressure, and it can be assumed that the gas returns to its initial conditions between pulses [4]. Nitrogen metastables are therefore unlikely to play an important role in obtaining a diffuse discharge in the present case.

It is shown in [34] that pre-ionisation by nitrogen metastables is indeed not a necessary requirement for a diffuse DBD in oxygen containing gas mixtures. Instead, it is suggested that a diffuse DBD may be obtained by specific barrier materials and electronic stabilisation by a 'choking coil' in series with the discharge cell. The coil provides electronic feedback and prevents the fast current increase. In the present electronic set-up, the 1 kΩ series resistor also provides negative feedback. As discussed in Chapter 5, the discharge current causes a voltage drop across the series resistor, which results in a decrease in voltage across the cell that is visible in the voltage characteristic. However, to determine whether this has an effect on the discharge, additional measurements with other series resistors should be performed.

Finally, according to [33], the surface resistance of the dielectric material plays a important role in the transition from streamer to Townsend breakdown. A surface resistance lower than 10^{11} Ω/sq strongly favours Townsend breakdown. In this case, charge on the dielectric can distribute more uniformly, resulting in a diffuse discharge. Additionally, it was also demonstrated in [33] that the surface resistance of a glass barrier decreased by over an order of magnitude from exposure to an air discharge. The surface resistance of

the polyimide film that is used as barrier for the plasters is specified as $3 \times 10^{12}\,\Omega/\text{sq}$ [57], but no measurements were performed to analyse if and by how much this changes when the material is exposed to plasma.

6.4.2 Discharge distribution

From figure 6.8 it is observed that the emission from the plane plaster is concentrated around a circle approximately 2 mm from the centre. Comparing this to the electrostatic field simulations in the left parts of figures 4.5 and 4.6 suggests that this corresponds to the field enhancement caused by the round edges of the secondary electrode. The same circular structure is also recognised in the degradation pattern of the polyimide barrier after operation. This shows that for the plane plaster the discharge distribution is determined by the shape of the secondary electrode.

For the meshed plaster, the structure of the mesh is readily recognised in the emission distribution in figure 6.9. Additionally, the barrier now also shows a more uniform degradation pattern along the mesh. So, contrary to the plane plaster, it is concluded that the discharge distribution in the gap using the meshed plaster is determined by the plaster itself instead of the secondary electrode. The fact that the discharge distribution in the gap for the meshed plaster is controlled by the plaster itself rather than by the shape of the secondary electrode is particularly useful for the treatment of uneven surfaces such as wounds.

When comparing the emission from the meshed plaster to the electrostatic simulations, a notable difference is observed. The highest field enhancement is obtained at places *between* intersections of the mesh, while the highest emission is measured *at* the intersections of the mesh. Generally, locations of high electric field and high emission do not have to coincide. Also, the emission is vertically integrated over the gap width and the differences in local field enhancement become less pronounced towards the anode. Finally, it should be realised the finest details in emission distribution may not be visible in figure 6.9, since no filter was used in the back projection of the intensity profiles. It may be possible in future measurement to improve the signal-to-noise ratio by accumulating the light from multiple pulses. Applying filtered back projection would then result in an emission profile with more details.

Chapter 7

Gas Temperature

The gas temperature is an important plasma parameter because it greatly affects the plasma chemistry. Additionally, in the perspective of wound treatment, temperatures need to remain close to room temperature. For these reasons knowledge on the gas temperature is essential. Determining the gas temperature in a highly transient plasma requires some careful consideration. Optical emission spectroscopy offers a non-invasive technique to obtain the gas temperature from the rotational rotational distribution in an emission spectrum, if certain equilibrium conditions are met. The method and its requirements are explained in section 7.1. To obtain quantitative information the spectral measurements are fitted to calculated spectra. The code that is programmed to do this is described in section 7.2. Finally, in section 7.3 and 7.4 the results will be shown and discussed respectively.

7.1 Method

To obtain the gas temperature, the rotational band structure of the $C\,^3\Pi_u \rightarrow B\,^3\Pi_g$ transition of N_2 is measured using optical emission spectroscopy (OES). This electronic transition is often referred to as the second positive system (SPS) and is usually responsible for the dominant emission in air or N_2 containing plasmas. The band head of the (0,0) vibrational transition is located at 337.1 nm.

If there is rotational equilibrium in the upper electronic state $C\,^3\Pi_u$, the population of the rotational levels obeys the Boltzmann distribution. The corresponding rotational temperature T_{rot} can then be determined from the relative intensities of the rotational band structure. In addition, if there is also rotational-translational equilibrium, the gas temperature T_{gas} can be approximated by $T_{gas} \approx T_{rot}$.

First, the method to obtain the rotational temperature from relative intensity measurements will be further explained. In the second part of this section the requirements for rotational-translation equilibrium will be discussed.

7.1.1 Relative intensity distribution in a rotational band

To obtain the rotational temperature from an emission spectrum, the intensity distribution of rotational lines must be considered. In fact, it suffices to analyse the rotational structure of a single vibronic transition. This means that only those factors of equation 3.33 that depend on the rotational state have to be considered. The intensity of a rotational line in this case reduces reduces to:

$$I_{J''}^{J'} \propto n_{J'} \nu A_{J''}^{J'} \propto n_{J'} \nu^4 \frac{S_{J''}^{J'}}{g_{J'}}, \tag{7.1}$$

where $S_{J''}^{J'}$ is the Hönl-London coefficient (line strength) and $g_{J'}$ is the degeneracy of the upper state J'. In case of a Boltzmann distribution, $n_{J'}$ is given by

$$n_{J'} = g_{J'} \exp\left(\frac{-hcF(J')}{kT_{rot}}\right), \tag{7.2}$$

where $F(J')$ is the rotational term energy that was discussed in Chapter 3. Inserting equation 7.2 into equation 7.1 gives

$$I_{J''}^{J'} \propto \nu^4 S_{J''}^{J'} \exp\left(\frac{-hcF(J')}{kT_{rot}}\right). \tag{7.3}$$

A commonly used method to extract the temperature data from a rotational spectrum is by making a so-called Boltzmann plot. When the natural logarithm of $I_{J''}^{J'}/\nu^4 S_{J''}^{J'}$ is plotted against the rotational energy, the temperature can be determined from the slope:

$$\ln\left(\frac{I_{J''}^{J'}}{\nu^4 S_{J''}^{J'}}\right) = -hcF(J')\frac{1}{kT} + \text{const.} \tag{7.4}$$

The Boltzmann plot method is applicable if the measured spectrum has sufficient spectral resolution and the individual rotational lines can be resolved.

Alternatively, the rotational temperature can be obtained by fitting the measured spectrum to a calculated spectrum with the temperature as fit parameter. This is the method that will be used here. Thus, a code that calculates the spectrum as function of temperature is required. While commercial software such as Specair [58] exists that has this kind of functionality, a code is built using Matlab to maintain full control over the calculation and fit procedures. This code will be further discussed in section 7.2.

7.1.2 Translational-rotational equilibrium

As mentioned, the gas temperature is only equal to the rotational temperature if there is translational-rotational equilibrium. Such an equilibrium exists if either the rotational distribution is a thermalised distribution, or if rotational energy transfer (RET) processes are fast enough to thermalise the rotational distribution.

In general, it can be assumed that the rotational distribution of ground state species is thermalised because its lifetime is long enough to allow many collisions with heavy particles. If the excited state is populated by electron impact excitation from the ground state, the thermalised rotational distribution of the ground state carries over to the excited state [59].

Regarding the N_2 SPS, electron impact excitation from the ground state is usually the dominant production mechanism of $N_2(C\,^3\Pi_u)$. Stepwise excitation is hardly possible in air atmospheric pressure because of the effective collisional quenching of excited states by molecular oxygen [60]. In Chapter 8 quenching processes will be discussed in more detail. There are only few examples reported in literature where the rotational distribution of $N_2(C\,^3\Pi_u)$ is *not* in equilibrium with the gas temperature. The most notable exception is when N_2/Ar gas mixtures are used. In this case, the excitation by the metastable $Ar(^3P_2)$ state can become an important population process for $N_2(C\,^3\Pi_u)$ and must be taken into account in the determination of the temperature. However, the effects of the low amounts of argon present in atmospheric air the can be safely neglected [61].

7.2 Line-by-line radiation code

A line-by-line radiation code is programmed to fit the measured spectra and obtain a temperature. Basically, the code calculates the contribution of each of the rotational lines of the SPS to the total intensity separately and in the end adds them all up. Before discussing how the contribution of each of the lines is determined, some simplifications are made.

The SPS is a triplet-triplet system and thus both the upper and lower state have three substates. Hence the system has three principal subbands resulting from spin multiplet splitting. The splitting between these subbands is approximately of the order 80 pm. Since the presented code is intended for application when the rotational lines remain unresolved, it is justified to neglect spin multiplet splitting and combine their contributions to the spectrum into a single line. This will be done by combining their line strengths.

First, the code calculates the wavelengths corresponding to the rotational lines of the vibronic transition of interest by

$$\lambda = \left[T'_e - T''_e + T(v', J') - T(v'', J'')\right]^{-1}, \tag{7.5}$$

where T_e and $T(v, J)$ are the electronic term energy and Dunham expansion respectively, as defined in Chapter 3. The spectroscopic constants that are used by the code are summarised in Appendix B.

Next, relative intensities are assigned to the lines using equation 7.3. The line strengths depend on whether the transition belongs to Hund's case (a) or Hund's case (b). For low values of J, both the upper and lower state of the SPS belong to Hund's case (a), but evolve to Hund's case (b) for larger values of J. Expressions exists for the intermediate case between (a) and (b), but they are more sophisticated then what is currently required, especially since at large values of J the difference between the two cases becomes negligible. For this reason line strengths for Hund's case (a) are used for all values of J. Combining

the contributions of the three subbands into a single line, the following line strengths are obtained for the P-, Q and R-branches by Phillips [62]:

$$S_P(J') = 6(J'+1) - \frac{10}{J'+1}, \tag{7.6}$$

$$S_Q(J') = \frac{10}{J'} + \frac{10}{J'+1}, \tag{7.7}$$

$$S_R(J') = 6J' - \frac{10}{J'}, \tag{7.8}$$

where the subscript indicates the branch.

Every line is then separately convoluted with a line profile and the result of all the lines is summed to generate the spectrum. Either an experimentally measured line profile can be provided, or a combination of a Gaussian and Lorentzian full width at half maximum (FWHM) can be set. Finally, the calculated spectrum is multiplied by a scaling factor and a constant background is added if necessary.

The fitting procedure is based on the linear least squares method and is implemented using the `fit` function from MATLAB's CURVE FITTING TOOLBOX. Several parameters are varied in the fitting process: the temperature, a constant and linear wavelength shift, a scaling factor, a constant background intensity and, if no experimentally measured line profile provided, the Gaussian and Lorentzian FWHMs.

The constant wavelength shift and linear wavelength shift are intended to make small corrections to the wavelengths assigned to the pixels of the spectrometer. For a good fit it is crucially important that the initial values for these two parameters are close to their actual values. After the best fit is found, the program returns the values for the fit parameters as well as the 95% confidence interval of these values.

7.3 Experimental set-up

The set-up that is used for the spectral measurements is shown in figure 7.1. Two plano-convex quartz lenses image the light emitted by the discharge onto the entrance slit of the monochromator (Jobin-Yvon THR1000). The monochromator is of the Czerny-Turner type with an optical path length of 1 m and has a spectral range of about 11 nm. The centre wavelength is set to 337.0 nm and an entrance slit width is 250 µm is used.

Spectra are recorded by an ICCD camera (Stanford Computer Optics 4QuickE). The camera is triggered by the same function generator that triggers the pulsed power supply. The delay and gate times are controlled through the camera's software. An intensity calibrated deuterium hollow cathode lamp is used to calibrate the relative sensitivity of the optical system. The line profile is measured using an atomic line from a low pressure mercury gas discharge lamp. To improve the signal-to-noise ratio, the CCD module of the camera is cooled to approximately 3 °C by attaching a Peltier element and a water cooled copper plate.

7.4 Results

For both the meshed and the plane plaster separate spectra are recorded for the discharge on the rise of the pulse and the discharge on the fall of the pulse. This is achieved by appropriately setting the delay such that the gate time concurs with one of the discharges.

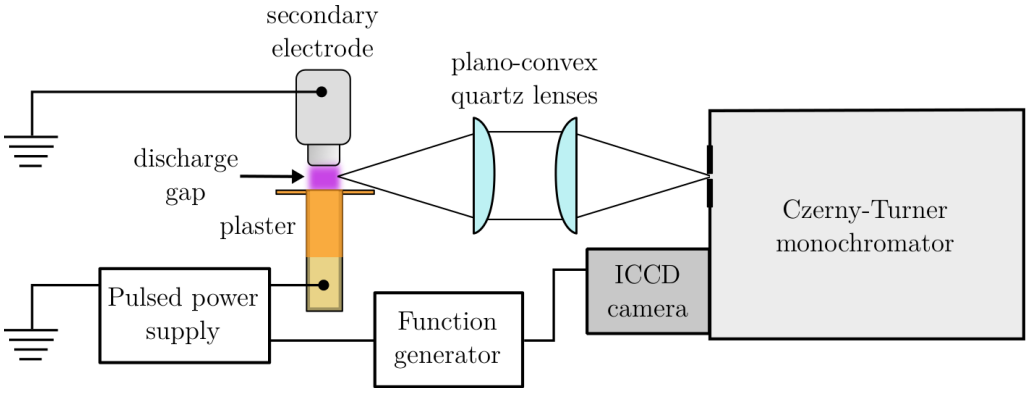

Figure 7.1: Illustration of the setup that is used for optical emission measurements. The purple region indicates where discharges occur and plasma is generated.

In each case the camera was gated for 100 ns during every pulse. Even with a relatively large slit width of 250 µm, the signal needs to be accumulated over 50 000 pulses in order to acquire a spectrum that can be used for further analysis. The plasters are operated at 6.5 kV, where the emission intensity is highest before the outward branching of the discharge on meshed plaster starts.

The measured spectra for the meshed plaster and the plane plaster are shown in figure 7.2 and figure 7.3 respectively. In both figures the left hand graph corresponds to the discharge on the rise of the pulse and the right hand graph belongs to the discharge on the fall of the pulse. A spectrum is fitted to every row of pixels to obtain a temperature profile. To illustrate, the measured spectrum corresponding to the row at 0 mm from figure 7.2a and its fitted spectrum are shown in figure 7.4. The calculated temperature profiles for the meshed plaster and plane plaster are shown in figures 7.5 and 7.6 respectively. This time in both figures the top graph belongs to the discharge on the rise of the pulse and the bottom graph to the discharge on the fall of the pulse.

7.5 Discussion

In each of the measurements for both plasters the temperature is found only slightly elevated above room temperature in the range of 325 ± 25 K. Within the errors the temperature is uniform across the plaster.

While the effects of the mesh structure can be readily observed in the spectra for the meshed plaster in figure 7.2, no clear structure is present the corresponding temperature profiles in figure 7.5 and 7.2b. The reason for this is that more light is collected at positions where the line-of-sight is directed along the mesh, resulting in higher intensities. However the spectral distribution of the intensity is approximately independent of the position, resulting a flat temperature profile. The positions with higher intensities do however result in lower errors. For example, the low intensity in 7.2 at position $x = -0.5$ mm is reflected in the relatively large error in temperature for that same position in figure 7.5.

The differences that are found in the temperature profiles between the two plasters are small and well within the errors. This means that the local electric field enhancement resulting form the structured electrode has no significant effect on the gas temperature. Even though electrons may be accelerated to higher speeds in the enhanced field, the short pulses still prevent electron driven gas heating. This fact can potentially be used to tune the reduced electric field, and hence the electron temperature, by appropriately choosing

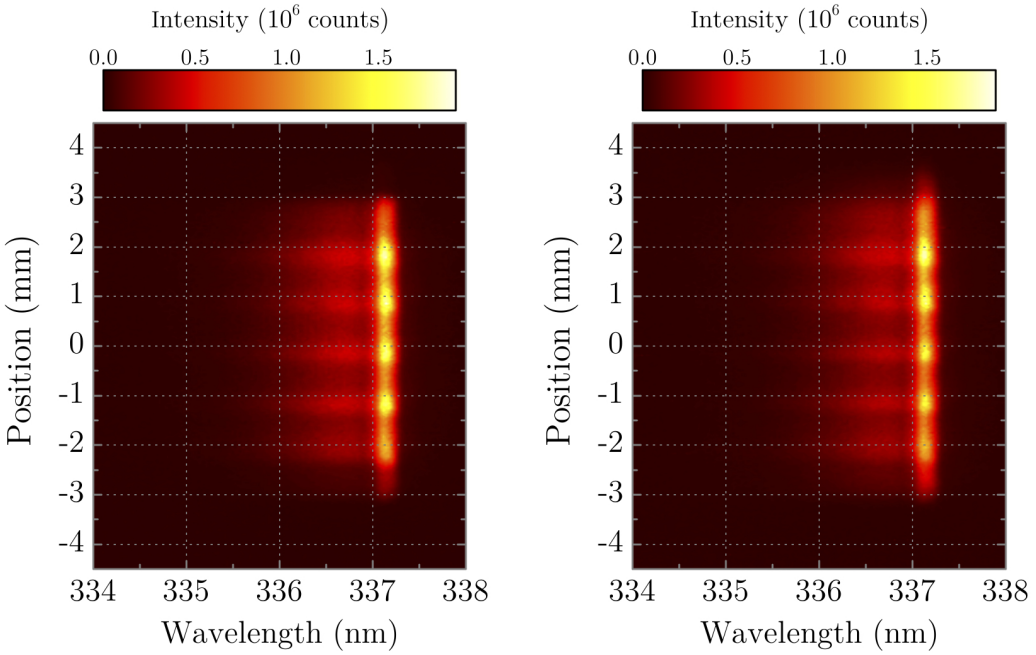

(a) Discharge on the rise of the pulse. **(b)** Discharge on the fall of the pulse.

Figure 7.2: Measured spectra for the **meshed plaster**. The position is relative to the centre of the secondary electrode.

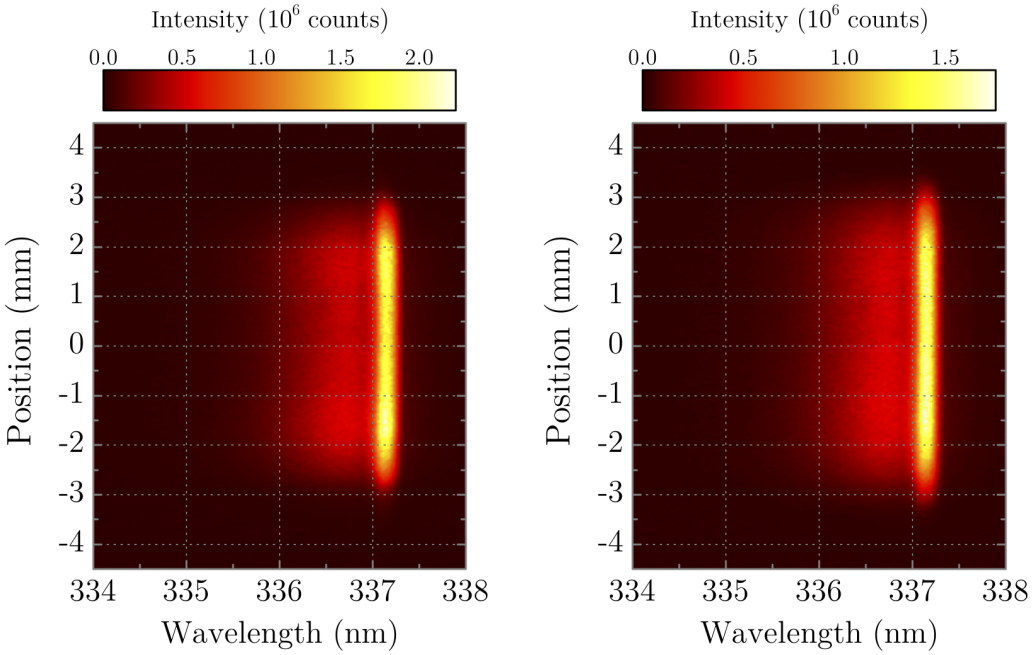

(a) discharge at the rise of the pulse. **(b)** discharge at the fall of the pulse.

Figure 7.3: Measured spectra for the **plane plaster**. The position is relative to the centre of the secondary electrode.

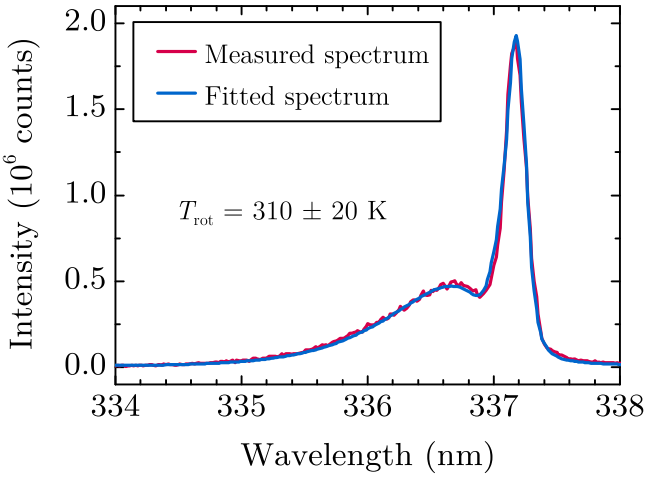

Figure 7.4: Measured (red) and fitted (blue) spectrum for the centre of the meshed plaster (0 mm in figure 7.2a).

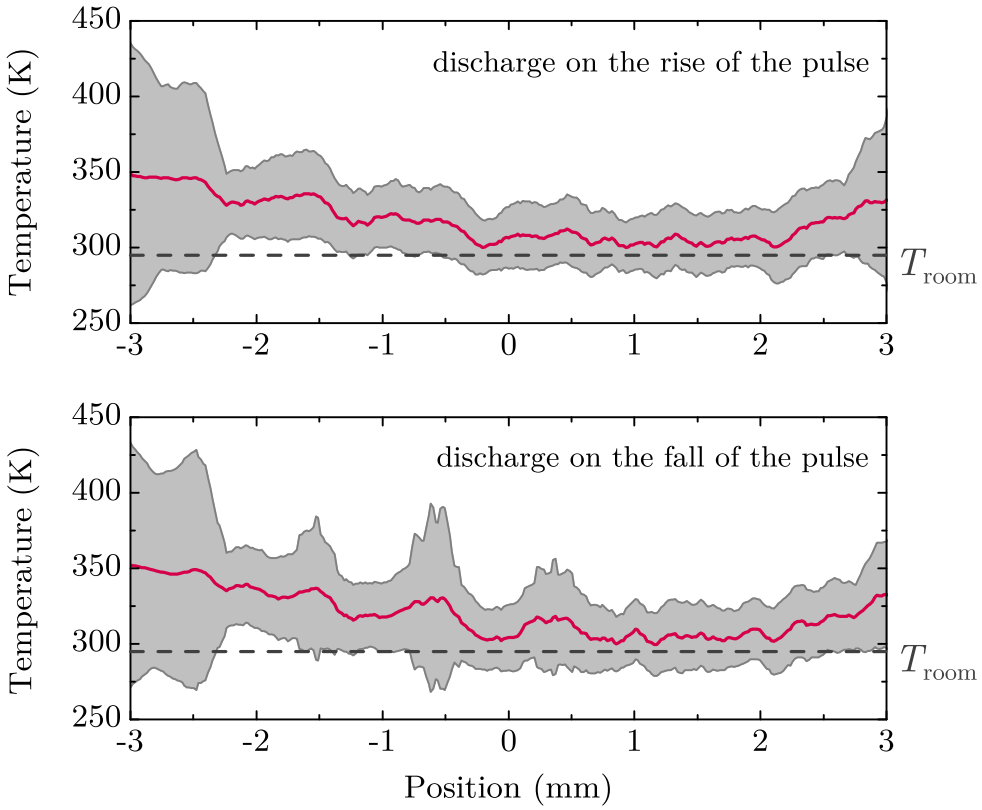

Figure 7.5: Temperature profile for the **meshed** plaster. The grey area indicates the 95% confidence interval and the position is relative to the centre of the secondary electrode. The dashed line represents the ambient temperature of $T_{room} \approx 295\,K$.

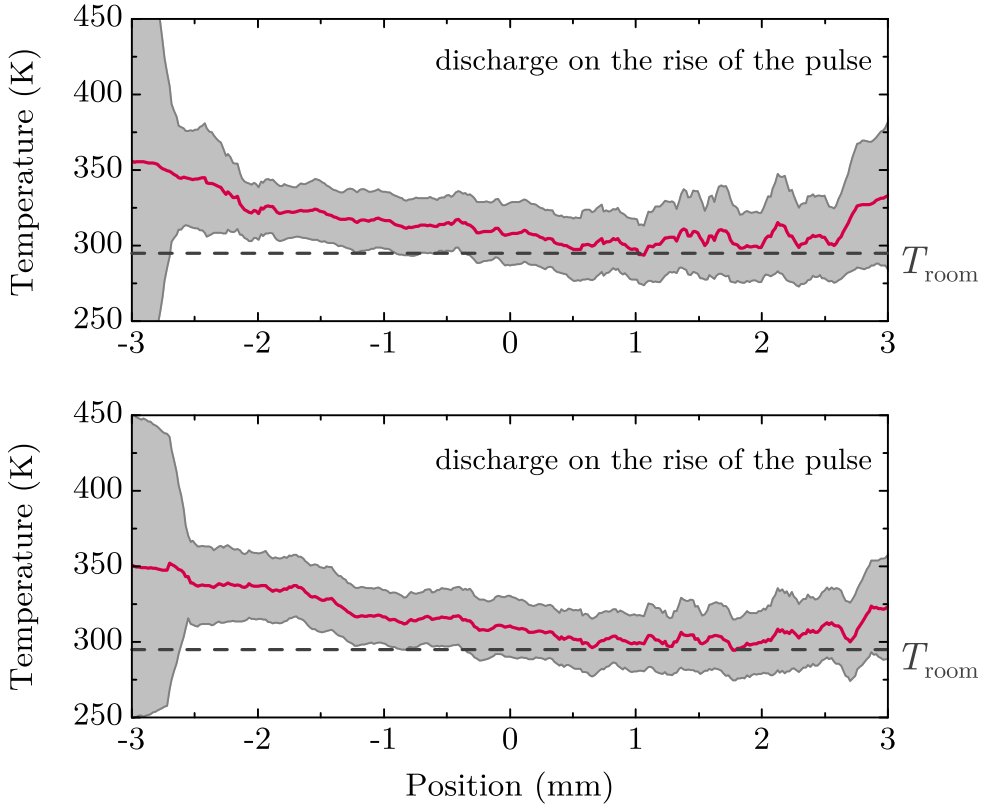

Figure 7.6: Temperature profile for the **plane** plaster. The grey area indicates the 95% confidence interval and he position is relative to the centre of the secondary electrode. The dashed line represents the ambient temperature of $T_{\mathrm{room}} \approx 295\,\mathrm{K}$.

the mesh pattern without influencing the gas temperature. This point is further explored in the next chapter.

Only measurements at an operation voltage of 6.5 kV were performed. Since the power dissipation decreases for lower voltages (see figure 5.9), it reasonable to expect that gas temperature will decrease for lower voltages as well. This means that the presented measurements at 6.5 kV can serve as an indication of the upper limit of the gas temperature for operation voltages at and lower than 6.5 kV.

In order to attain higher spectral or temporal resolution, measure the temperature at lower voltages and to reduce uncertainties in future measurements, the signal-to-noise ratio of the measurements has to be increased. Lower noise levels may be obtained by further cooling the CCD. Currently, cooling the CCD below 3 °C resulted in condensation. This can be prevented by flushing the camera's enclosure with dry air. To improve the signal, cylindrical lenses could be used instead of spherical lenses to focus a larger amount of light onto the slit without losing spatial resolution. Originally, one of the reasons for preserving the spatial resolution was to determine whether spectrally resolved tomographic techniques, like Abel inversion or the inverse Radon transform, were feasible. This would however require a dramatic increase in signal-to-noise ratio.

The gas found temperatures of around 325 K are in agreement with a diffuse discharge. In literature, local temperatures exceeding 500 K are sometimes found for filamentary discharges in air [4, 63].

Finally, in perspective of the application, with gas temperatures around 325 K the plasters can be safely applied to wounds.

Chapter 8

Reduced Electric Field

Another plasma parameter that is accessible by optical emission spectroscopy is the reduced electric field E/N, which is defined as the electric field E normalised to the background density N. Electric fields are essentially what drives the discharge, and the reduced electric field plays an important role in the energy distribution of electrons. Furthermore, it is believed that delivering electric fields to a wound may be important to stimulate cell regeneration, making knowledge of this parameter even more valuable. Section 8.1 discussed two approaches to calculate the reduced electric field from the ratio of emission lines from N_2 and N_2^+. The set-up is virtually identical to the one discussed in Chapter 7, but will nevertheless be briefly summarised in section 8.2. Finally, the result are shown in section 8.3 and subsequently discussed in section 8.4.

8.1 Method

Two approaches to obtain the reduced electric field from emission line ratios are proposed in literature [59]. Both of them rely on optical emission spectroscopy. The (0,0) and (2,5) vibrational transitions of the N_2 second positive system (SPS),

$$N_2(C\,^3\Pi_u, 0) \rightarrow N_2(B\,^3\Pi_g, 0) + h\nu \qquad \lambda_{head} = 337.1\,\text{nm}, \tag{8.1}$$

$$N_2(C\,^3\Pi_u, 2) \rightarrow N_2(B\,^3\Pi_g, 5) + h\nu \qquad \lambda_{head} = 394.3\,\text{nm}, \tag{8.2}$$

and the (0,0) vibrational transition of the N_2^+ first negative system (FNS),

$$N_2^+(B\,^2\Sigma_u^+, 0) \rightarrow N_2^+(X\,^2\Sigma_g^+, 0) + h\nu \qquad \lambda_{head} = 391.4\,\text{nm} \tag{8.3}$$

need to be measured to obtain the reduced electric field. The positions of the band heads of these transitions are indicated by λ_{head}. As discussed in Chapters 3 and 7, the intensities of the transitions are proportional to the number density of the upper state. To see how the intensity ratio is related to the reduced electric field, the population and depopulation processes of the upper states need to be considered.

It is assumed that electronic quenching prevents stepwise excitation and that the dominant population processes are therefore electron impact excitation and electron impact ionisation from the ground state:

$$e + N_2(X\,^1\Sigma_g^+, v) \rightarrow e + N_2(C\,^3\Pi_u, v) \qquad E_{thres} = 11.03\,\text{eV}, \tag{8.4}$$

$$e + N_2(X\,^1\Sigma_g^+, v) \rightarrow e + e + N_2^+(B\,^2\Sigma_u^+, v) \qquad E_{thres} = 18.7\,\text{eV}, \tag{8.5}$$

where E_{thres} is the threshold energy for the process. Only electrons with an energy above the threshold energy E_{thres} can bring about excitation or ionisation. The population of the excited and ionised states as well as the associated rate coefficients are hence related to the electron energy distribution function (EEDF), which depends on the reduced electric field.

In principle, any combination of the SPS (0,0), (2,5) and FNS (0,0) vibrational transitions can be used. However, since the threshold energies for electron impact excitation of the $v = 0 - 4$ vibrational levels differ by less than 1 eV [59], using just the SPS transitions is a much less sensitive choice.

The two approaches to calculate the reduced electric field are now explained. The first is a theoretical approach based on a kinetic model for population and depopulation processes. Accurate collisional data is thus required for this approach. The second approach is based on the empirical determination of the intensity ratios in conditions where the reduced electric field could be controlled [64].

To simplify the notation, the electronic upper state of the SPS ($C\,^3\Pi_u$) will be referred to as the 'C state' and the electronic upper state of the FNS ($B\,^2\Pi_u$) as the 'B state' in the remainder of this chapter.

8.1.1 Theoretical approach

The first approach is the *theoretical approach*. In this method a kinetic model for the population and depopulation of the C and B states is used to establish a relation between the intensity ratio of the SPS (0,0) and the FNS (0,0) vibronic transitions and the reduced electric field. In the assumption that both states are only populated by electron impact

excitation (for C) or ionisation (for B) from the ground state, and that the depopulation is dominated by collisional quenching from N_2 and O_2 and optical emission, the following equations for the number densities of C state n_{C} and the B state n_{B} can be written:

$$\frac{\mathrm{d}n_{\mathrm{C}}}{\mathrm{d}t} = k_C n_{\mathrm{N_2}} n_{\mathrm{e}} - n_{\mathrm{C}} \left[Q_{\mathrm{C}}^{\mathrm{N_2}} n_{\mathrm{N_2}} + Q_{\mathrm{C}}^{\mathrm{O_2}} n_{\mathrm{O_2}} \right] - \frac{n_{\mathrm{C}}}{\tau_0^{\mathrm{C}}}, \tag{8.6}$$

$$= k_C n_{\mathrm{N_2}} n_{\mathrm{e}} - \frac{n_{\mathrm{C}}}{\tau_{\mathrm{eff}}^{\mathrm{C}}}, \tag{8.7}$$

$$\frac{\mathrm{d}n_{\mathrm{B}}}{\mathrm{d}t} = k_B n_{\mathrm{N_2}} n_{\mathrm{e}} - n_{\mathrm{B}} \left[Q_{\mathrm{B}}^{\mathrm{N_2}} n_{\mathrm{N_2}} + Q_{\mathrm{B}}^{\mathrm{O_2}} n_{\mathrm{O_2}} \right] - \frac{n_{\mathrm{B}}}{\tau_0^{\mathrm{B}}}, \tag{8.8}$$

$$= k_C n_{\mathrm{N_2}} n_{\mathrm{e}} - \frac{n_{\mathrm{C}}}{\tau_{\mathrm{eff}}^{\mathrm{C}}}. \tag{8.9}$$

Here k_{C} and k_{B} are the electron impact excitation and electron impact ionisation rate coefficients, respectively, and are assumed to be solely a function of E/N. Next, n_e, $n_{\mathrm{N_2}}$ and $n_{\mathrm{O_2}}$ are the electron density, ground state N_2 density and ground state O_2 density. The coefficient for quenching by N_2 and O_2 are $Q^{\mathrm{N_2}}$ and $Q^{\mathrm{O_2}}$. And finally, τ_0 is the radiative lifetime, which can be combined with the quenching terms to form the effective lifetime τ_{eff}.

Again the intensity of the transition follows from equation 3.33:

$$I_{\mathrm{C}} = \nu_{\mathrm{C}} n_{\mathrm{C}} \frac{1}{\tau_0^{\mathrm{C}}}, \tag{8.10}$$

$$I_{\mathrm{B}} = \nu_{\mathrm{B}} n_{\mathrm{B}} \frac{1}{\tau_0^{\mathrm{B}}}. \tag{8.11}$$

where the transition probability is now replaced by the radiative lifetime $A = \tau_0^{-1}$. Now n_C and n_B can be solved from equations 8.10 and 8.11 and substituted in equations 8.7 and 8.9, which leads to:

$$\frac{\tau_0^{\mathrm{C}}}{\nu_{\mathrm{C}}} \left(\frac{I_{\mathrm{C}}}{\tau_{\mathrm{eff}}} + \frac{\mathrm{d}I_{\mathrm{C}}}{\mathrm{d}t} \right) = k_C n_{\mathrm{N_2}} n_{\mathrm{e}}, \tag{8.12}$$

$$\frac{\tau_0^{\mathrm{B}}}{\nu_{\mathrm{B}}} \left(\frac{I_{\mathrm{B}}}{\tau_{\mathrm{eff}}} + \frac{\mathrm{d}I_{\mathrm{B}}}{\mathrm{d}t} \right) = k_B n_{\mathrm{N_2}} n_{\mathrm{e}}, \tag{8.13}$$

Finally, dividing equation 8.13 by equation 8.12 gives

$$\frac{\tau_0^{\mathrm{B}} \nu_{\mathrm{C}}}{\tau_0^{\mathrm{C}} \nu_{\mathrm{B}}} \frac{\left(\frac{I_{\mathrm{B}}}{\tau_{\mathrm{eff}}} + \frac{\mathrm{d}I_{\mathrm{B}}}{\mathrm{d}t} \right)}{\left(\frac{I_{\mathrm{C}}}{\tau_{\mathrm{eff}}} + \frac{\mathrm{d}I_{\mathrm{C}}}{\mathrm{d}t} \right)} = \frac{k_{\mathrm{B}}}{k_{\mathrm{C}}} = \frac{k_{\mathrm{B}}}{k_{\mathrm{C}}} \left(\frac{E}{N} \right). \tag{8.14}$$

The left hand side of this expression can be measured, and the right hand side is a function of E/N. The steady-state approximation is usually used to avoid the time derivative of the intensity, resulting in:

$$R_{391/337} = \frac{I_{\mathrm{B}}}{I_{\mathrm{C}}} = \frac{\tau_0^{\mathrm{C}} \tau_{\mathrm{eff}}^{\mathrm{B}} \nu_{\mathrm{B}}}{\tau_0^{\mathrm{B}} \tau_{\mathrm{eff}}^{\mathrm{C}} \nu_{\mathrm{C}}} \frac{k_{\mathrm{B}}}{k_{\mathrm{C}}} \left(\frac{E}{N} \right), \tag{8.15}$$

where $R_{391/337}$ is used to indicate the intensity ratio of the transition corresponding to the band head wavelengths in the subscript. Radiative and effective lifetimes are reported

in literature [60] and the k_B/k_C can be calculated from cross sections as function of the reduced electric field by a Boltzmann solver, such as Bolsig+. Cross sections for electron impact excitation of the C state are included in the Bolsig+ distribution. The cross sections for electron impact ionisation for the B state can be obtained from the Phelps database.

This method requires either knowledge on the time derivative of the intensity of the emission lines or a steady-state approximation. Considering the fact that the discharges with the plasters are highly transient and that the accessible time resolution is significantly too low to obtain the time derivative of the line intensity, this method is not suitable in the present case.

8.1.2 Empirical approach

The second approach is based on the experimentally obtained intensity ratios by Paris *et al* [64]. Empirical data was used in [64] to determine the dependence of intensity ratios on the reduced electric field in the pressure range from 300 to 10^5 Pa in a non-self-sustaining Townsend discharge (a discharge in which the condition in equation 2.6 or 2.8 is not met). Because the dependence of the two SPS transitions on the reduced electric field is insufficiently sensitive in the range of applied electric fields that are used in this work, the SPS (2,5) and the FNS (0,0) transitions were measured to obtain the reduced electric field profile for both plasters. The following empirical formula is provided for the $R_{391/394}$ ratio at atmospheric pressure [64]:

$$R_{391/394} = \frac{I_{391}}{I_{394}} = 46 \exp\left[-89\left(\frac{E}{N}\right)^{-0.5}\right]. \tag{8.16}$$

8.1.3 Calculation of intensity ratios from measurements

The line-by-line code is again used to fit a spectrum to each of the peaks:

$$\Phi_{\text{meas}} = a\Phi + b, \tag{8.17}$$

where Φ_{meas} is the measured spectrum, Φ represents the shape of the calculated spectrum, a is the scaling factor and b the constant background. The intensity ratio can then be acquired by:

$$R_{i/j} = \frac{a_i}{a_j}. \tag{8.18}$$

To fit a spectrum to the FNS, the code has to be slightly expanded. Since both the upper and the lower state have $\Lambda = 0$, they strictly belong to Hund's case (b) and there is no Q-branch. If spin multiplet splitting is neglected again, J can be used as rotational quantum number again instead of K, and the line strength are [37]:

$$S_P(J') = J' + 1 \tag{8.19}$$

$$S_R(J') = J' \tag{8.20}$$

Spectroscopic constants that were used are listed in Appendix B.

8.2 Experimental set-up

The measurement are performed using the same set-up as for the temperature measurements in the Chapter 7: two plano-convex quartz lenses are used to image the emission

of the discharge onto the entrance slit of a 1 m Czerny-Tuner monochromator (Jobin-Yvon number) and the output is recorded by an ICCD camera (Stanford 4QuickE). To measure the SPS (2,5) and FNS (0,0) vibrational transitions the centre wavelength of the monochromator is now shifted to 391 nm.

8.3 Results

Since the wavelength range of the monochromator is about 11 nm, the emission from the FNS (0,0) at 391.4 nm and the SPS (2,5) at 394.3 nm could be captured in a single spectrum. Again, separate spectra are recorded for the discharge on the rise of the pulse and the discharge on the fall of the pulse for both plaster by gating the camera for 100 ns and using an appropriate delay. A slit width of 250 µm is used and the signal is accumulated over 50 000 pulses. Like for the temperature measurements, the plasters are operated at 6.5 kV. Since the settings are identical to ones in the chapter 7, with the exception of the wavelength, the measurements from the previous chapter are also used for the electric field calculations.

Figures 8.1 and 8.2 show the spectra for the meshed plaster and the plane plaster respectively. On the left hand side graphs the emission from the discharge on the rise of the pulse is shown and on the right side graphs the emission from the discharge on the fall of the pulse.

Before attempting to calculate the reduced electric field from the spectra, it is useful have an order of magnitude estimation. Since the discharge is diffuse and operates in the Townsend breakdown regime, there are no regions with high local electric field due to the discharge itself. It is therefore assumed that the order of magnitude of the reduced electric field can be estimated by the applied voltage $V = 6.5\,\mathrm{kV}$ divided by the gap width $d = 0.5\,\mathrm{mm}$ ($E = V/d = 13 \times 10^6\,\mathrm{V/m}$) and the background particle number density N_{air}. The particle density in air at atmospheric pressure and 20 °C is $N_{\mathrm{air}} = 2.5 \times 10^{25}\,\mathrm{m^{-3}}$, resulting in a reduced electric field of $E/N = 5.2 \times 10^{-19}\,\mathrm{Vm^2} = 520\,\mathrm{Td}$.

The reduced electric field profile determined from the spectra is shown in figure 8.3.

8.4 Discussion

The reduced electric field for the plane plaster is around the expected 520 Td and the reduced electric field for meshed plaster is found slightly higher around 600 Td, approximately reflecting the 20% local electric field enhancement that was found in the simulations of Chapter 4. This result further corroborates the conclusions from previous chapters that the discharge obtained with both plasters is diffuse. This conclusively shows that the meshed plaster produces a structured diffuse rather than filamentary discharge. As explained in Chapter 2, a filamentary discharge driven by streamer breakdown would typically exhibits local electric field enhancement an order of magnitude larger than the externally applied electric field. In addition, the ability to influence the electric field by structuring the powered electrode opens possibilities in tailoring electric field properties and consequently electron properties in dielectric barrier discharges.

Since the FNS (0,0) intensity is too weak on the fall of the pulse, no reduced electric field could be calculated. However, a qualitative analysis is still possible. It can be readily observed that for both plasters the FNS (0,0) peak has greater intensity than the SPS (2,5) peak on the rise of the pulse (figures 8.1a and 8.2a), but that it is barely visible on the fall of the pulse (figures 8.1b and 8.2b). Considering the threshold energies for the excitation and ionisation processes, this indicates that the average electron energy is much

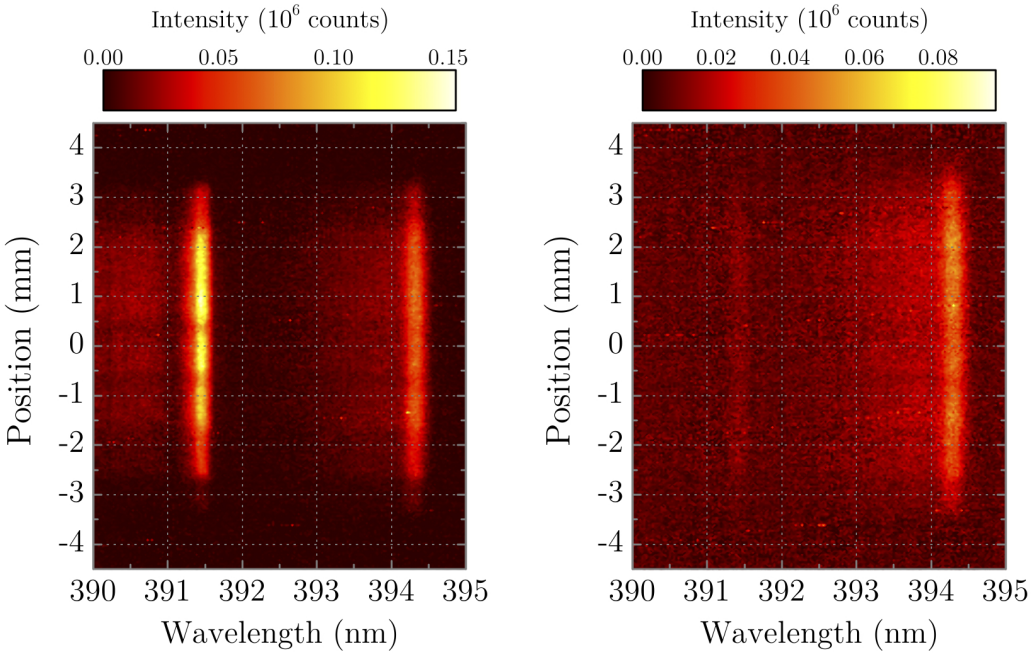

(a) Discharge on the rise of the pulse. **(b)** Discharge on the fall of the pulse.

Figure 8.1: Measured spectra for the **meshed plaster**. The position is relative to the centre of the secondary electrode.

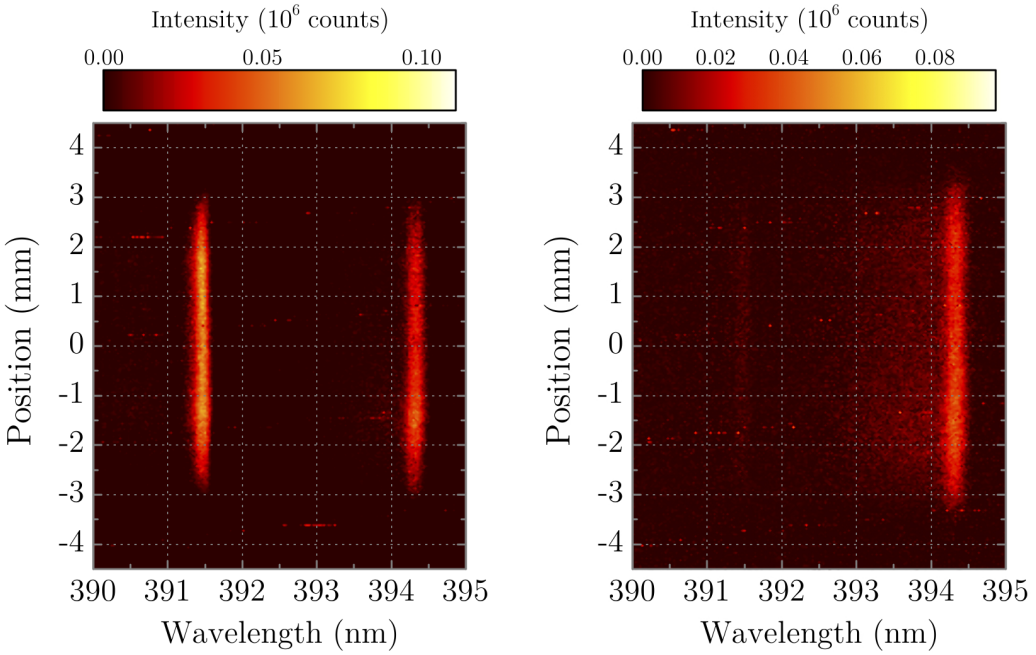

(a) discharge at the rise of the pulse. **(b)** discharge at the fall of the pulse.

Figure 8.2: Measured spectra for the **plane plaster**. The position is relative to the centre of the secondary electrode.

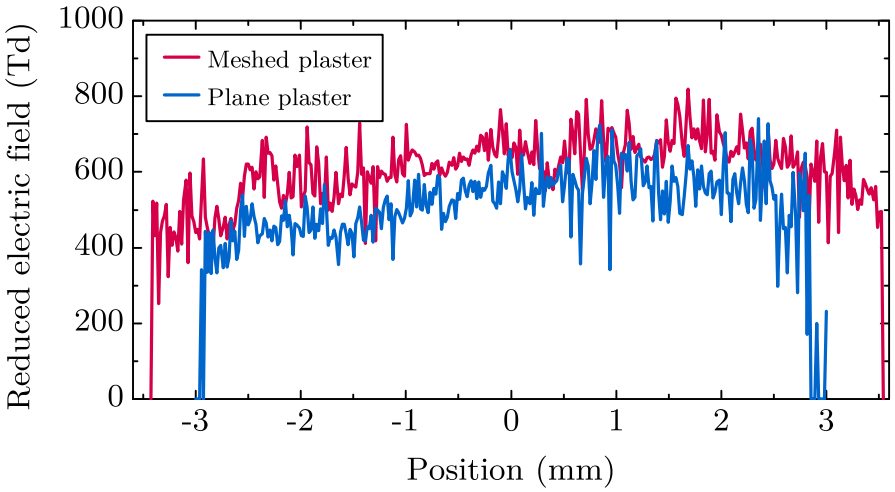

Figure 8.3: Reduced electric field profiles for the meshed plaster (red) and the plane plaster (blue) determined from the $R_{391/394}$ ratio using the empirical approach.

higher during the discharge on the rise of the pulse than during the discharge on the fall of the pulse. As was already mentioned in Chapter 5, the difference is that on the fall of the pulse the electrons are accelerated in the field setup by the deposited charges that still remain from the discharge on the rise of the pulse, rather than an externally applied field.

The field of the meshed plaster in figure 8.3 extends beyond the -3 mm and 3 mm positions. Since these measurements were performed at 6.5 kV these are likely the first signs of the outwards branching that was discussed in Chapter 5.

Chapter 9

Conclusions

Plasma medicine is a rapidly emerging field of research where non-thermal plasmas are applied in biomedical applications. One of the potential applications that is being investigated is the treatment of foot ulcers in diabetes by direct plasma treatment with a dielectric barrier discharge type source called plasma plaster. For an effective and safe treatment, the discharge properties must be predictable and controllable. As a contribution to the development process of a suitable source, the goal of the work presented is thesis was to determine the effects of a square mesh structured electrode on the discharge properties. It was hypothesised that using a structured electrode, instead of a more conventional solid plane electrode, is advantageous not only in terms of flexibility, but may also be used to tailor discharge properties through local electric field enhancement. To this end, a comparative study was performed between two plasma plasters, one with a square mesh structured electrode (the meshed plaster) and the other with a solid plane electrode (the plane plaster). A stainless steel secondary electrode was used. The main conclusions of this work are:

A structured electrode results in a structured discharge. Local electric field enhancement caused by the mesh structure forces the discharge to take the same structure as the mesh.

Both plasters operate in the diffuse DBD mode. Even though the discharge is structured in case of the meshed plaster, its characteristics are those of a diffuse discharge. Experimental evidence of a diffuse discharge for both plasters is found in the discharge current characteristics, ICCD images, gas temperature and reduced electric field values that are associated with the Townsend breakdown mechanism.

The meshed structure does not influence the gas temperature. The gas temperature during the discharge was investigated using optical emission spectroscopy on excited nitrogen molecules. Within the measurement error the same temperature was found for the two plasters.

The gas temperature is about 325 K for a pulse height of 6.5 kV. The temperature was measured at the relatively high pulse height of 6.5 kV to maximise the amount of emitted light. This value serves as an upper limit for the temperature at lower operation voltages, making the plaster safe to apply to a sensitive surface.

The reduced electric field measured with the meshed plaster is 20% higher than the field measured with the plane plaster
The results obtained by the empirical line intensity ratio method closely reflect the electric field enhancement predicted by the electrostatic model. Since the discharge is diffuse for both the plane and the meshed plaster, the 20% increase in the electric field is solely due to the structure of the mesh. This shows that the reduced electric field can indeed be controlled by the mesh pattern and that adapting the pattern may offer a way to tailor specific discharge properties.

For the development and design process of a suitable plasma source this means that mesh structured electrode can be successfully used without any undesired side effects such as discharge contraction or increased gas heating. Additionally, structured electrodes may offer the possibility to tailor specific discharge properties.

Appendices

Appendix A

Energy Dissipation in a Single Cycle and Error Analysis

In chapter 5 the following relation was used to calculate the amount of energy that is dissipated during one cycle of the periodically pulsed applied voltage:

$$E_{\text{cycle}} = \int_0^T V_{\text{gap}}(t) I_R(t)\,\mathrm{d}t = \int_0^T V(t) I(t)\,\mathrm{d}t. \qquad (\text{A.1})$$

A derivation of this equation is provided in section A.1. Then, in section A.2, an error analysis for the found energy values is given. The relevance and propagation of several potential sources of random and systematic errors are discussed.

A.1 Derivation

First, the product $V_{\text{gap}}(t)I_R(t)$ needs to be expressed in terms of $V(t)$ and $I(t)$, the voltage and current signals that are measured directly. This is done using the discharge cell part of equivalent circuit in figure 5.6, which is repeated in figure A.1. Additionally, the voltage across the barrier $V_{\text{barrier}}(t)$ and the voltage across the air gap $V_{\text{gap}}(t)$ are now explicitly indicated. Using the definition of capacitance and Kirchhoff's current and voltage laws, the following four coupled equations can be written:

$$V_{\text{barrier}}(t) = \frac{1}{C_{\text{barrier}}} \int I(\tau)\,\mathrm{d}\tau = \frac{Q(t)}{C_{\text{barrier}}}, \tag{A.2}$$

$$V_{\text{gap}}(t) = V(t) - V_{\text{barrier}}(t), \tag{A.3}$$

$$I_{\text{gap}}(t) = C_{\text{gap}} \frac{\mathrm{d}V_{\text{gap}}(t)}{\mathrm{d}t}, \tag{A.4}$$

$$I_R(t) = I(t) - I_{\text{gap}}(t), \tag{A.5}$$

where $Q(t)$ is the charge on capacitor C_{barrier}. Combining equations A.2 and A.3 gives an expression for the voltage across the air gap:

$$V_{\text{gap}}(t) = V(t) - \frac{Q(t)}{C_{\text{barrier}}}. \tag{A.6}$$

Assuming that C_{barrier} is constant, substitution of this relation into equation A.4 leads to

$$I_{\text{gap}}(t) = C_{\text{gap}} \frac{\mathrm{d}}{\mathrm{d}t}\left(V(t) - \frac{Q(t)}{C_{\text{barrier}}}\right) = C_{\text{gap}} \frac{\mathrm{d}V(t)}{\mathrm{d}t} - \frac{C_{\text{gap}}}{C_{\text{barrier}}} \frac{\mathrm{d}Q(t)}{\mathrm{d}t} \tag{A.7}$$

$$= C_{\text{gap}} \frac{\mathrm{d}V(t)}{\mathrm{d}t} - \frac{C_{\text{gap}}}{C_{\text{barrier}}} I(t). \tag{A.8}$$

Together with equation A.5, the following expression for the discharge current $I_R(t)$ is now obtained:

$$I_R(t) = I(t) - C_{\text{gap}} \frac{\mathrm{d}V(t)}{\mathrm{d}t} + \frac{C_{\text{gap}}}{C_{\text{barrier}}} I(t) \tag{A.9}$$

$$= \left[1 + \frac{C_{\text{gap}}}{C_{\text{barrier}}}\right] I(t) - C_{\text{gap}} \frac{\mathrm{d}V(t)}{\mathrm{d}t}. \tag{A.10}$$

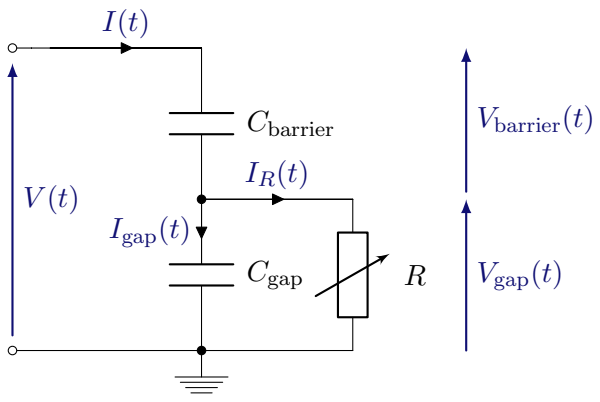

Figure A.1: Equivalent circuit of the discharge cell.

Multiplying equations A.6 and A.10, the product $V_{\text{gap}}(t)I_R(t)$ is now written as

$$\begin{aligned} V_{\text{gap}}(t)I_R(t) = &\left[1 + \frac{C_{\text{gap}}}{C_{\text{barrier}}}\right] V(t)I(t) \; - \; \frac{1}{C_{\text{barrier}}}\left[1 + \frac{C_{\text{gap}}}{C_{\text{barrier}}}\right] Q(t)I(t) \\ &- C_{\text{gap}}V(t)\frac{\mathrm{d}V(t)}{\mathrm{d}t} \; + \; \frac{C_{\text{gap}}}{C_{\text{barrier}}}Q(t)\frac{\mathrm{d}V(t)}{\mathrm{d}t}. \end{aligned} \tag{A.11}$$

Consequently, the integral of $V_{\text{gap}}(t)I_R(t)$ can be split into a sum of four integrals, which can then be evaluated separately. The second and third terms on the right hand side of equation A.11 are zero when integrated over a whole period, due to periodicity:

$$\int_0^T Q(t)I(t)\,\mathrm{d}t = \int_0^T Q(t)\frac{\mathrm{d}Q(t)}{\mathrm{d}t}\,\mathrm{d}t = \frac{1}{2}\left[Q^2(T) - Q^2(0)\right] = 0 \tag{A.12}$$

and

$$\int_0^T V(t)\frac{\mathrm{d}V(t)}{\mathrm{d}t}\,\mathrm{d}t = \frac{1}{2}\left[V^2(T) - V^2(0)\right] = 0. \tag{A.13}$$

Next, integrating the fourth term on the right hand side of equation A.11 by parts gives

$$\int_0^T Q(t)\frac{\mathrm{d}V(t)}{\mathrm{d}t}\,\mathrm{d}t = [Q(T)V(T) - Q(0)V(0)] - \int_0^T V(t)\frac{\mathrm{d}Q(t)}{\mathrm{d}t}\,\mathrm{d}t \tag{A.14}$$

$$= -\int_0^T V(t)I(t)\,\mathrm{d}t. \tag{A.15}$$

Finally, it follows that the integral of $V_{\text{gap}}(t)I_R(t)$ over a period is equal to

$$\int_0^T V_{\text{gap}}(t)I_R(t)\,\mathrm{d}t = \left[1 + \frac{C_{\text{gap}}}{C_{\text{barrier}}}\right]\int_0^T V(t)I(t)\,\mathrm{d}t - \frac{C_{\text{gap}}}{C_{\text{barrier}}}\int_0^T V(t)I(t)\,\mathrm{d}t \tag{A.16}$$

$$= \int_0^T V(t)I(t)\,\mathrm{d}t, \tag{A.17}$$

showing that the energy dissipated during one cycle can be obtained by measuring $V(t)$ and $I(t)$.

A.2 Error analysis

As mentioned in Chapter 5, the averaged energy dissipation per cycle, as shown in figure 5.9, is calculated using $N = 10$ single cycle measurement for each data point by:

$$\bar{E}_{\text{cycle}} = \frac{1}{N}\sum_{i=1}^{N} E_{\text{cycle}(i)}. \tag{A.18}$$

Several uncertainties can emerge in the calculation of averaged energy from voltage and current signals. To estimate the precision and the accuracy of the calculated averaged energy values, three potential sources of random and systematic errors, which together constitute the shown error bars, are now discussed.

A.2.1 Random errors and variations

When the energy is measured for different cycles at the same operation parameters, a certain distribution in the energy values is found. The main reason is the random variation in individual discharges: a discharge during one cycle is not exactly identical to a discharge during another cycle. This fact is immediately apparent from the jitter on the discharge current peaks, both in time and on peak height, as discussed in Chapter 5. Additionally, the electronics produce noise. However, since the calculation involves integration, which evens out random noise, electronic noise is unlikely to significantly influence the calculated energy value.

The distribution in measured energy values for a single cycle can be characterised by its standard deviation, which is given by [65]:

$$S_{E_{\text{cycle}}} = \sqrt{\frac{1}{N-1}\sum_{i=1}^{N}(E_{\text{cycle}(i)} - \bar{E}_{\text{cycle}})^2} \tag{A.19}$$

For example, the data point at 6 kV for the meshed plaster in figure 5.9 resulted in an averaged value of $\bar{E}_{\text{cycle}} = 142\,\mu\text{J}$ with a standard deviation of $S_{E_{\text{cycle}}} = 11\,\mu\text{J}$.

If now another $N = 10$ samples are taken, a slightly different average value may be found as a result of the limited amount of samples. The variation that is found in average values from different but equivalent sample sets is characterised by the standard deviation of the mean:

$$S_{\bar{E}_{\text{cycle}}} = \frac{S_{E_{\text{cycle}}}}{\sqrt{N}} = \sqrt{\frac{1}{N(N-1)}\sum_{i=1}^{N}(E_{\text{cycle}(i)} - \bar{E}_{\text{cycle}})^2} \tag{A.20}$$

So, in principle an arbitrarily *precise* averaged energy can be determined by increasing the number of samples used for averaging. Using equation B.20, the standard deviation in averages can be readily obtained from a single series of $N = 10$ measurements and results in $S_{\bar{E}_{\text{cycle}}} = 4\,\mu\text{J}$. To verify, repeating the calculation using 10 different cycles, resulted in an average value of $\bar{E}_{\text{cycle}} = 139\,\mu\text{J}$.

The standard deviation of the mean increases for larger pulse heights, but its value is found to be at most 5% of the average value. In the results presented in Chapter 5, the standard deviation of averages is calculated for each series of measurements by equation A.20 and is the first of three components that constitute the error bar.

A.2.2 Systematic errors

Besides random errors, systematic errors can also occur in a measurement. Contrary to random errors, systematic errors are not independent, and will therefore not even out when averaged. Two potential sources of systematic error are considered: the uncertainty in the probe conversion factors, and a mismatch in the temporal synchronisation of the signals.

Error in probe conversion factors

To analyse the propagation of an error introduced by the voltage and current probes, the numerical calculation of energy per cycle from the recorded signals is examined.

First, the actual voltage and current signals $V(t_i)$ and $I(t_i)$, sampled at times t_i, need to be recovered from the recorded probe data, $V_{\text{probe}}(t_i)$ and $I_{\text{probe}}(t_i)$. The actual voltage and current signals are scaled by the probes to make them suitable for measurement by

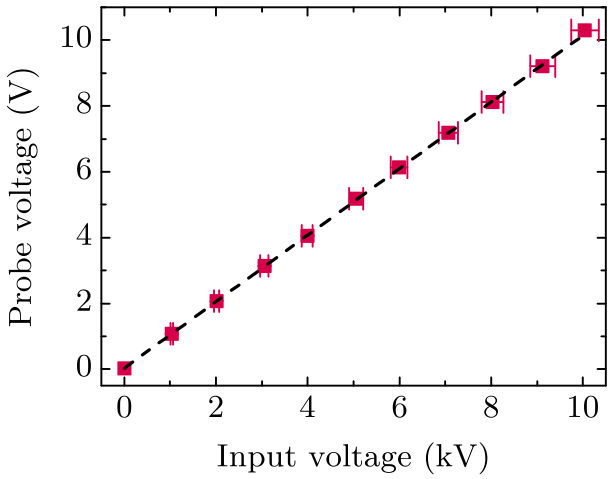

Figure A.2: Probe voltage measured by the high voltage probe against the input voltage according to the pulse generator (red squares), and a linear fit from which the probe factor is determined (black dashed line).

the oscilloscope. In addition to scaling the signal, the probes may also introduce a baseline offset, such that

$$V_{\text{probe}}(t_i) = a \cdot V(t_i) + b \tag{A.21}$$

and

$$I_{\text{probe}}(t_i) = c \cdot I(t_i) + d, \tag{A.22}$$

where a and c are the probe conversion factors and b and d represent a baseline offset. The high voltage probe is calibrated against the voltage monitor of the HV pulse generator, as shown in figure A.2. From a linear fit, the high voltage probe factor is determined to be $a = 1.02 \pm 0.02\text{V/kV}$ (relative error of approximately $\pm 2\%$). Both current probes have a conversion factor of $c = 1\,\text{V/A}$ with a relative error between 0% and +1%, according to the manufacturer [66]. Now the actual voltage and currents are obtained by

$$V(t_i) = a^{-1} \cdot (V_{\text{probe}}(t_i) - b) \tag{A.23}$$

and

$$I(t_i) = c^{-1} \cdot (I_{\text{probe}}(t_i) - d). \tag{A.24}$$

Assuming that the only systematic error originates from the probe conversion factors, the relative error in every voltage and current data point can be written as

$$\delta V(t_i) = \frac{\Delta V(t_i)}{V(t_i)} = \frac{\Delta(a^{-1})}{a^{-1}} = -\frac{\Delta a}{a} \in [-0.02, 0.02] \tag{A.25}$$

and

$$\delta I(t_i) = \frac{\Delta I(t_i)}{I(t_i)} = \delta(c^{-1}) = -\delta c \in [-0.01, 0], \tag{A.26}$$

where δ and Δ indicate the relative and absolute errors in their accompanying variables, respectively.

Next, the signals are multiplied

$$P(t_i) = V(t_i)I(t_i), \tag{A.27}$$

leading to a relative error in every multiplied value of

$$\delta P(t_i) = \delta V(t_i) + \delta I(t_i) \in [-0.03, 0.02] \tag{A.28}$$

The numerical quadrature $Q(P(t_i))$ that is used to numerically integrate $P(t_i)$ is the composite trapezoid rule [67]:

$$E_{\text{cycle}} = Q(P(t_i)) = \sum_{i=1}^{N} \frac{(t_i - t_{i-1})}{2}\Big[P(t_{i-1}) + P(t_i)\Big] \tag{A.29}$$

$$= \tau\left[\frac{1}{2}P(t_0) + P(t_1) + \cdots + P(t_{N-1}) + \frac{1}{2}P(t_N)\right], \tag{A.30}$$

where $\tau = t_i - t_{i-1}$ is the time interval between adjacent samples. From equation A.30 it follows that it is absolutely critical to apply baseline corrections in equations A.23 and A.24. The sum of a relatively small baseline offset can potentially become large and start to significantly contribute to the integral. Since both the energy per cycle and its average are (weighted) sums of $P(t_i)$, which all have the same relative error, it follows that

$$\delta\bar{E}_{\text{cycle}} = \delta E_{\text{cycle}} = \delta P(t_i) \in [-0.03, 0.02]. \tag{A.31}$$

So, the absolute systematic error in the averaged energy per cycle due to uncertainty in the probe conversion factors is

$$\Delta_{\text{probe}}\bar{E}_{\text{cycle}} = [-0.03, 0.02] \cdot \bar{E}_{\text{cycle}}. \tag{A.32}$$

Error in temporal synchronisation

So far, it has been assumed that $V(t_i)$ and $I(t_i)$ represent their corresponding continuous signal at the exact same time. Both the voltage and current probes have a response time and the coaxial cables that connect them to the oscilloscope cause an additional delay between an event and its recording. A mismatch in the synchronisation of the signals can result in an error in the found energy value.

As was briefly mentioned in Chapter 5, the voltage and current signals are synchronised using cross correlation between the current signals and the derivative of the voltage signal in the absence of a discharge. To synchronise the signals, 1024 repeated measurements are averaged on the oscilloscope to reduce noise. Additionally, to prevent biasing, the signals are first normalised, such that they have an average value of zero and unit variance, before their cross correlation is calculated. The actual calculation is done using MATLAB's `xcorr` function. The position of the maximum of the cross correlation indicates where the signals are best aligned and hence shows their relative delay. An example of a cross correlation plot is shown in figure A.3. The found delays are accounted for by setting an appropriate skew on the different oscilloscope channels.

Ultimately, the accuracy of the synchronisation is limited by the sampling frequency of the oscilloscope. In the present case the sample frequency is 2 GHz, which results in a time resolution of 0.5 ns. To estimate the error that a mismatch in synchronisation could induce, the voltage signal is shifted an additional amount of ± 0.5 ns and the energy is recalculated. In practice, this means that the recorded voltage data is shifted by one element to the left (+0.5 ns) or to the right (−0.5 ns). The recalculated energy values were always found within $\pm 2\%$ of the original value. Therefore, the absolute error due to uncertainty in synchronisation of the signals is estimated by

$$\Delta_{\text{sync}}\bar{E}_{\text{cycle}} = [-0.02, 0.02] \cdot \bar{E}_{\text{cycle}}. \tag{A.33}$$

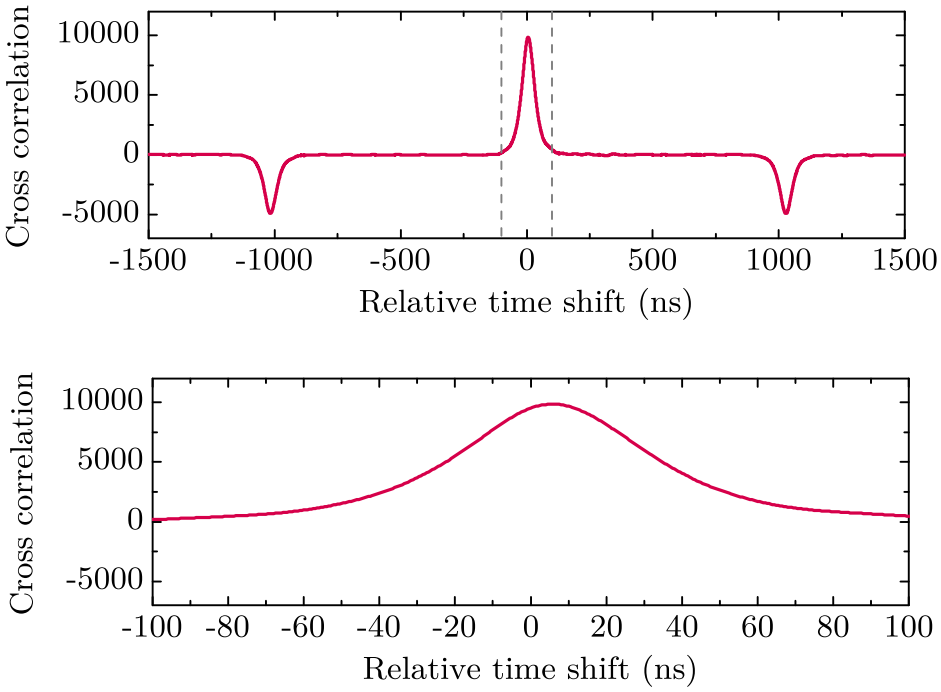

Figure A.3: Plot of the cross correlation between the HV side and GND side currents. The bottom graph is a zoomed view of the area enclosed by the two grey dashed lines in the top graph. A relative delay between the two signals of approximately 6 ns is found.

So, to conclude, the absolute errors $\Delta\bar{E}_{\text{cycle}}$ shown in figure 5.9 in Chapter 5 are the sum of the three discussed sources of error:

$$\Delta\bar{E}_{\text{cycle}} = S_{\bar{E}_{\text{cycle}}} + \Delta_{\text{probe}}\bar{E}_{\text{cycle}} + \Delta_{\text{sync}}\bar{E}_{\text{cycle}} \tag{A.34}$$

$$= S_{\bar{E}_{\text{cycle}}} + [-0.05, 0.04] \cdot \bar{E}_{\text{cycle}}, \tag{A.35}$$

where -0.05 corresponds to the minimum of the error bar, and 0.04 to the maximum of the error bar.

Appendix B

Spectroscopic Constants for Nitrogen

In this appendix the spectroscopic constants for the molecular states involved in the N_2 second positive system and the N_2^+ first negative system, which were used in the line-by-line radiation code presented in Chapters 7 and 8, are summarised.

Table B.1: Spectroscopic constants used in the line-by-line radiation code. Adapted from [68].

	Constants (cm^{-1})			
	N_2		N_2^+	
	$B\,^3\Pi_g$	$C\,^3\Pi_u$	$X\,^2\Sigma_g^+$	$B\,^2\Sigma_u^+$
T_e	59 619.35	89 136.88	0	25 461.11
Reference	[69]	[69]	[70]	[70]
$Y_{10} = \omega_e$	1734.025	2047.78	2207.22	2421.14
$Y_{20} = -\omega_e x_e$	−14.412	−28.9488	−16.226	−24.7
$Y_{30} = \omega_e y_e$	-3.3×10^{-3}	2.247 31	4.0×10^{-3}	−0.30
Y_{40}	-7.9×10^{-4}	−0.551 45	-6.1×10^{-3}	−0.0667
Y_{50}	4.2×10^{-5}		3.9×10^{-4}	
Y_{60}	-1.68×10^{-6}		-1.4×10^{-5}	
Y_{70}			2.0×10^{-7}	
Reference	[71]	[72]	[70]	[70]
$Y_{01} = B_e$	1.637 72	1.826 77	1.931 71	2.085 07
$Y_{11} = -\alpha_e$	−0.017 93	−0.024	−0.018 816	−0.0212
$Y_{21} = \gamma_e$	-1.04×10^{-4}	1.9×10^{-3}	-6.77×10^{-5}	-5×10^{-4}
Y_{31}	4.882×10^{-6}	-6×10^{-4}	-2.32×10^{-6}	-8.8×10^{-5}
Y_{41}	-2.12×10^{-7}			
Reference	[71]	[72]	[70]	[70]
$Y_{02} = -D_e$	-5.527×10^{-6}	-5.147×10^{-6}	-5.92×10^{-6}	
$Y_{12} = -\beta_e$	-9.584×10^{-9}	-2.137×10^{-6}	-3.9×10^{-8}	
$Y_{22} = -\epsilon_e$		1.2989×10^{-6}		
Y_{32}		-2.417×10^{-7}		
Reference	[71]	[72]	[70]	

References

[1] Lieberman M A and Lichtenberg A J 2005 *Principles of Plasma Discharges and Materials Processing* (Wiley)

[2] Fridman A 2008 *Plasma Chemistry* (Cambridge University Press)

[3] Graves D B 2014 *Phys. Plasmas* **21**, 080901

[4] Fridman A and Friedman G 2013 *Plasma Medicine* (Wiley)

[5] Fridman G, Friedman G, Gutsol A, Shekhter A B, Vasilets V N and Fridman A 2008 *Plasma Process. Polym.* **5**, 503–533

[6] Kong M G, Kroesen G, Morfill G, Nosenko T, Shimizu T, van Dijk J and Zimmermann J L 2009 *New J. Phys.* **11**, 115012

[7] Heinlin J, Morfill G, Landthaler M, Stolz W, Isbary G, Zimmermann J L, Shimizu T and Karrer S 2010 *J. Dtsch. Dermatol. Ges.* **8**, 968–76

[8] von Woedtke T, Reuter S, Masur K and Weltmann K D 2013 *Phys. Rep.* **530**, 291–320

[9] Laroussi M, Kong M G, Morfill G and Stolz W (eds) 2012 *Plasma Medicine: Applications of Low-Temperature Gas Plasmas in Medicine and Biology* (Cambridge University Press)

[10] Samukawa S, Hori M, Rauf S, Tachibana K, Bruggeman P, Kroesen G, Whitehead J C, Murphy A B, Gutsol A F, Starikovskaia S, Kortshagen U, Boeuf J P, Sommerer T J, Kushner M J, Czarnetzki U and Mason N 2012 *J. Phys. D. Appl. Phys.* **45**, 253001

[11] Shi Y and Hu F B 2014 *Lancet* **383**, 1947–8

[12] Singh N, Armstrong D and Lipsky B 2005 *JAMA* **293**, 217–228

[13] Wu S C, Driver V R, Wrobel J S and Armstrong D G 2007 *Vasc. Health Risk Manag.* **3**, 65–76

[14] Sibbald G R and Woo K Y 2008 *Diabetes. Metab. Res. Rev.* **24 Suppl 1**, S25–30

[15] Fridman G, Shereshevsky A, Jost M M, Brooks A D, Fridman A, Gutsol A, Vasilets V and Friedman G 2007 *Plasma Chem. Plasma Process.* **27**, 163–176

[16] Becker K H, Kogelschatz U, Schoenbach K H and Barker R J (eds) 2004 *Non-equilibrium Air Plasmas at Atmospheric Pressure* Series in Plasma Physics (CRC)

[17] Kogelschatz U 2003 *Plasma Chem. Plasma Process.* **23**, 1–46

[18] Townsend J 1947 *Electrons in Gases* (Hutchinson's)

[19] Raizer Y P 1991 *Gas Discharge Physics* (Springer)

[20] Parvulescu V I, Magureanu M and Lukes P (eds) 2012 *Plasma Chemistry and Catalysis in Gases and Liquids* (Wiley)

[21] Loeb L B and Meek J M 1940 *J. Appl. Phys.* **11**, 438

[22] Loeb L B and Meek J M 1940 *J. Appl. Phys.* **11**, 459

[23] Meek J and Craggs J 1953 *Electrical Breakdown of Gases* (Clarendon)

[24] Raether H 1964 *Electron Avalanches and Breakdown in gases* (Butterworths)

[25] Bruggeman P and Brandenburg R 2013 *J. Phys. D. Appl. Phys.* **46**, 464001

[26] Kogelschatz U 2002 *IEEE Trans. Plasma Sci.* **30**, 1400–1408

[27] Wagner H E, Brandenburg R, Kozlov K, Sonnenfeld A, Michel P and Behnke J 2003 *Vacuum* **71**, 417–436

[28] Chirokov A, Gutsol A and Fridman A 2005 *Pure Appl. Chem.* **77**, 487–495

[29] Massines F, Gherardi N, Naudé N and Ségur P 2009 *Eur. Phys. J. Appl. Phys.* **47**, 22805

[30] Garamoon A A and El-zeer D M 2009 *Plasma Sources Sci. Technol.* **18**, 045006

[31] Gherardi N and Massines F 2001 *IEEE Trans. Plasma Sci.* **29**, 536–544

[32] Gherardi N, Gouda G, Gat E, Ricard A and Massines F 2000 *Plasma Sources Sci. Technol.* **9**, 340–346

[33] Morshuis P H F and Kreuger F H 1990 *J. Phys. D. Appl. Phys.* **23**, 1562–1568

[34] Aldea E, Peeters P, De Vries H and Van De Sanden M 2005 *Surf. Coatings Technol.* **200**, 46–50

[35] Kanazawa S, Kogoma M, Moriwaki T and Okazaki S 1988 *J. Phys. D. Appl. Phys.* **21**, 838–840

[36] Roth J R, Rahel J, Dai X and Sherman D M 2005 *J. Phys. D. Appl. Phys.* **38**, 555–567

[37] Herzberg G 1950 *Molecular Spectra and Molecular Structure, Vol I. Spectra of Diatomic Molecules* (van Nostrand)

[38] Kovács I 1969 *Rotational Structure in the Spectra of Diatomic Molecules* (Hilger)

[39] Demtröder W 2006 *Atoms, Molecules and Photons: An Introduction to Atomic-, Molecular-, and Quantum-Physics* (Springer)

[40] Griffiths D J 2005 *Introduction to Quantum Mechanics* (Pearson)

[41] DuPont Kapton Polyimide Films - Summary of Properties URL `http://www.dupont.com/content/dam/assets/products-and-services/membranes-films/assets/DEC-Kapton-summary-of-properties.pdf`

[42] Rogowski W 1923 *Arch. für Elektrotechnik* **12**, 1–15

[43] Ernst G J 1984 *Opt. Commun.* **49**, 275–277

[44] Leyva I and Guerra J M 1999 *Meas. Sci. Technol.* **10**, N1–N2

[45] Liu S and Neiger M 2003 *J. Phys. D. Appl. Phys.* **36**, 3144–3150

[46] Pipa A V, Koskulics J, Brandenburg R and Hoder T 2012 *Rev. Sci. Instrum.* **83**, 115112

[47] Manley T C 1943 *Trans. Electrochem. Soc.* **84**, 83

[48] Pipa A V, Hoder T, Koskulics J, Schmidt M and Brandenburg R 2012 *Rev. Sci. Instrum.* **83**, 075111

[49] Seeböck R, Esrom H, Charbonnier M and Romand M 2000 *Plasmas Polym.* **5**, 103–118

[50] Kishi Y, Hashimoto T, Miyake H, Tanaka Y and Takada T 2009 *J. Phys. Conf. Ser.* **183**, 012005

[51] Kak A C and Slaney M 1988 *Principles of Computerized Tomographic Imaging* (IEEE Press)

[52] Pretzler G 1991 *Zeitschrift für Naturforsch. A* **46a**, 639–641

[53] Killer C Abel Inversion Algorithm URL http://www.mathworks.com/matlabcentral/fileexchange/43639-abel-inversion-algorithm

[54] Briels T M P, Kos J, Winands G J J, van Veldhuizen E M and Ebert U 2008 *J. Phys. D. Appl. Phys.* **41**, 234004

[55] Nijdam S, van de Wetering F M J H, Blanc R, van Veldhuizen E M and Ebert U 2010 *J. Phys. D. Appl. Phys.* **43**, 145204

[56] Dilecce G, Ambrico P F and Benedictis S D 2007 *Plasma Sources Sci. Technol.* **16**, 511–522

[57] Shengyi Polyimide SF302C URL http://www.entechelectronics.com.au/pdf/ShengyiPolyimideSF302C.pdf

[58] Specair URL http://www.specair-radiation.net/

[59] Dilecce G 2014 *Plasma Sources Sci. Technol.* **23**, 015011

[60] Kozlov K V, Wagner H E, Brandenburg R and Michel P 2001 *J. Phys. D. Appl. Phys.* **34**, 3164–3176

[61] Bruggeman P J, Sadeghi N, Schram D C and Linss V 2014 *Plasma Sources Sci. Technol.* **23**, 023001

[62] Phillips D M 1976 *J. Phys. D. Appl. Phys.* **9**, 507–521

[63] Jidenko N, Bourgeois E and Borra J P 2010 *J. Phys. D. Appl. Phys.* **43**, 295203

[64] Paris P, Aints M, Valk F, Plank T, Haljaste A, Kozlov K V and Wagner H E 2005 *J. Phys. D. Appl. Phys.* **38**, 3894–3899

[65] Taylor J R 1997 *An Introduction to Error Analysis* (University Science Books)

[66] Pearson Electronics inc Wide-band Current Monitors Technical support document URL http://www.pearsonelectronics.com/products/current-monitors

[67] Heath M T 2005 *Scientific Computing: An Introductory Survey* (McGraw-Hill)

[68] Laux C O 1993 *Optical Diagnostics and Radiative Emission of Air Plasmas* Ph.D. thesis Stanford University

[69] Huber K and Herzberg G 1979 *Molecular Spectra and Molecular Structure, Vol IV. Constants of Diatomic Molecules* (van Nostrand)

[70] Klynning L and Pagès P 1982 *Phys. Scr.* **25**, 543–560

[71] Roux F and Michaud F 1990 *Can. J. Phys.* **68**, 1257–1261

[72] Roux F, Michaud F and Vervloet M 1993 *J. Mol. Spectrosc.* **158**, 270–277